UNDERSTANDING SPACE PLASMA THROUGH DIAGNOSTICS AND MODELLING

M.Tech. Thesis

By

HARSH KARARWAL

DEPARTMENT OF ASTRONOMY, ASTROPHYSICS AND SPACE ENGINEERING

INDIAN INSTITUTE OF TECHNOLOGY INDORE

May 2025

UNDERSTANDING SPACE PLASMA THROUGH DIAGNOSTICS AND MODELLING

A THESIS

Submitted in partial fulfillment of the
requirements for the award of the degree
of
Master of Technology

by

HARSH KARARWAL

DEPARTMENT OF ASTRONOMY, ASTROPHYSICS AND SPACE ENGINEERING

INDIAN INSTITUTE OF TECHNOLOGY INDORE

May 2025

INDIAN INSTITUTE OF TECHNOLOGY INDORE

CANDIDATE'S DECLARATION

I hereby certify that the work which is being presented in the thesis entitled **UNDERSTANDING SPACE PLASMA THROUGH DIAGNOSTICS AND MODELLING** in the partial fulfillment of the requirements for the award of the degree of **MASTER OF TECHNOLOGY** and submitted in the **DEPARTMENT OF ASTRONOMY, ASTROPHYSICS AND SPACE ENGINEERING, Indian Institute of Technology Indore**, is an authentic record of my own work carried out during the time period from July 2023 to May 2025 under the supervision of Dr. Bhargav Vaidya, Associate Professor, Department of Astronomy, Astrophysics and Space Engineering, IIT Indore.

The matter presented in this thesis has not been submitted by me for the award of any other degree of this or any other institute.

16/05/2025

Signature of the student with date

(HARSH KARARWAL)

This is to certify that the above statement made by the candidate is correct to the best of my/our knowledge.

16/5/2025

Signature of the Supervisor with date

(Dr. BHARGAV VAIDYA, ASSOCIATE PROFESSOR)

HARSH KARARWAL has successfully given his/her M.Tech. Oral Examination held on **5th May, 2025.**

Signature(s) of Supervisor(s)

Date: 16/5/2025

Programme Coordinator, M.Tech.

Date: 16-05-2025

Manoneeta Chakraborty

Convenor, DPGC

Date: 16/05/2025

HoD, DAASE

Date:

ACKNOWLEDGEMENTS

I would like to express my sincere gratitude to my thesis supervisor, **Dr. Bhargav Vaidya**, for his invaluable support and guidance throughout the course of this research work. I am also thankful to the faculty and staff of the **Department of Astronomy, Astrophysics and Space Engineering**, IIT Indore, for their support and for providing the infrastructure and facilities essential for carrying out this research work.

I sincerely acknowledge the contributions of **Dr. Nishant Sirse**, Associate Professor and Director R&D at IPS Academy, Indore, and his Ph.D. student **Mr. Akanshu Khandelwal**, for their generous assistance in the fabrication of the Langmuir probe and the custom design of the plasma chamber, both of which were vital to this experimental study.

I am profoundly grateful to my parents for their unconditional love, patience, and understanding, especially during the times I could not be in touch as often as I should have been. Their enduring support has been the foundation of all my efforts. I also thank my brother and sister for their constant motivation and belief in me throughout this journey.

Lastly, I extend heartfelt thanks to my dear friend, whose thoughtful encouragement, insightful conversations, and emotional support were a steady source of strength during the most challenging moments of this work.

— Harsh Kararwal

ABSTRACT

The fourth fundamental state of matter, plasma, is a highly ionized gas composed of neutral atoms, free electrons, and ions. A comprehensive understanding of plasma behavior necessitates accurate measurement of key plasma parameters such as plasma potential, electron and ion densities, and electron temperature.

This thesis presents the development of a plasma diagnostics toolkit combining Optical Emission Spectroscopy, often abbreviated as OES, and the Langmuir probe, designed to operate within a custom-fabricated plasma chamber. Air and argon plasmas were generated at varying discharge conditions and characterized using an OES spectrometer. Spectral data were acquired via the software interface integrated with the spectrometer, followed by baseline correction and smoothing to identify peak wavelengths and intensities. These refined spectra enabled the construction of Boltzmann plots, from which the electron temperature (T_e) was derived. Electron density (n_e) was subsequently calculated using the FWHM and the Stark broadening parameter (ω) of selected emission lines. Furthermore, additional key plasma parameters were computed for a range of pressures and applied voltages. Trends and correlations between these parameters and discharge conditions were analyzed and presented graphically, offering deeper insight into the influence of pressure and voltage on plasma behavior.

The thesis also focuses on the design and fabrication of a Langmuir probe. An equivalent circuit model of the Langmuir probe was developed and simulated using LTspice to analyze the expected current–voltage (I–V) characteristics curve. A Langmuir probe was initially manufactured using a tungsten tip; however, due to dimensional constraints and incompatibility with the plasma chamber setup, a new probe was designed and fabricated. The redesigned probe, featuring a tungsten tip with an exposed length of $8mm$ and a diameter of $0.1mm$, along with a custom electronic circuit box, was successfully integrated into the plasma chamber. It passed vacuum integrity tests and demonstrated robust mechanical stability during vertical placement between electrodes. The use of both OES and Langmuir probe techniques enables complementary diagnostics, allowing for

cross-validation of plasma parameters and improved measurement accuracy.

This work contributes to the establishment of a versatile and modular plasma diagnostic platform, suitable for both research and teaching purposes. The experimental setup and diagnostic methodology developed in this thesis will be integrated into the M.Sc. Astronomy Laboratory curriculum to enrich practical training in plasma physics.

Contents

List of Figures

List of Tables

Nomenclature

n	Particle density
n_e	Electron Density
n_i	Ion density
T	Temperature in Kelvin
λ_D	Debye Length
ω	Plasma Oscillation Frequency
ω_{pe}	Electron Plasma Frequency
τ	Mean time between particle collisions
N_D	Number of particles in Debye sphere
T_e	Electron Temperature
T_i	Ion Temperature
T_n	Neutral Temperature

Acronyms

D Deuterium (^{2}H). 7

ITER the International Thermonuclear Experimental Reactor. 7

LTE Local Thermodynamic Equilibirium. 9

MHD Magnetohydrodynamics. xiii, 7, 8

OD Outer Diameter. 67

PECVD Plasma-Enhanced Chemical Vapor Deposition. 6

T Tritium (^{3}H). 7

Chapter 1

Introduction

1.1 Fundamentals of Plasma

Plasma is a quasineutral gas composed of charged particles such as electrons, ions and the neutral particles that display unique collective behavior. **Quasineutrality** implies that the plasma is neutral enough, hence one can take $n_i \sim n_e \sim n$, but not so neutral that all the intriguing electromagnetic forces dissipate. **Collective Behavior** describes how long-range electromagnetic forces on the motion of particles within the plasma. Due to Coulomb forces from moving charges, plasma particles interact across long-range distances, unlike neutral gas particles. For example, two weakly charged regions of plasma which are separated by a distance r exert forces on each other even at large separations because the volume of plasma contributing to these forces increases with r^3, counteracting the Coulomb force reduction by $1/r^2$. This interaction gives rise to complex and diverse plasma motions, enriching the study of plasma physics[1]. For an ionized gas to be classified as a plasma, it must satisfy the following 3 critical conditions:

i. **Debye Length Condition** ($\lambda_D \ll L$): The Debye length (λ_D), represents the scale over which electric fields are shielded in a plasma. It must be much smaller than the overall size of the plasma, ensuring effective shielding.

ii. **Sufficient Particle Density** ($N_D \gg 1$): The number of particles in a Debye sphere, N_D, must be significantly greater than one for Debye shielding to be statistically valid. The number is calculated using:

$$N_D = n \cdot \frac{4}{3}\pi\lambda_D^3 = 1.38 \times 10^6 \frac{T^{3/2}}{n^{1/2}}$$

where T represents temperature in Kelvin, and n represents particle density.

iii. **Dominance of Electromagnetic Forces** ($\omega\tau > 1$): The product of the plasma oscillation frequency (ω) & the mean time between particle collisions (τ) must be greater than one. This make sure that long-range electromagnetic forces dominate over local collisional forces, allowing the plasma to exhibit its characteristic behaviors [2].

A medium is classified as a plasma if it meets the aforementioned conditions, distinguishing it from conventional ionized or neutral gases. This framework is fundamental to understanding and analyzing the complex properties of plasma.

Figure 1.1: Benjamin Franklin's initial experiments with the atmospheric plasma phenomenon of lightning [5].

1.2 Occurrence of Plasma in Nature and in the Laboratory

Plasmas are found in a wide range of natural and artificial environments, ranging from interstellar space to highly controlled laboratory settings on Earth. Despite the wide variation in their physical properties such as temperature, density, and scale they exhibit fundamental behaviors that can be described by a unified framework of classical physics [1].

One of the earliest experimental interactions with plasma-like phenomena can be traced back to Benjamin Franklin's famous experiments with lightning (Figure 1.1), which may explain the historical fame of plasma research in Philadelphia [4, 5].

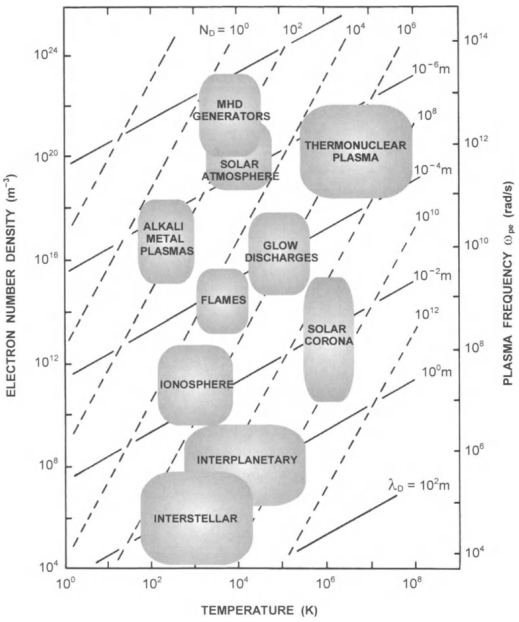

(a) Typical ranges of temperature and electron density for various laboratory and cosmic plasmas, along with their characteristic physical parameters:λ_D, ω_{pe}, & (N_D) contained within a Debye sphere [2].

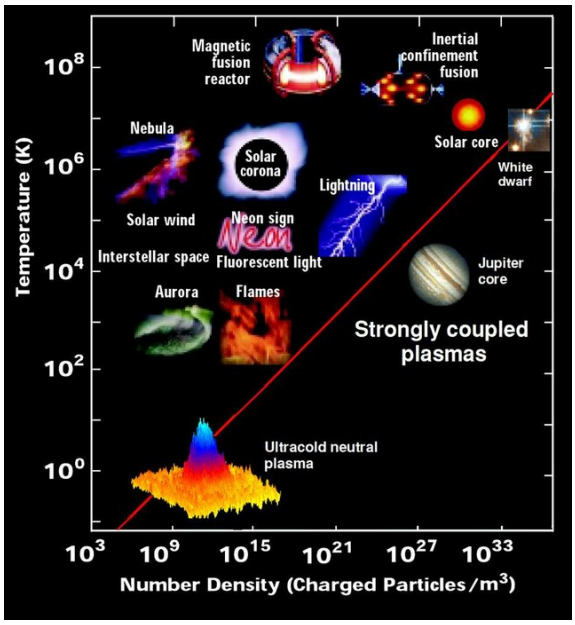

(b) Different types of plasmas and their position in temperature-density phase space. [6]

Figure 1.2: Plasma Temperatures And Densities.

Figure 1.2a presents the basic characteristics of different laboratory and cosmic plasmas, plotted as a function of their temperature (T) and electron number density (n_e). It also includes derived physical parameters such as the Debye length (λ_D), electron plasma frequency (ω_{pe}), and the number of electrons (N_D) within a Debye sphere [2].

1.2.1 Occurence Of Plasma in Nature

The Solar Plasma and Its Atmospheric Layers

The Sun, our nearest star, is a self-sustained thermonuclear plasma reactor. At its core, where temperatures exceed 1.2×10^7 K, hydrogen nuclei undergo fusion to form helium, releasing immense energy in the process [2]. Due to its massive size (2×10^{30} kg), gravitational pressure maintains the Sun in a fully ionized, gaseous plasma state.

The Sun has no sharp boundary, its visible disk i.e., the photosphere, is approximately 6000 K and several hundred kilometers thick. Above it lies the chromosphere, a reddish ring about 10,000 km thick, featuring prominences with temperatures around 100,000 K. Surrounding all of this is the solar corona which is a hot, tenuous plasma extending millions of kilometers into space, reaching temperatures above 10^6 K. The solar magnetic field, typically 10^{-4} T, intensifies up to 0.1 T in sunspot regions [2].

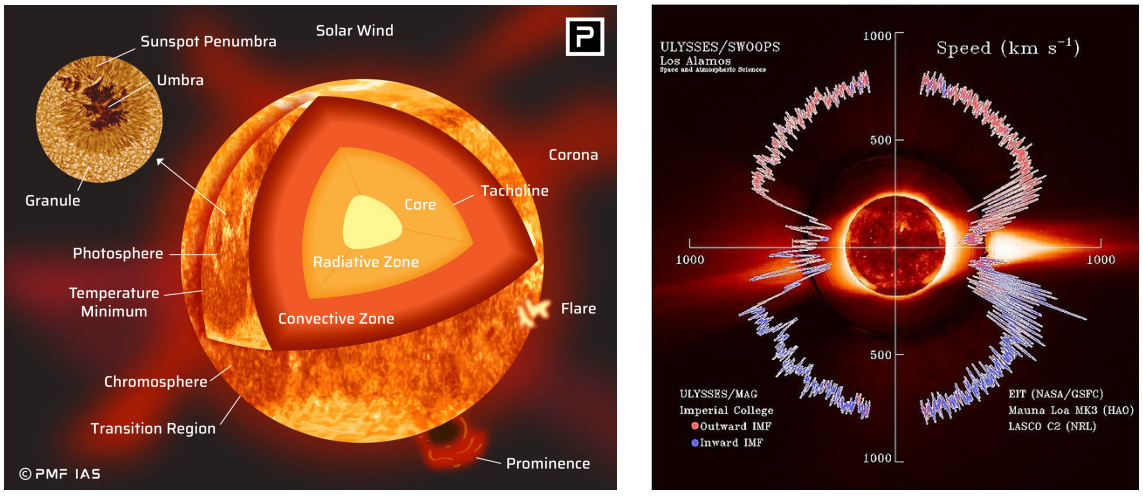

(a) **(b)**

Figure 1.3: (a.) The Sun's Internal Structure and Atmosphere [7] (b.) Ulysses's observations of solar wind speed as a function of helio latitude during solar minimum. [8]

Solar Wind

The solar corona emits a highly conductive plasma known as the solar wind. This outflow of electrons and protons expands supersonically into space, dragging the solar magnetic field into spiral shapes due to solar rotation. Typical solar wind parameters include $n_e \sim 5 \times 10^6$ m^{-3}, $T_e \sim 5 \times 10^4$ K, $T_i \sim 10^4$ K, and $B \sim 5 \times 10^{-9}$ T, with drift velocities around 300–500 km/s [2].

Figure 1.3a illustrates the structure of the Sun and its distinct atmospheric layers, while Figure 1.3b depicts the variation of solar wind speed with helio latitude during solar minimum [7, 8].

Earth's Magnetosphere and the Van Allen Radiation Belts

As the solar wind encounters Earth's magnetic field, it compresses the field on the sunward side and stretches it into a magnetotail on the night side. This interaction forms the magnetosphere, bounded by the magnetopause (Figure 1.4). Within this structure lie the Van Allen radiation belts, where energetic electrons and protons spiral along geomagnetic field lines. These belts arise from trapped cosmic ray interactions and periodic solar eruptions [2].

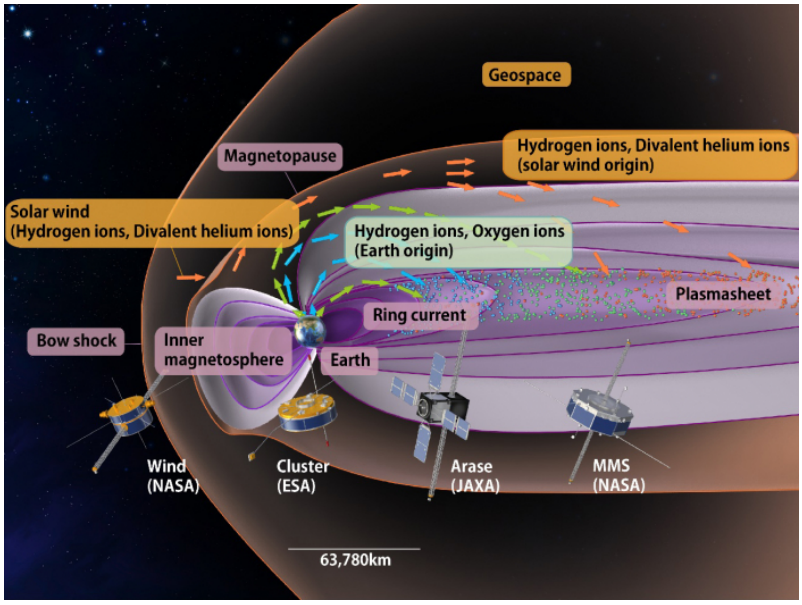

Figure 1.4: Solar wind and geospace observations show that during space storms, plasma in the inner magnetosphere primarily originates from Earth rather than the solar wind. [9].

The Ionosphere and Auroras

The ionosphere, ranging from 60 km to over 1000 km altitude, is a dense plasma layer created by solar UV and X-ray ionization of atmospheric gases. It plays a critical role in long-range radio communication and is influenced strongly by geomagnetic activity.

Auroras occur when energetic solar particles follow Earth's magnetic field lines and collide with particles in the ionosphere, resulting in the emission of visible light . These trapped particles are most concentrated near the magnetic poles and are responsible for phenomena such as the aurora borealis (Figure 1.5). Along with lightning, auroras represent the most commonly observed natural

plasma phenomena on Earth [2, 4].

Figure 1.5: Northern lights (aurora borealis). [10].

Astrophysical and Extragalactic Plasmas

In the broader cosmos, plasmas are present in nearly all astrophysical settings. Interstellar plasmas have densities around 1 particle/cm^3 and magnetic fields near 10^{-9} T. Phenomena include supernova shock waves, neutron star emissions, and synchrotron radiation from pulsars. The Crab Nebula is a prototypical plasma system with strong magnetic fields. Black holes and active galactic nuclei also host relativistic plasmas that emit high-energy radiation (Figure 1.2) [2].

1.2.2 Occurence Of Plasma in the Laboratory

Historical Background and Gas Discharges

Plasma physics began with the studies of glow discharges in vacuum tubes by Langmuir, Tonks and their collaborators in the 1920s. These weakly ionized systems (typically $T_e \sim 2$ eV, $n \sim 10^{14}$–10^{18} m^{-3}) revealed critical phenomena such as Debye shielding and plasma sheaths [1]. Early uses included neon lights, mercury rectifiers, and spark gaps (Figure 1.6a).

Semiconductor and Industrial Plasmas

The growth of the semiconductor industry brought gas discharges into high-tech applications. Low-temperature RF-driven plasmas are now essential for etching, thin-film deposition, and microfabrication. Magnetron sputtering, Plasma-Enhanced Chemical Vapor Deposition (PECVD) (Figure 1.6b), and ion beam tools rely heavily on partially ionized plasma sources [4].

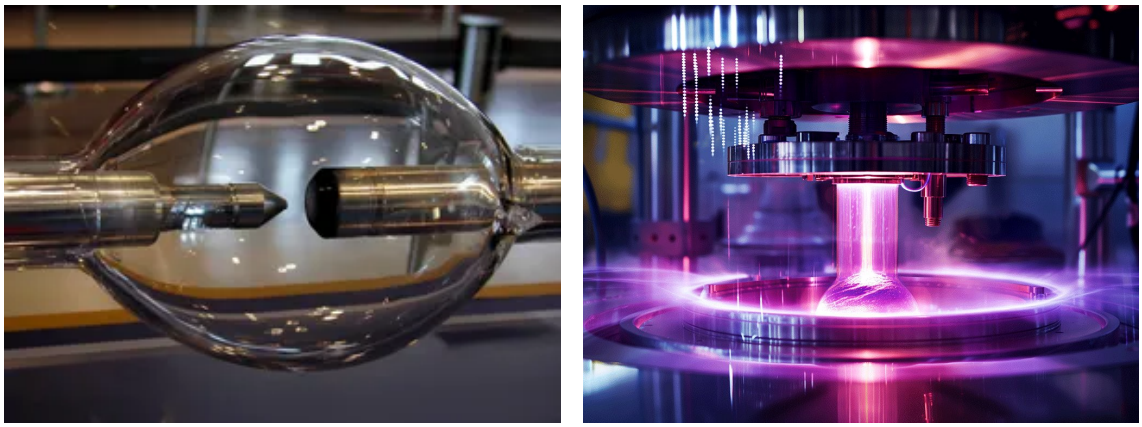

(a) **(b)**

Figure 1.6: (a.) Electric discharge lamp: Xenon short-arc discharge lamp with tungsten electrodes, used for producing bright white light in motion-picture projectors [11] (b.) Plasma-enhanced chemical vapor deposition (PECVD). [12]

Controlled Thermonuclear Fusion

Fusion research began in the 1950s to mimic solar energy production on Earth. Achieving Deuterium (^{2}H) (D)–Tritium (^{3}H) (T) fusion requires ion temperatures exceeding 10 keV. The principal reactions involved are:

$$\mathrm{D} + \mathrm{D} \rightarrow {}^3\mathrm{He} + n + 3.27\ \mathrm{MeV}$$

$$\mathrm{D} + \mathrm{D} \rightarrow {}^3\mathrm{H} + p + 4.03\ \mathrm{MeV}$$

$$\mathrm{D} + \mathrm{T} \rightarrow {}^4\mathrm{He} + n + 17.58\ \mathrm{MeV}$$

Devices such as tokamaks (e.g., the International Thermonuclear Experimental Reactor (ITER)) (Figure 1.7) confine the plasma magnetically using a combination of toroidal and poloidal magnetic fields. Other confinement schemes include stellarators, magnetic mirror machines, and theta-pinch devices. Inertial confinement fusion, on the other hand, uses high-energy laser beams to implode a small D-T pellet. The Lawson criterion ($n\tau$ product) determines the minimum conditions for achieving a net energy gain from fusion reactions [2].

MHD Generators and Plasma Propulsion

In an MHD generator, a conductive plasma stream moves through a magnetic field, inducing a transverse current via the Lorentz force. The extracted electrical energy avoids thermal-cycle inefficiencies.

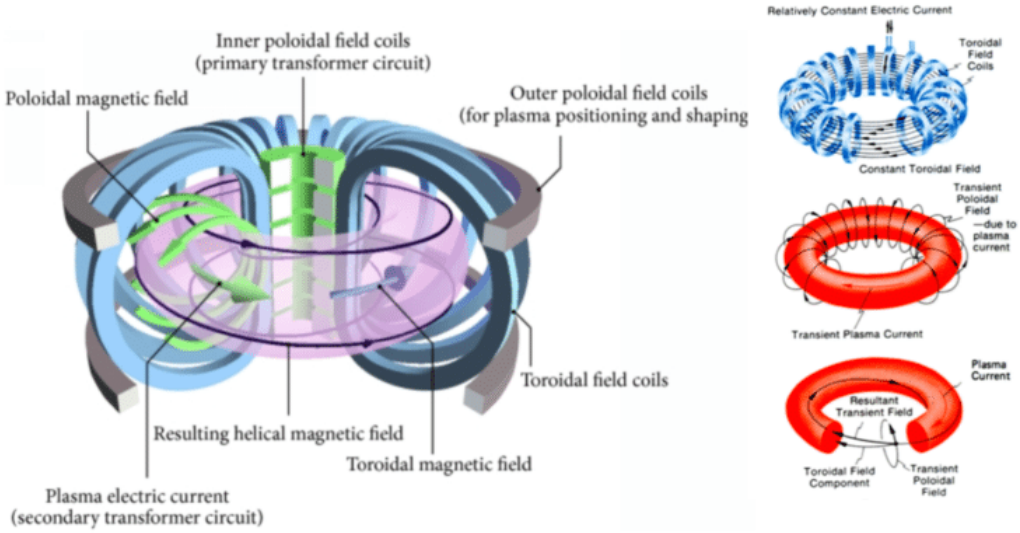

Figure 1.7: Schematic of a tokamak illustrating the toroidal and poloidal magnetic coils, along with the resulting toroidal and poloidal magnetic field lines (in black) used for plasma confinement in fusion devices. [13].

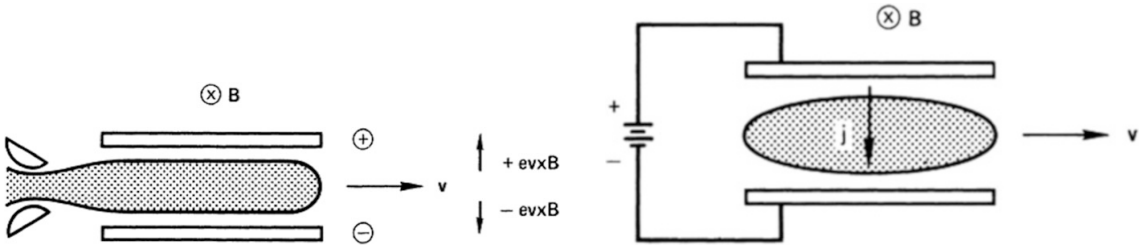

Figure 1.8: (a.) Principle Of the MHD generator (b.) Principle of plasma-jet engine utilized for spacecraft propulsion. [1]

Reversing this principle, plasma propulsion systems (e.g., Hall thrusters) accelerate ions via $\vec{J} \times \vec{B}$ forces, providing efficient, long-duration spacecraft propulsion [2].

Atmospheric and Biomedical Plasmas

Atmospheric-pressure plasma jets can be produced using RF or microwave power in noble gases. These compact plasmas are used in sterilization, tissue cauterization, and surface processing. Roll-to-roll manufacturing systems also employ atmospheric plasmas for large-scale substrate treatment [4].

In conclusion, plasmas are omnipresent in both cosmic and terrestrial systems. From the Sun's core to microchips, their behavior underpins natural phenomena and advanced technologies alike.

1.3 Plasma Classifications Across Physical and Operational Regimes

Plasmas exist across an enormous range of conditions and exhibit various degrees of ionization, temperature, and confinement. These characteristics lead to multiple classification schemes, each emphasizing specific physical behaviors or applications [1, 2].

1.3.1 Based on Temperature

In this classification, plasma is divided into two broad categories based on energy distribution among particles.

Thermal Plasma: A plasma in Local Thermodynamic Equilibirium (LTE), where $T_e \approx T_i \approx T_n$. Common in fusion, welding arcs, and atmospheric plasma torches. These plasmas are dense, radiative, and often modeled using fluid theory [2].

Non-Thermal Plasma: Characterized by $T_e \gg T_i \approx T_n$, which implies electrons have much higher average kinetic energy than ions and neutrals. This allows efficient ionization at low gas temperatures, enabling applications like plasma medicine and thin-film etching [1, 4].

The engineering aspects and application areas differ for thermal and non-thermal plasmas. Thermal plasmas are usually more powerful, whereas non-thermal plasmas are more selective.

1.3.2 Based on Degree of Ionization

A distinction between **weakly ionized and strongly ionized plasmas** can be drawn based on the dominant type of particle interaction. In **weakly ionized plasmas**, interactions between charged and neutral particles are predominant, while long-range Coulomb forces play a relatively minor role.

However, as the degree of ionization increases, Coulomb interactions between charged species become more significant. In **strongly ionized plasmas**, particularly those which are **fully ionized**, these long-range electromagnetic interactions dominate the plasma behavior, influencing both dynamics and transport properties. [2].

1.3.3 Based on Pressure and Density

Low-Pressure Plasma: Typically found in labs and space, where ions and electrons are less collisional. Debye lengths and mean free paths are relatively large [2].

High-Pressure Plasma: Found in arcs and flames. Highly collisional and well-described by fluid equations. Used in industrial cutting and sterilization [3].

1.3.4 Based on Source and Application

Natural Plasmas: Naturally occurring plasmas like the ionosphere, auroras, and interplanetary medium. Their study helps us understand space weather and solar-terrestrial interactions [2].

Artificial Plasmas: Created in labs and industries for purposes like micro-fabrication, propulsion, and sterilization. Common sources include RF and microwave discharges [3, 4].

1.4 Overview of Plasma Generation in the Laboratory

Plasma generation in laboratory environments is achieved by introducing energy into a neutral gas to ionize it, thereby producing a mixture of charged and neutral species. This process is typically carried out under low-pressure conditions to allow the free path of electrons and ions to be long enough for effective energy transfer. The energy is supplied via electric or electromagnetic fields, initiating what is known as a **gas discharge** [1, 4, 3].

Several plasma generation techniques are widely used in laboratory and industrial applications, each suited to different regimes of pressure, power, and plasma density:

1.4.1 DC Glow Discharge

A DC glow discharge is one of the most fundamental plasma sources and is widely studied due to its simplicity and rich structure. It is established by applying a direct current voltage across two electrodes placed inside a vacuum chamber filled with a low-pressure inert gas, typically argon or helium. The operating pressure usually lies between 0.1 to 1 mbar.

When the applied voltage exceeds the breakdown voltage, gas ionization occurs via electron-neutral collisions, leading to the formation of a self-sustained discharge. The structure of a DC glow discharge includes several distinct regions along the axis between the cathode and anode (Figure 1.9) [3, 14]:

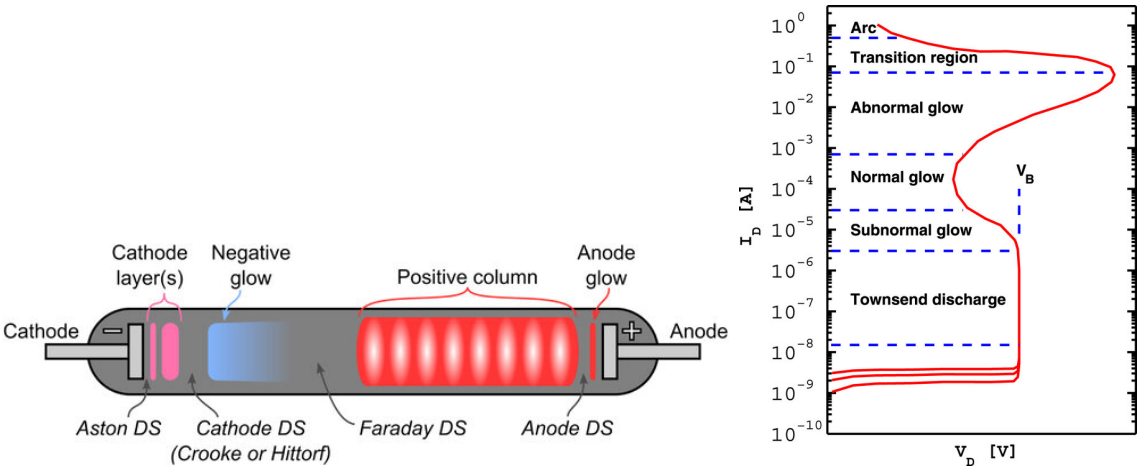

Figure 1.9: (a.) A schematic representation of the direct current glow discharge illustrating the several distinct regions that emerge between the cathode and the anode (b.) The current versus applied voltage plot for DC discharge [14]

- **Crookes Dark Space:** Located adjacent to the cathode, this region is dark due to high-energy electrons that have yet to excite gas atoms via inelastic collisions. It is characterized by a strong electric field and low light emission.

- **Negative glow:** A bright region following the cathode fall where most of the ionization occurs. Electrons here gain enough energy to excite and ionize neutral atoms, causing visible light emission.

- **Faraday dark space:** Situated between the negative glow and the positive column, the Faraday dark space is another region of reduced luminosity. Here, the electron energy has decreased due to prior collisions, leading to a lower probability of further excitation of gas atoms. Consequently, light emission diminishes. This region is named after Michael Faraday, who first observed it during his experiments with electric discharges in gases.

- **Positive column:** A quasi-neutral, uniformly glowing region that occupies the main body of the discharge. It sustains the current over the gap length and shows minimal electric field.

- **Anode glow and anode fall:** Close to the anode, weak light emission and a small potential drop are observed.

DC glow discharges are widely used in material processing, plasma cleaning, and diagnostics due to their reproducibility and low-temperature operation.

Breakdown Voltage and Paschen's Law in DC Glow Discharges

In order to initiate a DC glow discharge, the applied voltage must be high enough to ionize the neutral gas and causes a breakdown. This process is primarily driven by electron-impact ionization and secondary electron emission occurring near the cathode.

When an electric field is applied across a gas-filled chamber, free electrons accelerate and collide with neutral atoms, ionizing them and creating electron-ion pairs. This avalanche process is quantified by the first Townsend coefficient α, which represents the number of ionizing collisions per unit length. As electrons multiply through collisions, positive ions drift toward the cathode, where they release additional electrons upon impact, sustaining the discharge through secondary emission [3].

The condition for a self-sustained discharge, assuming negligible ion current at the sheath edge, leads to the classic expression for the breakdown in terms of the Townsend coefficient and secondary emission coefficient γ_{se}:

$$\exp(\alpha d) = 1 + \frac{1}{\gamma_{se}} \tag{1.1}$$

where d is the electrode separation.

The Townsend coefficient α is an exponential function of the reduced electric field E/p, and is empirically approximated as:

$$\frac{\alpha}{p} = A \exp\left(-\frac{Bp}{E}\right) \tag{1.2}$$

where A and B are gas-dependent constants determined experimentally.

Combining this with $V_b = Ed$, the expression for the breakdown voltage becomes:

$$V_b = \frac{Bpd}{\ln(Apd) - \ln\left[\ln\left(1 + \frac{1}{\gamma_{se}}\right)\right]} \tag{1.3}$$

The above Equation (1.3) is known as the **Paschen's Law**, and it shows that the **breakdown voltage V_b is a function of the product pd.**

At small pd values, electrons cannot gain sufficient energy between collisions, while at large pd, frequent collisions prevent them from reaching ionization energy. Therefore, V_b has a minimum at a characteristic pd, making the Paschen curve an essential tool in discharge design [3, 14].

The more detailed derivation and analysis, including the vacuum breakdown formulae and

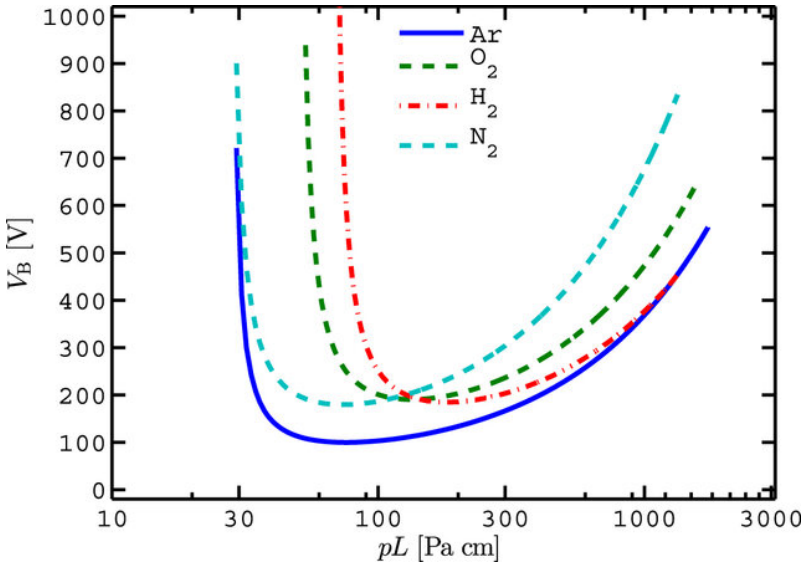

Figure 1.10: Paschen curve showing breakdown voltage as a function of pressure–distance product (pd) for various gases. The minimum point corresponds to the optimal condition for breakdown.[14]

secondary electron effects, are included in the appendix for detailed reference.

1.4.2 Capacitively Coupled Plasma (CCP)

Capacitively coupled plasmas (CCPs) are among the most commonly used low-temperature plasma sources, particularly in microfabrication and surface processing applications. A CCP is generated by applying a radio-frequency (RF) voltage—typically 13.56 MHz—between two electrodes enclosed in a low-pressure gas-filled chamber (e.g., argon, oxygen, or nitrogen). The RF electric field oscillates rapidly, imparting energy to free electrons in the plasma through both bulk ohmic heating and sheath interactions [3].

Electrons gain sufficient energy to ionize the background gas via inelastic collisions, creating additional electron-ion pairs and sustaining the discharge. The main power absorption mechanisms include:

- **Stochastic (collisionless) heating:** Occurs due to electron interaction with the moving sheath edge near electrodes, prominent at low pressures.
- **Ohmic heating:** Occurs through electron-neutral collisions in the plasma bulk, more effective at higher pressures.

The plasma is bounded by sheaths on both electrodes. Due to the higher mobility of electrons compared to ions, a time-averaged negative DC self-bias forms on the smaller (or powered) electrode. The resulting sheath potential accelerates ions toward the electrode surfaces, enabling

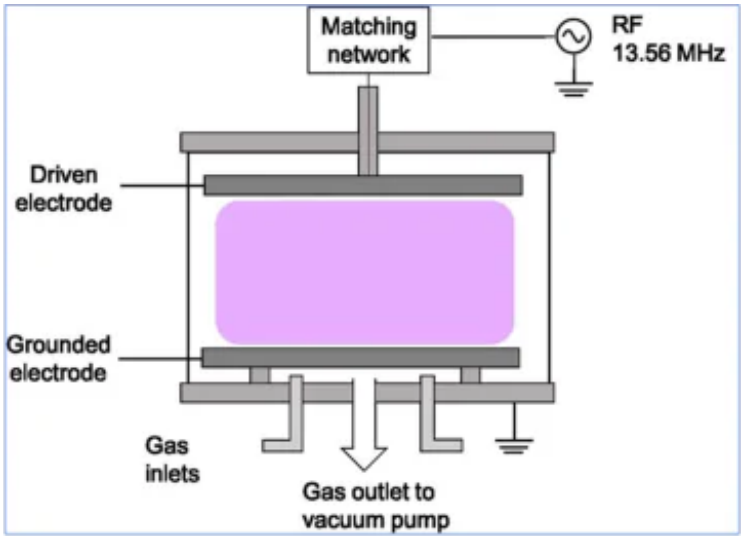

Figure 1.11: Schematic diagram of a parallel plate Capacitively Coupled Plasma (CCP) system [15]

directional (anisotropic) ion bombardment, which is crucial for applications such as plasma etching and sputtering [4].

Typical CCPs operate at pressures ranging from 10 to 500 mTorr, with electron densities in the range of 10^{15} to 10^{17} m^{-3}. Control of ion energy and flux is achieved by tuning the RF power, gas composition, and electrode configuration.

In this thesis, a variation of the CCP configuration is utilized, where the plasma is generated using a DC power supply instead of an RF source. The setup includes stainless steel electrodes placed at a distance d apart within a cylindrical chamber. Air and argon are introduced as the working gas at a typical pressure and DC voltage to initiate the discharge (Figure 1.12).

Despite being DC driven, the plasma exhibits capacitive characteristics due to the geometry and electrode configuration. Diagnostics such as Langmuir probe and optical emission spectroscopy (OES) are employed to analyze electron temperature, density, and plasma potential under this configuration.

1.4.3 Inductively Coupled Plasma (ICP)

Inductively Coupled Plasmas (ICPs) are high-density, low-pressure plasmas widely used in analytical chemistry and material processing. Unlike CCPs, which rely on capacitive coupling through electrodes, ICPs use inductive coupling via an RF-driven coil to transfer energy into the plasma without direct electrode contact. This minimizes contamination and enables longer operational lifetimes [3, 4].

In an ICP system, an RF current (commonly at 13.56 MHz) is passed through a coil wound

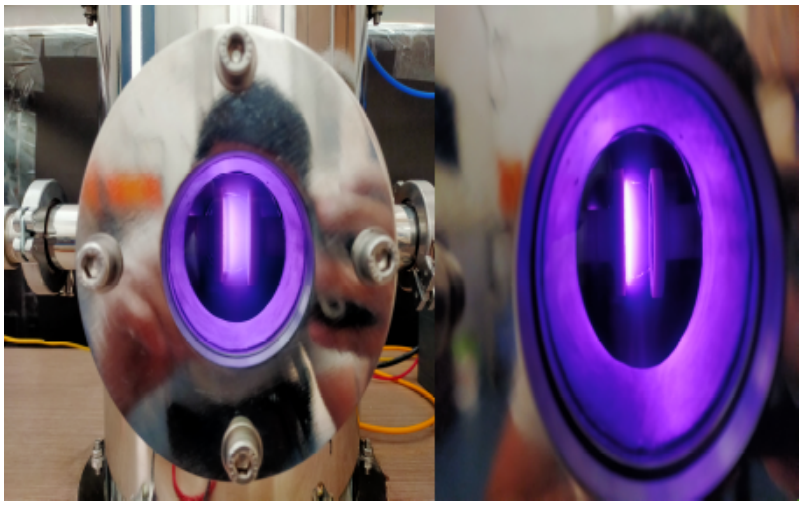

Figure 1.12: Visible plasma glow in the CCP setup driven by a DC power supply, as used for diagnostic experiments in this thesis.

around a dielectric tube (usually quartz). The oscillating current in the coil generates a time-varying magnetic field, which induces an azimuthal electric field inside the discharge chamber via Faraday's law. This electric field accelerates free electrons, which then collide with neutral gas atoms, leading to ionization and sustaining the plasma.

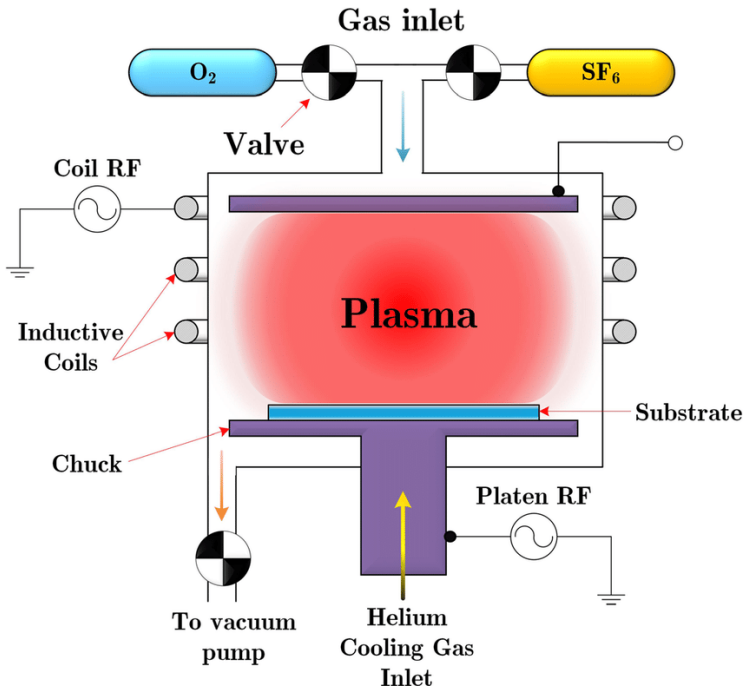

Figure 1.13: Schematic diagram of an Inductively Coupled Plasma (ICP) system. RF current through a coil generates a magnetic field, which induces an azimuthal electric field that sustains the plasma. [16]

ICPs operate efficiently at pressures between 1 and 100 mTorr and can achieve electron densities up to 10^{17} to 10^{18} m^{-3}. Since no electrodes are in contact with the plasma, sputtering and contamination are significantly reduced. Furthermore, the energy delivered to the plasma is uni-

formly distributed, making ICPs ideal for applications that demand high-density, uniform plasmas.

There are two common geometrical configurations:

- **Cylindrical ICP (Axial)**: The coil surrounds the discharge tube along its axis.
- **Planar ICP**: The coil lies flat over the chamber, used for processing flat substrates.

The primary heating mechanism in ICPs is ohmic (or Joule) heating, where electrons gain energy from the induced electric fields and transfer it to the gas through collisions. Unlike CCPs, where sheath acceleration dominates ion energy control, ICPs allow relatively independent control of ion flux and ion energy by combining ICP (for density) and CCP (for bias control) in hybrid systems.

ICPs are extensively used in applications such as Inductively Coupled Plasma Mass Spectrometry (ICP-MS), Inductively Coupled Plasma Optical Emission Spectroscopy (ICP-OES), Plasma-enhanced etching and deposition processes, Nanomaterial synthesis and surface functionalization.

Because the power is delivered inductively—without direct contact between electrodes and plasma i.e., the separation of power source from the plasma boundaries makes ICPs especially suitable for large scale industrial processes and sensitive applications requiring ultra-clean conditions. As a result, ICPs have become a fundamental technology in modern plasma-based material processing.

1.4.4 Microwave Plasma Discharges

Microwave and radio-frequency (RF) plasma discharges offer highly efficient methods for plasma generation, especially in low-pressure environments. These discharges are sustained through the coupling of high-frequency electromagnetic waves with free electrons in the gas, resulting in ionization and plasma formation without the need for direct electrode contact [1, 4].

Microwave Plasmas sources typically operate at a frequency of 2.45 GHz, where energy is delivered to the electrons via oscillating electric fields generated by electromagnetic waves. These plasmas are often sustained in resonant cavities or waveguides using dielectric windows (like quartz) to couple power into the chamber.

Electrons are accelerated by the microwave field and gain sufficient energy to ionize neutral atoms through collisions. One of the key operating modes of microwave plasmas is the electron cyclotron resonance (ECR) mode, where the microwave frequency matches the electron cyclotron

frequency, allowing for resonant energy absorption. This enables extremely high plasma densities (up to 10^{18} m^{-3}) at very low pressures (sub-mTorr).

Microwave plasmas are widely used in Plasma-enhanced chemical vapor deposition (PECVD), Surface modification and cleaning, Materials synthesis (e.g., carbon nanotubes, graphene), Sterilization and biomedical applications

1.5 Debye Sheath

The Debye sheath is a plasma layer characterized by a higher density of positive ions, resulting in a net positive charge that balances the negative charge on a material surface in contact with the plasma. Its thickness is generally multiple Debye lengths, depending upon plasma parameters such as temperature and density. This sheath forms as electrons, being lighter and faster than ions, exit the plasma near the surface, resulting in a negative charge. The Debye length defines the scale of the transition region, and as the potential increases, an increasing number of electrons are reflected until equilibrium is attained, generally at a potential many times the electron temperature. The sheath defines the interface between plasma and a solid surface.

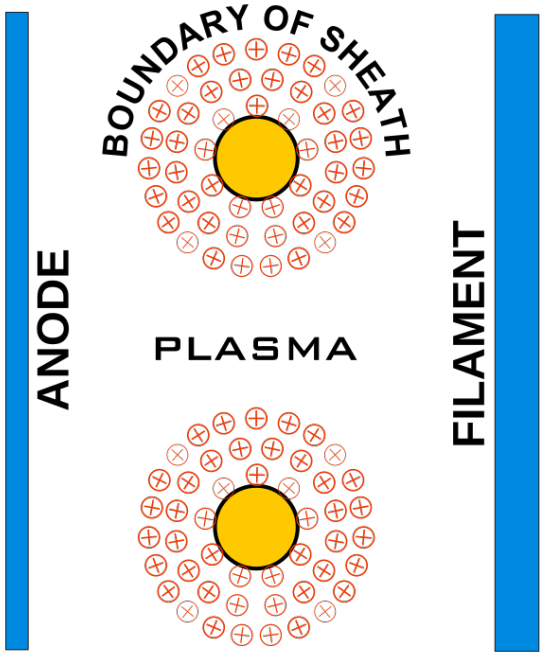

Figure 1.14: Positive ion sheaths around grid wires in a thermionic gas tube, where $\oplus$ represents a positive charge [23].

Langmuir and Albert W. Hull described the development of a sheath in a thermionic valve (Figure 1.14), wherein a wire submerged in plasma at zero potential absorbs both electrons and

positive ions. Due to the significantly higher velocity of electrons compared to ions, the wire receives a substantially greater number of electrons. In order to achieve equilibrium, the wire must attain a negative potential that repels the majority of electrons, allowing an equal influx of electrons and ions to impact it. When the wire is made more negative, it repels electrons and attracts positive ions, forming a sheath surrounding the wire composed solely of positive ions. A potential gradient develops within the sheath, becoming less negative with distance until it matches the plasma potential. This boundary defines the sheath, beyond which the wire's potential fails to influence the plasma [23].

1.6 Plasma Diagnostics: Optical Emission Spectroscopy (OES)

1.6.1 Principle of Optical Emission Spectroscopy (OES)

Optical Emission Spectroscopy (OES) is based on the fundamental principle that when atoms in a sample are excited—typically through spark, arc, or plasma discharge—their electrons are elevated to higher energy levels. Upon relaxation back to lower energy states, these atoms emit photons at element-specific wavelengths. Since no two elements emit at the same wavelength, the spectral lines observed uniquely identify the elements present (Figure 1.15).

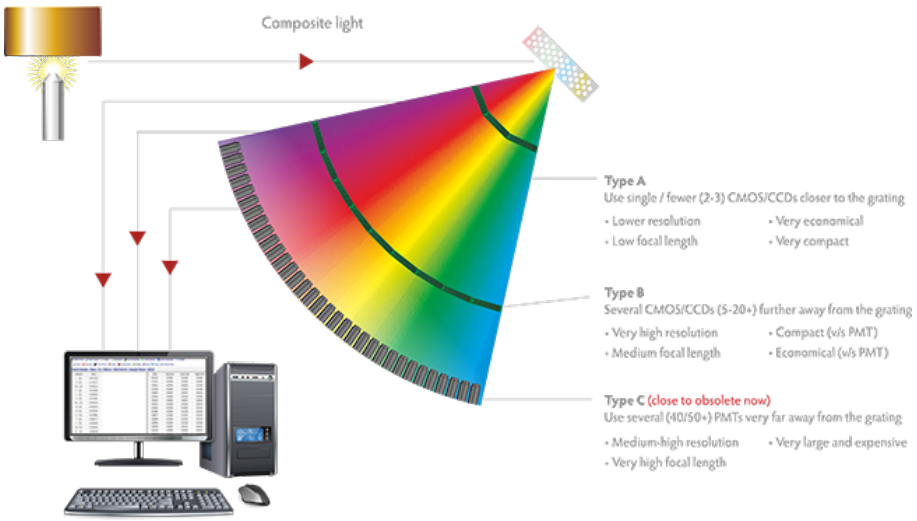

Figure 1.15: Fundamental working principle of OES: excitation of atoms, emission of photons, which are dispersed by a diffraction grating and detected using an array of CMOS/CCD or legacy PMT sensors [17].

Key Advantages of OES:

- Non-invasive and real-time
- Provides both qualitative and quantitative data
- Suitable for various gas compositions and discharge types

In modern arc/spark OES systems, a high-voltage discharge is applied to a sample surface (typically metallic) in an argon-purged environment. This creates a localized plasma that vaporizes part of the sample. The excited atoms within the plasma emit light, which is then directed through a diffraction grating to split it into individual wavelengths. These spectral lines are detected and analyzed using CCD or CMOS detectors, replacing the older PMT (photomultiplier tube) systems. The intensity of each line corresponds to the concentration of that element, allowing for quantitative analysis.

This method is highly effective for determining the elemental composition of solid materials and is especially valued for its precision, speed, and reliability in both research and industrial settings [17].

1.6.2 OES for Determining Plasma Parameters

Optical Emission Spectroscopy (OES) is also a powerful non-intrusive technique for characterizing plasma parameters. It relies on analyzing the electromagnetic radiation emitted by excited atoms or ions in a plasma as they return to lower energy states. These emissions form discrete spectral lines, which are specific to the transitions occurring in different elements present in the plasma. The technique provides valuable insights into plasma composition, electron temperature, and electron density without disturbing the plasma environment [18, 19, 20]. **Applications in Plasma Diagnostics:**

- Identification of atomic and ionic species present in the plasma
- Determination of electron temperature using the Boltzmann plot method
- Estimation of electron density using Stark broadening of spectral lines
- Analysis of excitation and ionization mechanisms

Determination of Electron Temperature: The electron temperature T_e can be calculated using the Boltzmann plot method by measuring the relative intensities of emission lines from the same

species:

$$\ln\left(\frac{I_{ik}\lambda_{ik}}{A_{ik}g_k}\right) = -\frac{E_k}{k_B T_e} + \ln\left(\frac{N}{Z(T)}\right) \tag{1.4}$$

where:

- I_{ik} is the line intensity
- λ_{ik} is the wavelength of the transition
- A_{ik} is the Einstein transition probability
- g_k is the statistical weight of the upper level
- E_k is the excitation energy
- $Z(T)$ is the partition function

Plotting the left-hand side against E_k yields a straight line with slope $-1/(k_B T_e)$.

In the Boltzmann plot analysis, the uncertainties in the measured intensities I_{ik} and the transition probabilities A_{ik} significantly affect the **uncertainty in the logarithmic term** $\ln\left(\frac{I_{ik}\lambda_{ik}}{A_{ik}g_k}\right)$. Assuming that the uncertainties in the degeneracy g_k and wavelength λ_{ik} are negligible, the error in the logarithmic term can be expressed as:

$$\delta\left(\ln\left(\frac{I_{ik}\lambda_{ik}}{A_{ik}g_k}\right)\right) = \sqrt{\left(\frac{\delta I_{ik}}{I_{ik}}\right)^2 + \left(\frac{\delta A_{ik}}{A_{ik}}\right)^2} \tag{1.5}$$

The uncertainties in δI_{ik} and δA_{ik} correspond to the uncertainties in the intensity I_{ik} and transition probability A_{ik}, respectively. The uncertainty in I_{ik} arises from Poisson statistics, as it is derived from the number of counts recorded. On the other hand, the uncertainty in A_{ik} is obtained from literature sources and the NIST Atomic Spectra Database [21].

Determination of Electron Density: Electron density n_e can be estimated from Stark broadening of emission lines. The line width (FWHM), primarily caused by interactions with nearby charged particles, is related to electron density:

$$\Delta\lambda_{1/2} = 2w \times 10^{-16} \cdot n_e \quad \text{(in nm)} \tag{1.6}$$

Comparing measured $\Delta\lambda_{1/2}$ with known values allows one to compute n_e.

The absolute error in the electron density (δn_e) can be expressed as:

$$\delta n_e = n_e \cdot \sqrt{\left(\frac{\delta(\Delta\lambda_{\text{FWHM}})}{\Delta\lambda_{\text{FWHM}}}\right)^2 + \left(\frac{\delta w}{w}\right)^2}$$

where:

- w is the Stark broadening parameter [22].
- δw is the uncertainty in the Stark width w [22].
- $\delta(\Delta\lambda_{\text{FWHM}})$ is the uncertainty in the FWHM measurement.

Plasma Frequency: From the measured electron density, the plasma frequency can be calculated as:

$$\omega_p = \sqrt{\frac{n_e e^2}{\varepsilon_0 m_e}} \tag{1.7}$$

This frequency represents the natural oscillation rate of electrons in the plasma and is crucial for understanding plasma wave interactions.

Debye Length and Number of Particles in a Debye Sphere: The Debye length λ_D represents the scale over which electric potentials are screened in plasma and is given by:

$$\lambda_D = \sqrt{\frac{\varepsilon_0 k_B T_e}{n_e e^2}} \tag{1.8}$$

The number of electrons in a Debye sphere N_D is:

$$N_D = \frac{4}{3}\pi n_e \lambda_D^3 \tag{1.9}$$

Both parameters are essential to ensure the quasi-neutrality and collective behavior characteristic of a true plasma, and were used in the analysis conducted in [19].

References and Data Sources: OES data for this thesis was processed using high-resolution spectrometers, and relevant emission data such as A_{ik}, g_k, and E_k are typically taken from the NIST Atomic Spectra Database [21]. The Stark broadening parameter (ω) and its associated uncertainty (δw) are sourced from the review paper by Konjević et al. [22]. Background correction of raw spectral data (Figure 1.16), spectral line identification, and Boltzmann plotting were implemented to derive key plasma parameters. Analysis techniques and experimental procedures are adapted

from works such as [18, 19, 20], where OES was used to determine plasma characteristics under varying gas pressures and discharge conditions.

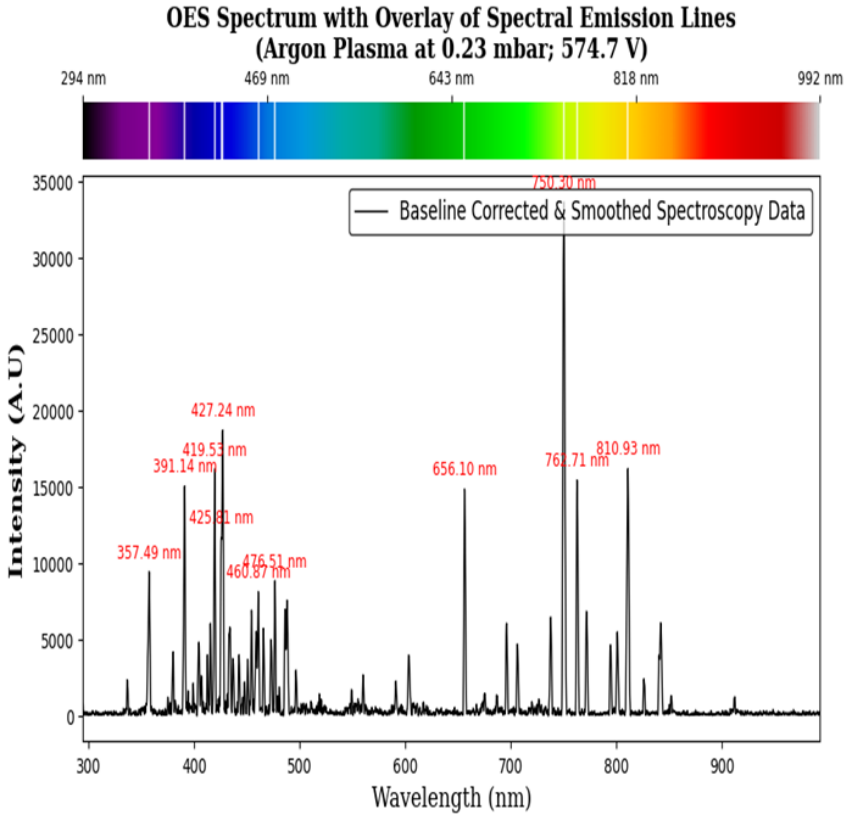

Figure 1.16: Illustration of a baseline-corrected and smoothed optical emission spectrum from argon plasma, with labeled peaks corresponding to various atomic transitions.

OES thus serves as a fundamental technique in plasma diagnostics, especially valuable for characterizing electron temperature, density, and emission behavior in air, argon, and laser-induced plasmas.

Limitations of OES:

- Only radiative (optically active) transitions are observed — non-radiative processes are undetected.
- Accuracy in determining electron temperature and density depends on assumptions (e.g., LTE - local thermodynamic equilibrium).
- Spectral line overlap can hinder precise identification without high-resolution instruments.
- Requires known transition data (A_{ik}, g_k, E_k) from reliable databases such as NIST ASD.
- Stark broadening analysis is often sensitive to instrument resolution and requires calibration.

1.7 Plasma Diagnostics: Langmuir Probe and Its I–V Characteristics

1.7.1 Langmuir Probe

A Langmuir probe is an instrument utilized to determine the plasma parameters such as electron temperature, electron & ion densities and electric potential of a laboratory and even space plasmas. The mechanism involves the placement of one or more electrodes within a plasma system, creating either a steady or fluctuating electric potential between them. The measured currents and potentials in this system helps in elucidating the physical properties of the plasma. The basis of Langmuir probe theory lies in the I–V characteristic of the Debye sheath, which illustrates the current density approaching a surface in plasma as a function of the voltage difference across the sheath. The following section demonstrates the computation of plasma parameters derived from the I–V characteristics curve.

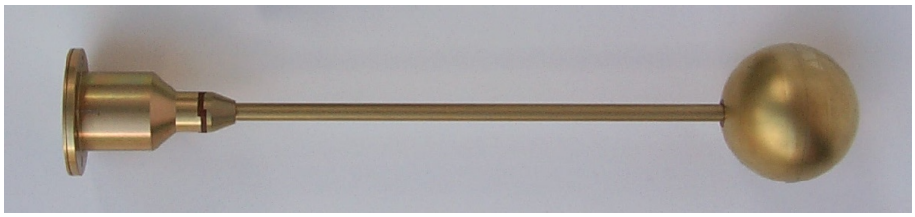

Figure 1.17: The Langmuir probe onboard ESA's space vehicle Rosetta, developed by the Swedish Institute of Space Physics, Uppsala. Spherical probe with 50 mm diameter [24].

1.7.2 I-V Characteristics Of Langmuir Probe

The Langmuir probe's current-voltage (I-V) characteristics provide critical insights into plasma behavior. Let us consider the plasma potential or the space potential denoted as V_s, and the potential applied to the probe end through a circuit is V_p. When the probe potential $V_p \gg V_s$, the probe predominantly collects electron current (I_e), and the net current of the probe becomes negative. Conversely, for $V_p \ll V_s$, the probe collects ion current (I_i). By convention, I-V curves are plotted with electron current (I_e) considered positive and ion current (I_i) negative. Figure 1.18 demonstrates an idealized I-V characteristic curve illustrating these features of different potentials, highlighting five primary regions of interest.

Ion Saturation Region $I_{\mathbf{sat}}$, at the far left of the curve, where the probe repels nearly all

electrons due to a highly negative potential, the current is dominated by ions. **Floating Potential (V_f)** is the point where the collected electron and ion currents are equal, resulting in a net current of zero. **Transition Region** is the intermediate region where the ion current is negligible, and the electron current increases exponentially as the probe potential V_p approaches $V_s - V_p$. This behavior is characteristic of a Maxwellian plasma distribution. Located very close to the "knee" of the I-V curve is **Plasma Potential (V_s)**. **Electron Saturation Region** ($V_p \geq V_s$), where the probe collects electrons at a nearly constant rate, with slow growth in current due to sheath expansion.

As discussed in the next subsections, the I-V curve offers useful plasma diagnostic parameters such as plasma density (n), electron temperature (kT_e), and plasma potential (V_s). [25]

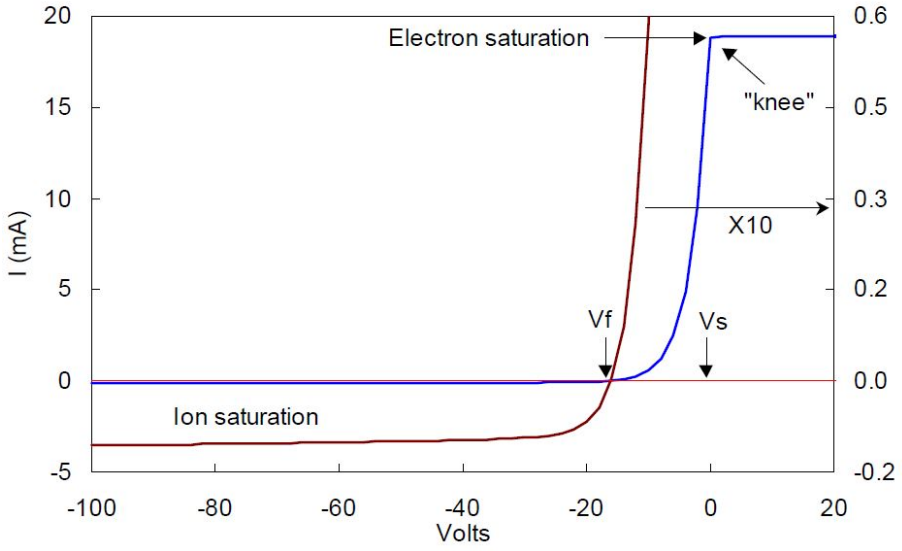

Figure 1.18: An idealized I-V curve for the Langmuir probe. The left curve is expanded 10 times to show the ion current. [25].

1.7.3 The Transition Region Between Electron And Ion Saturation Currents

The exponential region of the I-V curve, when plotted as a semi-logarithmic curve against the potential of the probe V_p, should produce a linear relationship if the electrons adhere to a Maxwellian distribution. This relationship is given by:

$$I_e = I_{\text{es}} \exp\left[\frac{e(V_p - V_s)}{kT_e}\right], \tag{1.10}$$

where,

$$I_{\text{es}} = en_e A\sqrt{\frac{kT_e}{2\pi m_e}}, \tag{1.11}$$

where, A is the probe tip's exposed area and I_{es} is the electron saturation current. Equation (1.10), demonstrates that the slope of the $\ln(I) - V_p$ curve is precisely $\frac{1}{T_{eV}}$ (in units of electron volts, where electron temperature, $T_{eV} = kT_e/e$). Electron temperature (T_e) is one of the easiest plasma parameters to be determined using a Langmuir probe.

For electrons repelled by the probe, the distribution function known as **Electron Energy Distribution Function (EEDF)** at a potential/voltage of $V < 0$ is directly proportional to:

$$f(u) \propto \exp\left(-\frac{m_e u^2}{2kT_e} - \frac{q_e|V|}{kT_e}\right). \tag{1.12}$$

This indicates that $f(u)$ continues to be Maxwellian at the constant electron temperature, while the density diminishes by a factor of $\exp(-q_e|V|/kT_e)$. Therefore, the slope of the semilogarithmic plot does not depend on the probe area or shape and remains unchanged by collisions, as these only maintain the Maxwellian distribution. To obtain electron current (I_e) from the total current I, the ion current (I_i) have to be subtracted. A common approximation involves extrapolating a straight line through the ion saturation current (I_{sat}) into the electron region.

Figure 1.19 presents an observed electron characteristic with a linear fit. The ion current was modeled theoretically using I_{sat} and subsequently subtracted to determine electron current (I_e). The uncorrected data points, illustrating a more restricted portion of linearity, are also presented. In cases where the EEDF is non-Maxwellian, one can sometimes infer its shape from the observed deviations in the semilogarithmic curve [25].

1.7.4 Electron Saturation Region

The exponential growth of I_e in with voltage V_p persists until $V_p = V_s$, at which point no electrons are repelled from the negative potential/voltage, leading to the saturation of the electron current. Given that electron velocities are roughly $(m/M)^{1/2}$ times greater than those of ions, it is anticipated that I_{es} will exceed I_{sat} by a factor of more than 200 (in argon). In low-pressure, unmagnetized, DC discharges of plasma, this remains valid [27], and the "knee" of the I-V curve is distinctly sharp, serving as a reliable indicator of V_s. When $V_p > V_s$, the increase in I_e occurs gradually as the sheath thickness expands, iwhich depends on the probe tip's geometry.

This optimal scenario is rarely observed in real-world devices. Collisions and magnetic fields

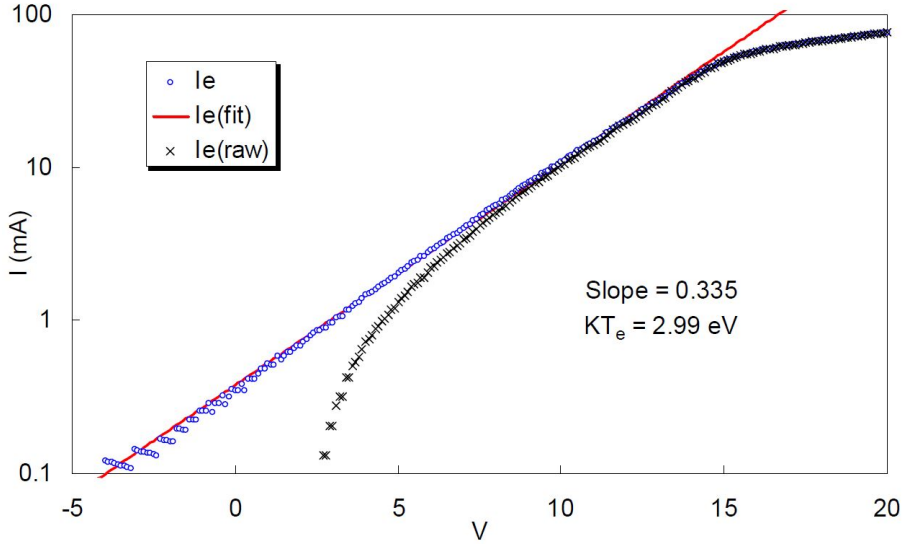

Figure 1.19: A semilog plot illustrating the electron current derived from an I-V characteristics curve within a plasma environment. The lower curve represents the raw data prior to the subtraction of the ion current from the total current [26]

can reduce I_{es} and smooth out the knee, making it difficult to determine V_s. In magnetized plasmas, when the electron Larmor radius is less than the probe radius, I_{es} can be merely 10-20 times I_{sat}. The probe reduces the magnetic field lines it encounters, and further electrons are gathered only via a diffusion across the magnetic field. In this scenario, the $I-V$ curve exhibits exponential behavior for just a few kT_e above the floating potential, thereby capturing only the tail of the Maxwellian distribution. Collisions may also limit the precise determination of I_{es} [25].

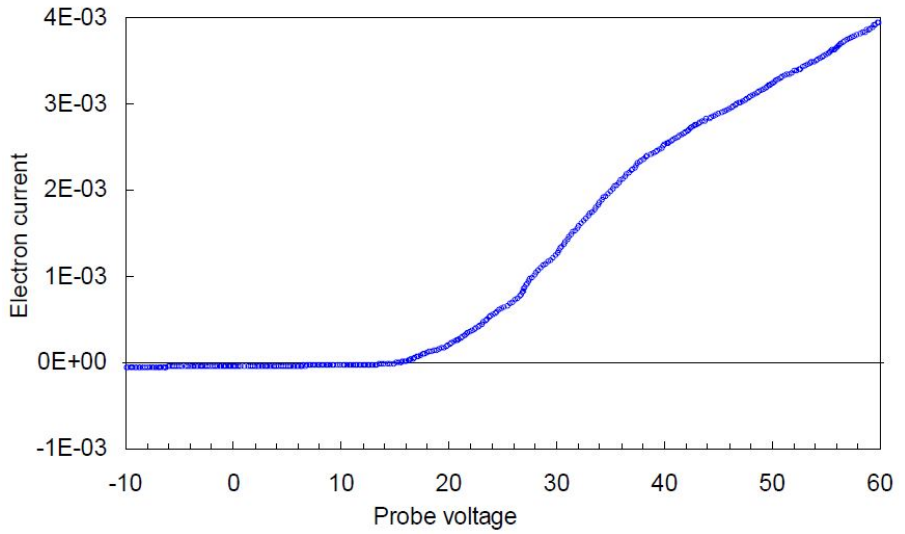

Figure 1.20: Characteristic curve in a magnetized plasma.The knee is represented by a slight bend where I_e is merely 10-30 times the ion current [25, 26] .

1.7.5 Floating Potential (V_p)

V_f is a potential at which the current due to ion collection equals the current due to electron collection i.e., $I_i = I_e$, where I_e is electron current, given by Equation (1.10) and Equation (1.11), assuming the electrons follow a Maxwellian distribution. The ion current, I_i, can be calculated from theories discussed in a later section but can also be estimated using the Bohm current [1]:

$$I_B = \alpha n_e A c_s, \quad c_s \equiv \sqrt{\frac{KT_e}{M}}, \quad \alpha \approx 1/2, \tag{1.13}$$

where M is the mass of ion, n_e is the electron density, A is the probe's collection area, c_s is the ion sound speed, and α is a proportionality constant. The current is generated as a result of the electric field present in the presheath, which accelerates ions to a velocity comparable to the velocity of sound (c_s), the minimum necessary for sheath formation. Equating Equation (1.10) and Equation (1.13), provides a relation given as:

$$V_f = V_s - \frac{KT_e}{2e} \ln(\frac{2M}{\pi m}), \tag{1.14}$$

Value of $V_f - V_s$ is approximately $-3.5T_{eV}$ for plasma based on hydrogen gas and $-5.4T_{eV}$ for plasmas based on argon gas. The above equation only applies to the planar probes. For cylindrical probes, a geometrical correction [28] modifies this value. For example, the value of $-5.4T_{eV}$ is changed to a value between $-4T_{eV}$ and $-5T_{eV}$, depending on the ratio of the probe radius to the Debye length.

1.7.6 Space Potential (V_s)

The traditional method for determining the space potential/plasma potential), (V_s), involves drawing a linear fit through the I-V curve in the transition region and electron saturation regions, with the intersection point defining V_s and I_{es}. However, the above mentioned approach becomes inaccurate if we get curved I_{es}.

In such cases, two alternative methods can be employed, and are described as:

- To measure the floating potential V_f and then calculate V_s using Equation (1.14).
- To identify the point where the electron current I_e begins to deviate from the exponential growth, which corresponds to the point where the derivative of electron current ($I'_e(V)$) is

maximum or the double derivative of the electron current ($I_e''(V)$) is zero. If $I_e'(V)$ has a distinct maximum, a reasonable estimate of V_s can be obtained, as illustrated in Figure 1.21

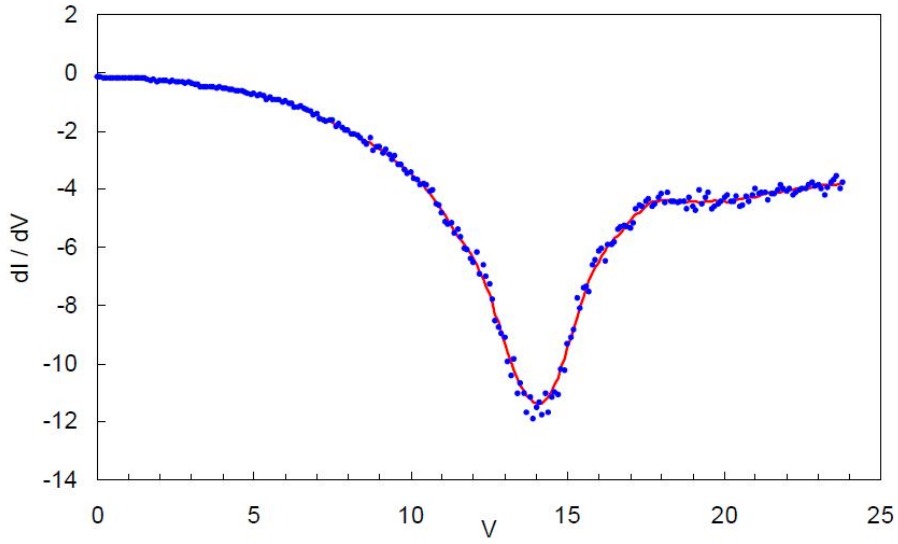

Figure 1.21: Derivative of an I-V curve that has a distinct minimum point at space potential (V_s) [25].

It is important to note that equating the current at this point to I_{es} in order to compute the electron density, n_e, is not reliable for two reasons. Firstly, the knee of the curve can occur before V_s is reached. Secondly, as shown in Equation (1.10) I_{es} depends exponentially on the assumed value of V_s, so a small error in V_s leads to a significant error in the inferred electron density. Therefore, the only accurate way to determine V_s is to use a hot, or emitting, probe for which $V_f \approx V_s$.

1.7.7 Ion Saturation Current

Measuring plasma density n using the electron saturation current I_{es} can be quite inaccurate and may result in dangerously large probe currents, particularly in dense plasmas. In contrast, ion saturation currents I_{sat} are significantly smaller and easier to handle due to the low output impedance they provide. However, interpreting the I_{sat} curve involves substantial computation, and even under optimal conditions, measurements of n using I_{sat} have an uncertainty of approximately 10%.

The simplest approximation for I_{sat} is applicable to planar probes or probes with large ξ_p, where ξ_p is the ratio of the probe radius R_p to the Debye length λ_D:

$$\xi_p = \frac{R_p}{\lambda_D}, \quad \lambda_D = \sqrt{\frac{\epsilon_0 K T_e}{e^2 n_e}} \tag{1.15}$$

At plasma densities above 10^{11} cm^{-3}, the sheath around a negatively biased probe becomes so thin that the area of the sheath edge is nearly equal to the probe tip area. In this regime, the ion current satisfies the Bohm sheath criterion of Equation (1.13), where, α is the ratio of the density at the sheath edge (n_s) to the main plasma density (n). The theoretical value of α is approximately $e^{-1/2} \approx 0.61$, but experimentally calibrated values range from 0.6 to 0.7. For flat probes, I_{sat} is predicted to be constant, as the sheath area does not expand significantly as the probe is made more negative. However, in practice, I_{sat} often exhibits a slope due to the ion current originating from a disturbed presheath volume, where the ion distribution transitions from isotropic to unidirectional. For a disk-shaped probe of radius R, the disturbed volume increases with the magnitude of the probe voltage $|V_p|$. In such cases, extrapolating I_i back to V_f provides a better estimate of I_{sat}, as illustrated in Figure 1.22. This approach compensates for presheath expansion effects.

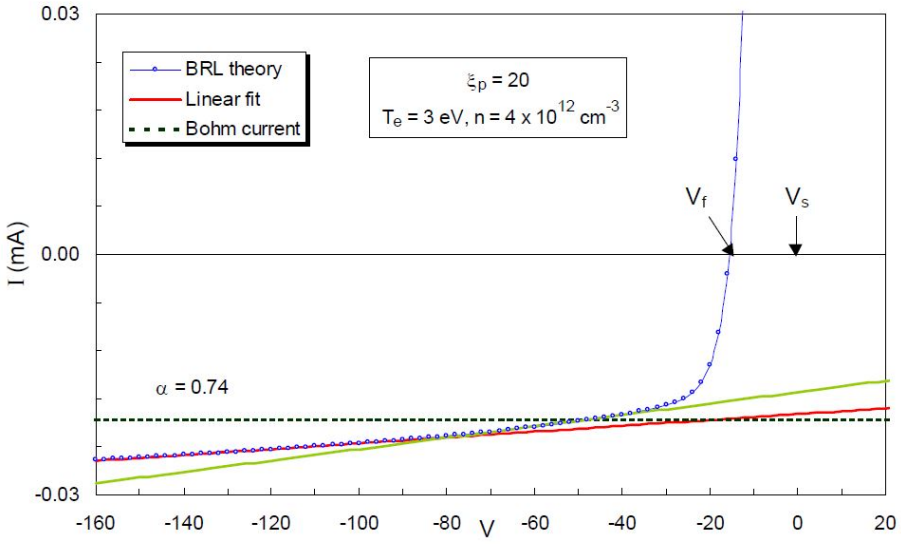

Figure 1.22: Ion saturation current extrapolation to V_f for better estiamtion of saturation current (I_{sat}) [25].

To achieve better saturation characteristics, especially with planar probes, a guard ring can be employed. This is a flat, washer-shaped disk surrounding the probe, biased to the same potential as the probe to maintain planar fields as V_p varies. The current to the guard ring is disregarded.

1.8 Motivation Behind This Thesis Work

Plasma, often termed the fourth state of matter, plays a central role in both natural environments and advanced technological applications. From the sun's core to microelectronic fabrication, plasma behavior underpins critical processes that demand precise control and understanding. However, due to its complex nature involving charged particles, sheath dynamics, and non-linear phenomena, the accurate characterization of plasma remains a scientific and engineering challenge.

This thesis investigates low-temperature and low-pressure air and argon plasmas using two widely adopted diagnostic techniques: Langmuir probe analysis and Optical Emission Spectroscopy (OES). The primary objective is to design and implement a reliable diagnostic framework that can extract key plasma parameters such as electron temperature, electron density and plasma potential.

Langmuir probes offer localized, high-resolution information through current-voltage (I–V) characteristics, while OES provides non-invasive spectral data that enables cross-verification of electron temperatures and species identification. Together, these methods form a powerful diagnostic suite, capable of uncovering both microscopic and macroscopic features of the plasma.

The motivation for this study stems from the need to develop diagnostic tools that are experimentally accessible, yet robust enough to characterize plasma behavior in controlled laboratory conditions. Particular focus is given to low-temperature glow discharges in air and argon environments, which are widely used for surface processing, basic plasma physics research, and pre-fusion experimentation. The insights obtained through such diagnostics not only validate theoretical models but also help refine plasma sources for future applications in both research and industry.

1.9 Organization of the Thesis

The thesis begins with Chapter 1, which introduces the fundamental concepts of plasma physics, covering plasma types, natural and laboratory manifestations, and commonly employed generation methods. It also outlines the motivation behind the present study and introduces the diagnostic techniques used. Chapter 2 reviews relevant literature in the field of plasma diagnostics, focusing on Langmuir probe systems and Optical Emission Spectroscopy (OES). It identifies research gaps and defines the scope and objectives of this work. Chapter 3 describes the experimental setup, including the design of the plasma chamber, power supply configuration, electrode arrangement, and the overall measurement environment. Chapter 4 explains the application of OES for

plasma diagnostics. It presents the underlying principles, data acquisition methods, and analysis techniques used to determine electron temperature and density from emission spectra. Chapter 5 is dedicated to Langmuir probe diagnostics, detailing the probe design, theoretical background, equivalent circuit analysis, and the extraction of plasma parameters from the I–V characteristics. Chapter 6 provides a comprehensive discussion of the experimental results obtained from both diagnostic techniques, highlighting trends, comparative analysis, and sources of error. Chapter 7 concludes the thesis by summarizing the key findings and outlining possible directions for future work, including the refinement of diagnostic tools and the extension of this study to other plasma regimes.

Chapter 2

Literature Review of Past Work and Problem Formulation

2.1 Review of Plasma Generation Techniques & Chamber Design Approaches

Sudit and Woods (1993) [27] developed a sophisticated Langmuir probe system integrated with a VAXStation 3200 graphics workstation for characterizing low-pressure DC and microwave plasmas. Their experimental setup included a 3-meter-long, 15.2 cm diameter Pyrex discharge tube with water-cooled electrodes and a solenoidal magnet providing axial magnetic fields up to 440 G. Precise pressure and flow control (via MKS 1159B controller and MKS 120 manometer) enabled stable discharge conditions in the range of 5–200 mTorr, 500–1500 V, and 20–2000 mA.

In 1994, Sudit and Chen [42] introduced an RF-compensated Langmuir probe system tailored for high-density RF plasmas where strong RF fluctuations of nearly 100 V often distort probe readings. Their experiments were conducted in a helicon discharge (27.12 MHz, 2 kW) in a 1.6-meter-long quartz tube under axial magnetic fields up to 0.13 T and argon pressures between 7.5–10 mTorr, producing plasmas with electron densities around 10^{13} cm^{-3}.

Carey et al. (2010) [29] studied anomalies in Paschen's law at high pd values using a G10 high-pressure housing capable of up to 13.8 MPa. Their chamber, with stainless steel spherical electrodes (2.54 cm diameter), allowed testing of gap distances (0.508–2.54 mm) with N_2, H_2, and SF_6 gases. A 125 kV Glassman power supply, ramped over 120 seconds, facilitated precise breakdown studies over a broad pressure range (96.5–6900 kPa).

Loureiro et al. (2010) [30] developed a compact Paschen curve experiment using a remote-controlled setup with horizontally embedded parallel electrodes (gap ≈ 4.5 mm), a 3.5 kV DC power supply, and a turbo-molecular vacuum pump. Gas flow and pressure were managed via electro-pneumatic valves, and optical access was enabled via a front-facing webcam for visual plasma confirmation (Figure 2.1a).

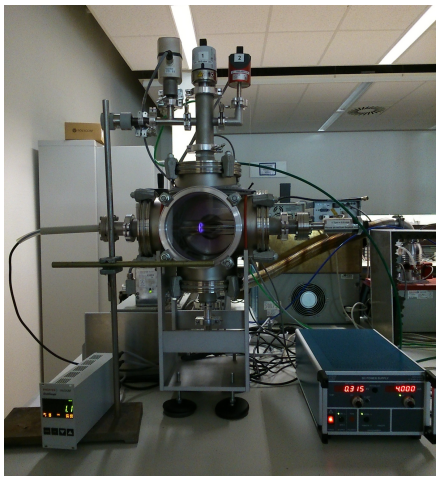

(a) Photograph of the experimental setup. The central component is the main plasma chamber, with the pressure gauge controller positioned on the left and the power supply unit on the right (Loureiro et al.) [30].

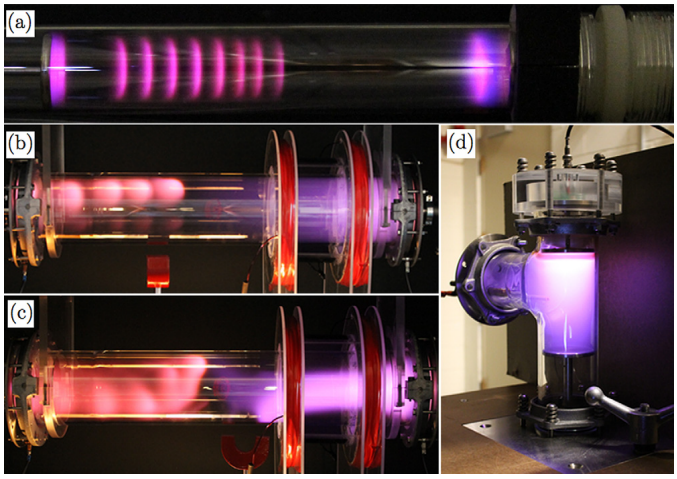

(b) Educational plasma setups based on DC glow discharges: (a) a basic introductory system for lab demonstrations, (b) & (c) advanced configurations incorporating magnetic fields for field–plasma interaction studies, and (d) a system equipped with Langmuir probes for diagnostic measurements (Wissel et al.) [31].

Figure 2.1

Wissel et al. (2013) [31] presented a modular DC glow discharge system for undergraduate education, featuring glass vessels with stainless steel electrodes, powered by 2000 V supplies through 50–100 kΩ ballast resistors. The setup enables a wide pressure range (3–300 Pa), supporting studies of Paschen curves, magnetic field effects, and Langmuir probe diagnostics (Figure 2.1b).

Mathew et al. (2019) [32] analyzed the effects of electrode separation and radius on breakdown voltage in argon plasmas. Using an 80 cm long, 30 cm diameter stainless steel vacuum chamber with adjustable Wilson feedthrough electrodes, they verified a modified Paschen's law that includes the d/r ratio. Their system operated with a 1000 V DC supply and pressures in the millibar range.

Galli et al. (2019) [33] explored Paschen's law deviations at high temperature and pressure using a chamber capable of 650°C and 40 bar. With spherical stainless steel electrodes (1.6 cm diameter, 3 µm roughness) and precision micrometer adjustment (50 µm–6.6 mm), their setup supported breakdown measurements under extreme conditions.

Chen et al. (2020) [34] developed a hybrid diagnostic system combining Langmuir probe and Optical Emission Spectroscopy (OES) for microwave plasma. Their setup used a 2.45 GHz

magnetron (400–800 W) in a coaxial waveguide chamber with KF flanges for diagnostic access.

Pambudi et al. (2020) [20] investigated RF argon plasma sputtering (2 MHz) using OES for the determination of electron temperature and electron density. They operated at 120 V RF voltage, 60 mL/min argon flow, and 10–20 Pa pressures, showing both temperature and density decrease with increasing pressure.

Palomares et al. (2022) [35] conducted breakdown voltage studies in ethanol, methanol, and mixtures using a cylindrical aluminum chamber with copper electrodes (3–5 cm diameter) and variable gaps (0.5–2.5 cm). Experiments confirmed the geometry-modified Paschen behavior for organic vapors at pressures ranging from 0.07–5.00 Torr.

Kadhim et al. (2022) [19] characterized cold argon plasma jets using OES in a dielectric-barrier discharge device with a 15 cm Pyrex tube and copper electrodes under 10–18 kV AC. Spectra were analyzed using a 50 µm optical fiber and Surwit S3000-UV-NIR spectrometer.

From the aforementioned literature review of experimental studies, it is evident that plasma generation techniques—whether for Langmuir probe diagnostics, OES analysis, or Paschen curve experiments—rely critically on well-designed plasma chambers. These setups vary in size, pressure regime, power source, and configuration depending on the intended application, ranging from educational tools and basic diagnostics to advanced research under extreme conditions.

2.2 Review of Optical Emission Spectroscopy (OES) in Plasma Diagnostics

The fundamental basis for interpreting plasma spectra was established by J. Cooper (1966)[38], who emphasized that emitted radiation from ionized gases depends not only on atomic transitions but also on plasma environment effects such as Coulomb interactions. These interactions shift energy levels, broaden spectral lines, and influence population distributions. The work laid essential groundwork for later diagnostics under both Local Thermodynamic Equilibirium (LTE) and non-LTE conditions.

For accurate electron density determination from spectral line broadening, the Stark broadening parameter w is critical. Konjević et al. (2002) [22] provided a critically reviewed dataset of Stark widths and shifts for numerous atomic and ionic species, offering a reliable foundation for FWHM-based OES plasma diagnostics of electron density.

Blue et al. (2010) [39] documented the implementation and sustainability of an advanced un-

dergraduate laboratory course on atomic and molecular spectroscopy. While educational in scope, their approach underscores the value of hands-on training with spectrometers and their diagnostic techniques. Their course framework, focused on connecting spectra with quantum structures, offers a scalable model for designing OES-based plasma diagnostics modules in both research and education.

Pambudi et al. (2020) [20] applied OES to analyze argon RF plasma sputtering during carbon thin film deposition. By using Boltzmann plots for T_e and Stark broadening for n_e, they observed a decrease in both parameters with increasing pressure, demonstrating OES's sensitivity to background conditions. The combination of neutral Argon I (Ar I) and ionized Argon II (Ar II) spectral lines, identified via NIST Atomic Spectra Database, further validates the method's effectiveness in thin-film processing environments.

Chen et al. (2020)[34] developed a hybrid diagnostic approach combining OES and Langmuir probes for microwave plasmas. They showed that spectral data can compensate for errors due to probe contamination, making OES a valuable backup or supplement in such environments.

Mohammed et al. (2021)[40] investigated Nd:YAG laser-induced plasmas in Cu, Zn, and CuZn alloys. They observed non-linear trends in electron temperature due to matrix effects, while electron density increased with laser irradiance, demonstrating OES's diagnostic capability even in complex material systems.

Savard et al. (2022) [37] conducted a comparative study of OES and Langmuir probes in a helium-based volume-cusp filament ion source. Using a collisional-radiative model with radiation trapping and non-Maxwellian EEDFs, they benchmarked OES results against invasive probe data. Although trends were similar, discrepancies under varying arc voltages revealed OES's limited sensitivity to energetic electrons from the cathode sheath, demonstrating the importance of combining diagnostics for comprehensive characterization.

Kadhim et al. (2022) [19] used OES to study cold argon plasma jets generated by an AC high-voltage dielectric-barrier system. Spectra were analyzed via a Surwit S3000-UV-NIR spectrometer, and plasma parameters were determined using intensity ratios and Stark broadening. Their results showed a slight rise in T_e (0.130–0.142 eV) and a significant increase in n_e (from 4.5×10^{17} to 9×10^{17} cm^{-3}) with voltage. Additional calculations of plasma frequency and Debye parameters affirmed OES's utility in low-temperature plasma applications like biomedical and material surface treatments.

Mazen et al. (2023) [41] employed a self-designed Cherny-Turner spectrometer to determine

electron temperature in argon discharges using the Boltzmann plot method. With a spectral resolution of 0.7 nm, they evaluated power-dependent variations in T_e under constant pressure (6.5 Torr), selecting argon emission lines (706–912 nm) referenced from the NIST database. This study showcased how cost-effective spectrometers can be employed for reliable OES-based diagnostics in controlled plasma environments.

As these studies collectively demonstrate, OES serves as a powerful, non-invasive diagnostic method for estimating key plasma parameters such as electron temperature (T_e) and electron density (n_e). Its applicability spans a wide range of plasma environments—from cold jets to high-power laser-induced plasmas. Though low-temperature plasmas often exhibit non-equilibrium behavior, the use of Boltzmann plots remains valid under the assumption of LTE-like behavior, as supported by collisional-radiative modeling in several studies. Additionally, the accurate use of databases like NIST and the integration of broadening parameters like those from Konjević et al. ensure reliability and repeatability in plasma diagnostics.

2.3 Literature Review Regarding Langmuir Probe

The Langmuir probe is among the best-known and most widely employed plasma diagnostic techniques for characterizing a wide range of laboratory and space plasmas. Its application has evolved with advancements in both experimental requirements and probe technology.

Sudit and Chen (1994) [42] developed a Langmuir probe equipped with Radio Frequency (RF) compensation to address the challenge of accurate electron temperature measurements in high-density RF discharges, where the RF potential ($\sim$100 V) can significantly exceed the electron temperature ($\sim$4 eV). Their probe design employed carbon-based graphite tips to minimize erosion from ion sputtering and incorporated miniature chokes with high RF impedances (150 kΩ at 27.12 MHz and 300 kΩ at 54.24 MHz). The probe assembly and RF compensation circuitry, illustrated in Figure 2.2, provide an optimized configuration for accurate measurements in such environments.

This probe system's equivalent circuit, including the plasma sheath and compensation network, has been simulated and experimentally validated in Chapter 3 of this thesis to produce reliable I–V characteristics for analysis.

In an earlier study, Sudit and Woods (1993) [27] developed a specialized Langmuir probe system tailored for precise diagnostics in low-pressure DC and microwave plasma environments. Their diagnostic system featured cylindrical probes and a transformer-coupled isolation ampli-

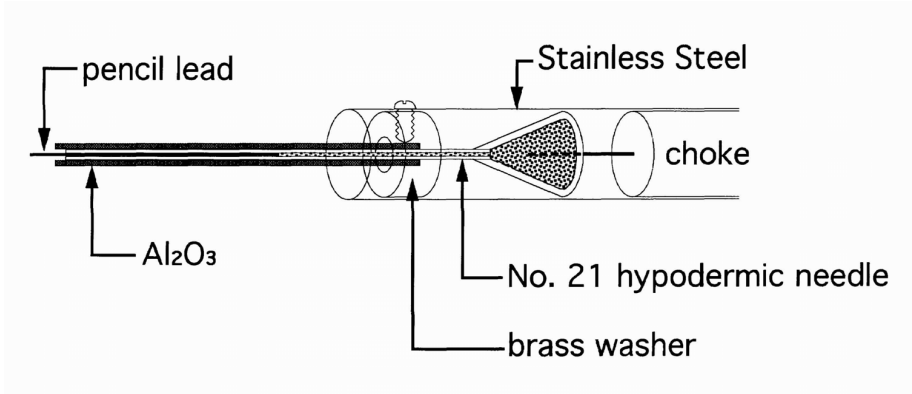

Figure 2.2: Probe assembly with graphite needle and RF compensation circuitry [42].

fier, enabling measurements in plasma regions with large potential differences from ground. An additional compensation probe helped suppress RF-induced noise, significantly improving measurement fidelity. Data acquisition was carried out through high-speed DMA and analyzed using a FORTRAN-based graphical interface to extract plasma potential, electron density, and electron energy distribution functions (EEDFs). Their work remains a reference for probe diagnostics in extended glow discharge systems.

Recognizing the growing complexity of modern plasma experiments, Conde (2011) [43] contributed a comprehensive thesis discussing advanced Langmuir probe geometries, including spherical and double cylindrical configurations. His work emphasizes practical and laboratory applications, highlighting the adaptability of Langmuir probe designs to suit various plasma conditions.

Chektybayev et al. (2022) [36] implemented an automated cylindrical Langmuir probe within a PBI to investigate radial variations of electron temperature (T_e) and density (n_e) in hydrogen plasmas. The system enabled real-time I–V curve analysis, revealing parameter variations with beam energy and pressure, aligning with studies in linear plasma devices. Their system also integrates additional diagnostics such as OES, pyrometry, and mass spectrometry, enhancing its utility for fusion-relevant material interaction research.

The IEEE conference paper by Bigelow et al. (2023) [44] presented the design and testing of a CubeSat-compatible Langmuir probe system for space plasma diagnostics. This 3D-printed sensor incorporates single, double, and triple Langmuir probe configurations to enable high-resolution plasma characterization in **ionospheric environments**. Their innovative, miniaturized multi-probe setup highlights the adaptation of Langmuir diagnostics for compact space platforms.

Similarly, Bekkeng et al. (2019) [45] developed a multi-needle Langmuir probe (m-NLP) with support from the European Space Agency (ESA) for space-based plasma diagnostics. Designed for

CubeSat deployment, the m-NLP offers enhanced spatial resolution and was built using advanced fabrication techniques. The novelty in this research is building a state of the art multi-needle probe sensor which can be utilized on CubeSats for plasma diagnostics [46].

The Langmuir probes are also required for **Indian Space Missions** to study space plasma characteristics. ISRO scientists Vipin K. Yadav and D. Bora [47] designed and developed Langmuir probes specifically suited for hazardous and extreme space plasma conditions. Two distinct probes were created: a Langmuir probe for measuring key plasma parameters & a capacitive probe for detecting plasma oscillations. The designs of both probes are illustrated in Figure 2.3. These probes were engineered and fabricated for the characterization of the microwave-produced plasmas. The RF and microwave-produced plasmas are difficult to characterize using ordinary Langmuir probes, which are especially developed for laboratory-based plasmas.

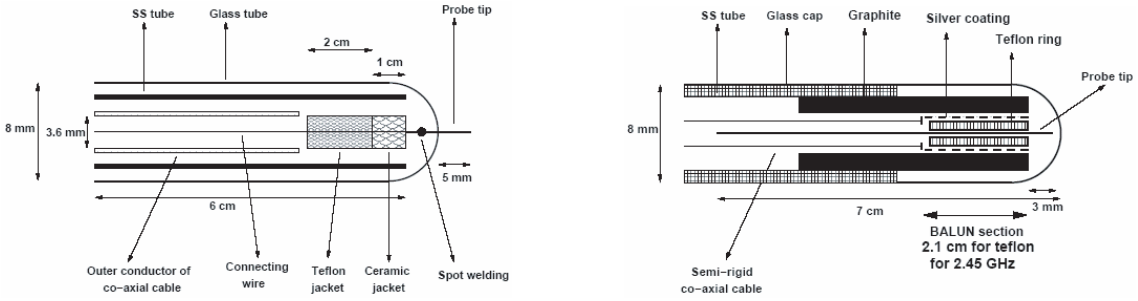

(a) Langmuir probe design. **(b)** Capacitive probe design.

Figure 2.3: Langmuir and capacitive probe designs for space plasma diagnostics [47].

Overall, these advancements reflect a growing trend toward miniaturization, RF-compensation, and multi-diagnostic integration in Langmuir probe design, extending their applicability from basic plasma research to advanced industrial and space-based plasma environments.

2.4 Problem Formulation

As evident from the literature reviewed in previous sections, plasma chambers utilized for diagnostic purposes typically require high-voltage power supplies, ranging from 1.5 kV to 2 kV for educational experiments, and escalating to 10–20 kV for advanced research and industrial applications. Different applications across diverse plasma domains call for different power sources—primarily DC or RF—in order to generate and sustain plasma. However, low-voltage power supplies have rarely been used to investigate plasma properties, largely due to concerns around accuracy, reproducibility, and diagnostic limitations at such operating conditions.

This thesis addresses that gap by demonstrating that meaningful plasma diagnostics and parameter extraction can indeed be performed for low-temperature plasmas generated using a relatively low-voltage DC power source. The plasma parameters obtained under these conditions are found to be comparable in accuracy and significance to those derived from higher voltage systems. The experimental challenges involved in extracting such parameters at low voltages, such as weaker emission intensities, signal noise, and probe sensitivity, are explicitly addressed and discussed. This work, therefore, provides a practical methodology for cost-effective plasma diagnostics suitable for undergraduate and master's level laboratory environments.

Importantly, the research extends into pedagogical impact. The plasma chamber designed and implemented during this thesis is intended to serve as a part of the Astronomy Lab coursework for postgraduate students at IIT Indore. The results, methodologies, and standard operating procedures will be compiled into experiment manuals, thereby enhancing hands-on training in plasma physics and diagnostics at the academic level.

From a diagnostic standpoint, textbfOptical Emission Spectroscopy (OES) was employed to non-invasively estimate key plasma parameters. OES is a fast and convenient technique that allows in-situ diagnostics through emission spectra. However, its data acquisition and analysis process is intricate, requiring careful calibration, knowledge of atomic constants, and the use of models such as Boltzmann plots and Stark broadening analysis. These challenges, and the impact of chamber geometry and gas pressure on spectral quality and resolution, are discussed in detail in the relevant chapter of this thesis. Furthermore, the observed variations of plasma parameters concerning the plasma chamber configuration and gas environment are studied more comprehensively than typically reported in existing literature.

Langmuir probe diagnostics, despite being an established technique, have seen relatively stagnant progress in Indian space-related missions. The Langmuir probes currently deployed in Indian satellite payloads are based on outdated designs and fail to reflect modern advances in miniaturization, real-time data processing, and robustness in hostile environments. This reveals a critical research gap in space-relevant plasma diagnostics. To address this, the present thesis includes the design, fabrication, and implementation of a laboratory-grade Langmuir probe system optimized for low-temperature DC plasmas. The insights derived from this work lay the foundation for adapting such designs for space-like plasma environments, especially in simulating near-Earth plasma conditions using laboratory analogs.

Furthermore, the thesis emphasizes the need to refine our theoretical and practical understand-

ing of probe behavior, particularly the collection dynamics of electrons and ions under low-density, low-pressure conditions. These enhancements are crucial to bridge the current mismatch between theoretical models and modern probe designs, especially in non-Maxwellian or non-LTE plasma systems.

The thesis also attempts to bridge the gap between diagnostic methodologies. Most studies focus exclusively on either Langmuir probe measurements or OES, with very limited integration or cross-validation under the same set of experimental conditions. This project overcomes that limitation by combining both techniques—Langmuir probe and Optical Emission Spectroscopy—for comprehensive diagnostics of air and argon plasmas generated in a custom-built capacitively coupled plasma (CCP) chamber, powered by a low-voltage DC power supply.

This dual-diagnostic approach enables a deeper understanding of the plasma system, helps evaluate the sensitivity of each method to experimental variables (pressure, gas type, electrode geometry), and strengthens the credibility of the extracted results.

Objectives of the Study

The specific objectives of this thesis are outlined as follows:

- To assemble and understand the components of a custom-designed CCP plasma chamber driven by a DC power source.
- To successfully generate low-temperature plasma using a low-voltage DC supply (up to 660 V).
- To perform OES-based diagnostics by analyzing spectral lines and estimating plasma parameters using Boltzmann plot and Stark broadening methods.
- To design and fabricate a Langmuir probe suitable for insertion and operation in the laboratory plasma chamber.
- To extract plasma parameters—electron temperature (T_e), density (n_e), and plasma potential (V_p)—by implementing Langmuir probe diagnostics.
- To perform a comparative analysis between Langmuir probe and OES measurements under varying plasma conditions.
- To develop a practical, reproducible methodology suitable for integration into educational laboratories and advanced plasma research environments.

Chapter 3

The Plasma Chamber & Its Accessories

3.1 Plasma Chamber/Vacuum Chamber

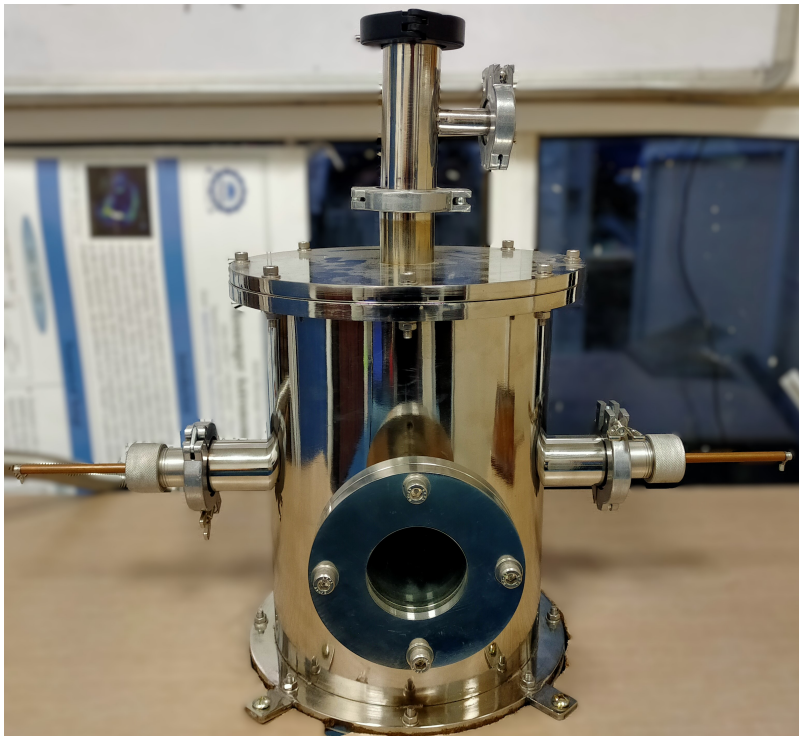

Figure 3.1: Plasma chamber with ports and flanges.

3.1.1 Cylindrical Section Of the Plasma Chamber

The plasma chamber (Figure 3.1) is a cylindrical structure with an outer diameter of 270 mm and a height of 310 mm. It features multiple ports for experimental setups:

i. **Radial Ports for Top and Bottom Flanges:**

Two radial ports of outer diameter of 270 mm are positioned on opposite sides of the chamber. These ports are configured to be sealed with top and bottom flanges (200 CF to 40 KF adapter flange), ensuring secure closure.

ii. **Surface Ports for Viewports:**

Two additional ports (70 mm) are integrated on the surface of the cylindrical chamber. These ports serve as viewports (63 ISO-F) (Figure 3.2), providing optical access for observation, alignment, or diagnostics through plasma-probe interaction.

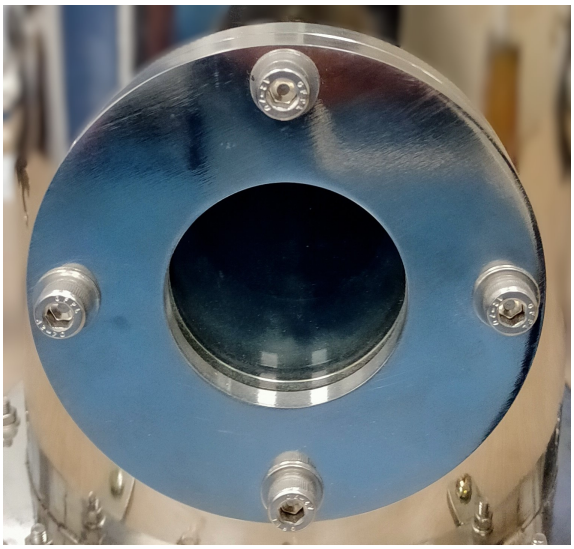

Figure 3.2: 63 ISO-F viewport for plasma observation.

iii. **Axial Ports for Electrodes:**

Two 40 KF ports are located on the surface, aligned along the axial direction of the chamber. These ports facilitate the insertion of horizontally embedded electrodes, which can be adjusted to vary the distance between them.

3.1.2 Top & Bottom Adapter Flange

The top and bottom radial ports of the cylindrical chamber are sealed using **200 CF to 40 KF adapter flanges**. These adapter flanges feature 40 KF ports that are designed to connect with Tee flanges, as described below:

i. **Tee Flange on the Top Adapter Flange :**

A **3-way Tee flange (40 KF to 25 KF)** is utilized, which provides the following configura-

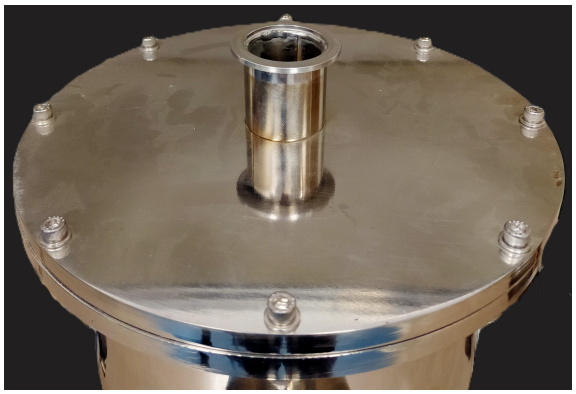

Figure 3.3: Top adapter flange with a 40 KF port for Tee configuration.

tion:

- **Two 40 KF ports** positioned opposite to each other.
- **One 25 KF port** positioned on the side.

The functional details of the ports are as follows:

a) **25 KF Port :**

This port is used to supply argon gas from the gas cylinder. The gas flow is regulated through a needle valve attached to the port.

b) **Bottom 40KF Port :**

This port is connected to the 40 KF port on the top adapter flange, forming a sealed and secure connection to the chamber.

c) **Top 40KF Port :**

This port connects with a 40 KF flange mounted on an instrument called the **Langmuir probe**. The Langmuir probe is employed for plasma diagnostics.

ii. **Tee Flange on the Bottom Adapter Flange :**

Another **3-way Tee flange (40 KF to 25 KF)** is connected to the bottom adapter flange, with the following configurations:

a) **25 KF Port :**

This port is connected to a **vacuum or rotary pump** through ball valve via a vacuum hose. The pump is responsible for evacuating the chamber to achieve the required vacuum level.

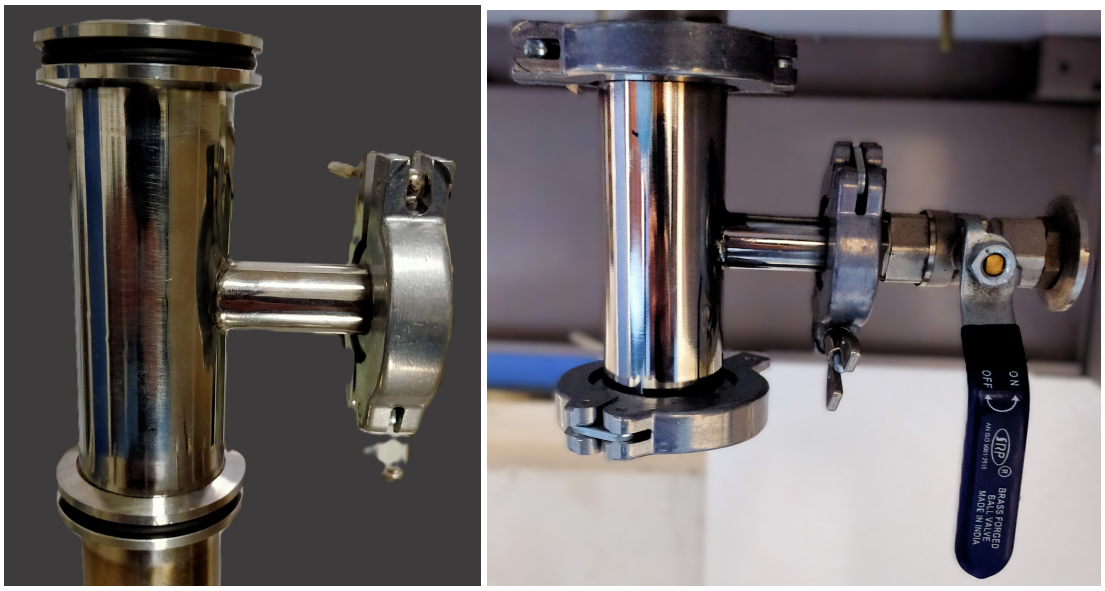

(a) **(b)**

Figure 3.4: (a.) Tee flange on the top adapter flange (b.) Tee flange on the bottom adapter flange.

b) **Bottom 40KF Port :**

This port is connected to the 40 KF port on the bottom adapter flange, forming a sealed and secure connection to the chamber.

c) **Top 40KF Port :**

This port is used to connect a **Pirani gauge (pressure gauge)**. The gauge monitors the chamber pressure to ensure proper vacuum conditions during operation.

3.1.3 Axial Ports for Electrodes

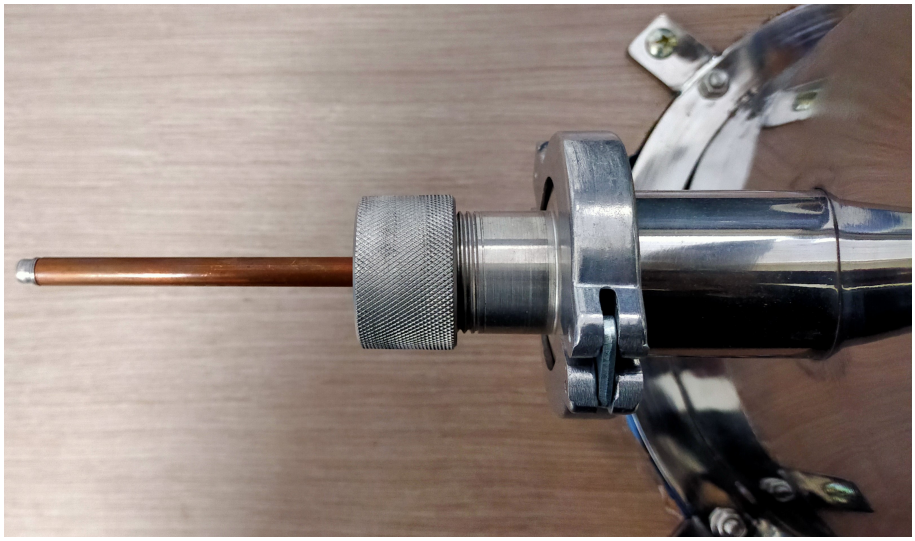

Figure 3.5: High-Voltage Vacuum Feedthrough Installed at the Axial Port of the Plasma Chamber.

i. Adjustable rods are provided for connecting to a high-voltage DC power supply. These rods are designed to allow precise alignment and positioning of the electrodes inside plasma chamber.

ii. A high-voltage **vacuum feedthrough** is integrated into the system to enable safe and reliable transfer of high-voltage power into the vacuum environment while maintaining electrical insulation and vacuum integrity.

iii. **Two parallel plate electrodes**, each approximately 50 mm in diameter, are installed with a fixed gap (d) between them to ensure a uniform electric field, suitable for plasma generation or related experiments.

Figure 3.6: Electrode with Nut to Affix it to the High-Voltage Power Rod.

3.1.4 Clamps

i. A total of **six 40 KF clamps** are provided for securing 40 KF flanges. Additionally, **four spare clamps** are included as backups for replacements if needed.

ii. **Two 25 KF clamps** are supplied with the tee flanges to ensure robust, leak-proof connections.

iii. **Two 25 KF clamps** are included for securing the **vacuum hose**, which connects the 25 KF port on the vacuum pump to the 25 KF port on the ball valve, ensuring a tight and reliable seal.

iv. **Two additional 25 KF clamps** are provided as spares for auxiliary applications.

v. **One 16 KF clamp** is provided along with a KF 25 to KF 16 clamp reducer, which is equipped with a needle valve.

vi. **One additional 16 KF clamp** is supplied for another KF 25 to KF 16 reducer, which can be utilized for the Pirani gauge installation.

(a) **(b)** **(c)**

Figure 3.7: (a.) 40 KF Clamp (b.) 25 KF flange (c.) O ring

3.2 Argon Gas Cylinder

3.2.1 Gas Cylinder

A gas cylinder (Figure 3.8a) with a capacity of **46.7 liters**, filled with **99.999% pure argon gas**, is provided. The cylinder has dimensions of **232 mm outer diameter and 1365 mm length**.

It is supplied by **Vindhya Weld Tech, Indore (M.P.)** and comes with all necessary documentation, including, Purity certificate, Acceptance certificate, Record of hydrostatic stretch test on the cylinder, and Tax invoice.

3.2.2 Gas Regulator

A gas regulator (Figure 3.8b), also supplied by **Vindhya Weld Tech, Indore (M.P.)**, is provided to ensure safe and precise control of the argon gas flow.

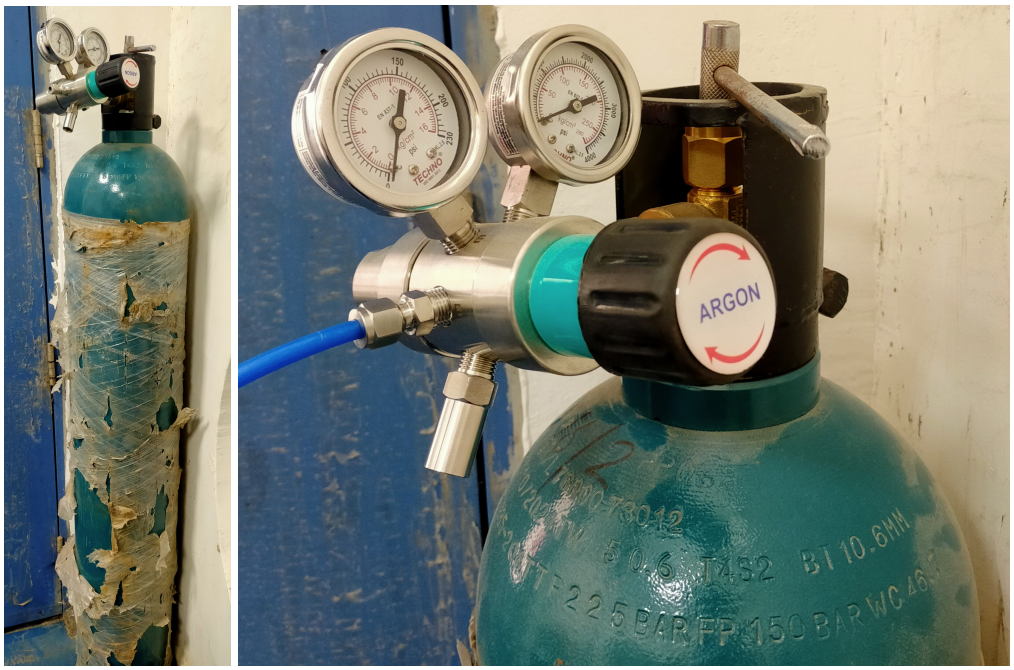

(a) **(b)**

Figure 3.8: (a.) Argon gas cylinder (46.7 litres) (b.) Gas regulator with a 6 mm PVC pipe to facilitate the controlled inlet of gas into the plasma chamber.

3.2.3 PVC Pipe And Needle Valve

A **PVC pipe (6 mm outer diameter)** is provided to connect the gas regulator to the chamber inlet. The connection is made through the **25 KF port of the Tee flange** located on the top adapter flange. A **needle valve** (Figure 3.9) is incorporated to precisely control the flow of argon gas within the chamber.

Figure 3.9: Needle valve to regulate argon gas flow through the chamber.

This setup ensures a reliable supply of high-purity argon gas for experiments, with precise flow

control and robust connections.

3.3 Vacuum Pump / Rotary Pump

A rotary pump connected via a vacuum hose ensures the required vacuum level. The setup includes ball valves for precise control.

- A vacuum pump (Figure 3.10), specifically a rotary pump, is provided with a 25 KF port for connecting a vacuum hose.

Figure 3.10: Vacuum pump setup with a vacuum hose for connection to the plasma chamber.

- A vacuum hose is included to connect the vacuum pump to the plasma chamber. The connection is established through the **25 KF port of the Tee flange** located on the bottom adapter flange. A **ball valve** is incorporated to regulate the outflow of gas, enabling the evacuation of the chamber to achieve the required vacuum level.

3.4 High-Voltage DC Power Supply

- A high-voltage power supply capable of delivering up to **1 kV or 1.5 kV** is required for plasma generation within the chamber.

- For initial plasma experiments a low voltage DC power supply (upto 660 V) from the Electrical Engineering department of IIT Indore is utilized.
- High-quality cable wires are needed to carry current across the plasma chamber, connecting to the electrodes via the rods. Additionally, another cable is required to ground the power supply, and it must be connected to the same ground used to ground the plasma chamber to ensure proper electrical safety and system integrity.

3.5 Digital Pirani Gauge And Gauge Head

A **Pirani gauge** (Figure 3.11) is employed to measure the pressure within the plasma chamber, with a measurement range spanning from **999 mbar to 0.001 mbar**. It is connected through the **40 KF port** of the Tee flange on the bottom adapter flange, with the Pirani gauge head attached.

Figure 3.11: Pirani gauge & gauge head for pressure measurement.

The system includes accessories such as a **25 KF flange**, a **25 KF clamp**, an **O-ring**, an Ethernet cable and a **mains chord**. A **KF 25 to KF 40 clamp reducer** is required to connect the Pirani gauge to the **40 KF port** of the plasma chamber, ensuring proper adaptation and sealing.

3.6 Langmuir Probe Integration and Associated Circuitry

A Langmuir probe has been specifically designed and integrated into the plasma chamber for reliable diagnostics while maintaining vacuum integrity. The probe is mounted on a modified **40 KF flange** attached to the top adapter tee flange of the chamber. A hole is precisely machined in this flange to accommodate a **BNC connector**, which is soldered to the probe cable. This configuration allows the flange to serve as both the mechanical mount and vacuum-sealed electrical feedthrough.

The probe tip is positioned between the electrodes and is visible through the viewport, ensuring direct interaction with the plasma for accurate measurement.

The associated diagnostic circuit includes a **low-voltage DC power supply** for biasing the probe tip, a **series resistor** for current measurement, and a **multimeter** to monitor the voltage across the resistor. The voltage drop is used to calculate the current, enabling the generation of an **I-V characteristic curve**. This curve forms the basis for deriving key plasma parameters.

A detailed account of the design and fabrication of this Langmuir probe, along with the associated electronic circuit box, is provided in Chapter 5.

3.7 Experimental Setup for Plasma Generation and Diagnostics

The experimental setup plays a pivotal role in the successful execution & reproducibility of plasma experiments. Figure 3.12a and Figure 3.12b show, respectively, the schematic layout and the actual laboratory implementation of the setup used for plasma generation and diagnostics in our lab. A DC power supply (up to 660 V) is used to generate plasma between two parallel stainless

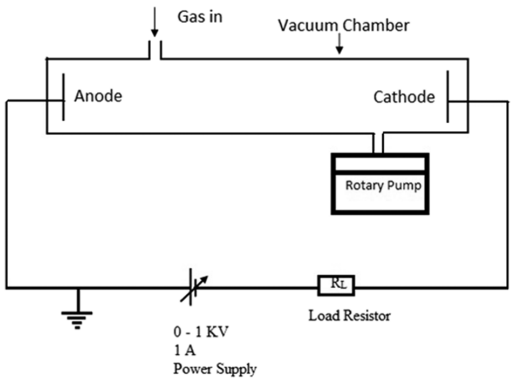

(a) Schematic representation of the experimental setup for plasma chamber diagnostics.

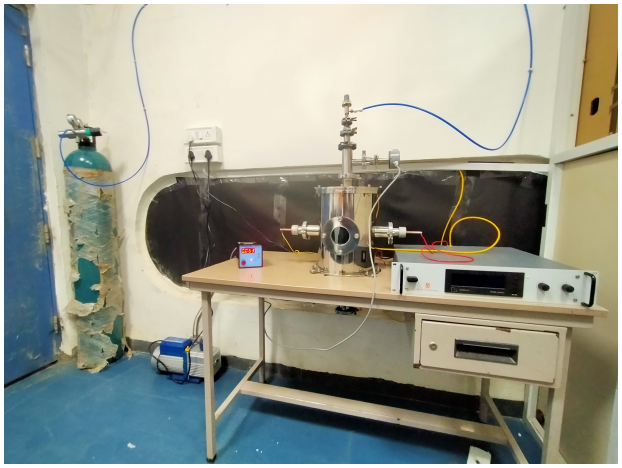

(b) Actual laboratory setup showing the plasma chamber (center), DC power supply, Pirani gauge (left), and vacuum pump and argon gas cylinder (off-frame, right).

Figure 3.12: Overview of the experimental configuration used for plasma generation and diagnostics.

steel electrodes placed inside a custom-fabricated plasma chamber. A Pirani gauge is employed to continuously monitor the pressure inside the chamber, while a rotary vacuum pump evacuates the system to achieve the required low-pressure conditions for plasma generation. For argon plasma,

high-purity argon gas is introduced through a controlled gas inlet connected to an argon cylinder. During air plasma generation, no external gas feed is required, as the chamber is filled with ambient air after pumping down and partially venting.

It is important to note that the Langmuir probe and its associated electronic circuit box are not part of this particular setup. Therefore, this configuration is specifically used for conducting the Paschen's law experiments and for performing Optical Emission Spectroscopy (OES) diagnostics, which will be discussed in detail in the subsequent chapters.

The next section presents visual evidence of plasma formation under both air and argon gas conditions, showcasing the qualitative aspects of plasma glow and behavior under varying experimental parameters.

3.8 Plasma Generation with Air and Argon Gases

Plasma is generated by applying a high-voltage DC power supply (0-660 V) across the **parallel plate electrodes (50 mm diameter)**. The electrodes are affixed to high-voltage rods using nuts and a high-voltage vacuum feedthrough. The distance between the electrodes is maintained at approximately 25–30 mm. However, due to a slight tilt in one of the electrodes, the electrode gap exhibits a degree of non-uniformity across its length/diameter, resulting in a spatial variation in the discharge region.

The steps for plasma generation include:

1. **Evacuating the chamber** to a suitable pressure (10^{-2} mbar) for plasma ignition.
2. **Introducing argon gas** at a controlled flow rate, otherwise plasma can be generated using air.
3. **Applying high voltage** across electrodes to ionize the gas.
4. **Observing plasma formation** through the viewport.

Initially, plasma was not generated between the parallel plate electrodes because the electric field was sufficiently high on the rear side of the electrodes and the copper rod of the feedthrough. This led to plasma formation on the backside of the electrodes and along the chamber walls.

To resolve this issue, the electrodes and copper rods were insulated using cylindrical Teflon jackets that fit around the copper rods and cover the rear surface of the electrodes (Figure 3.13).

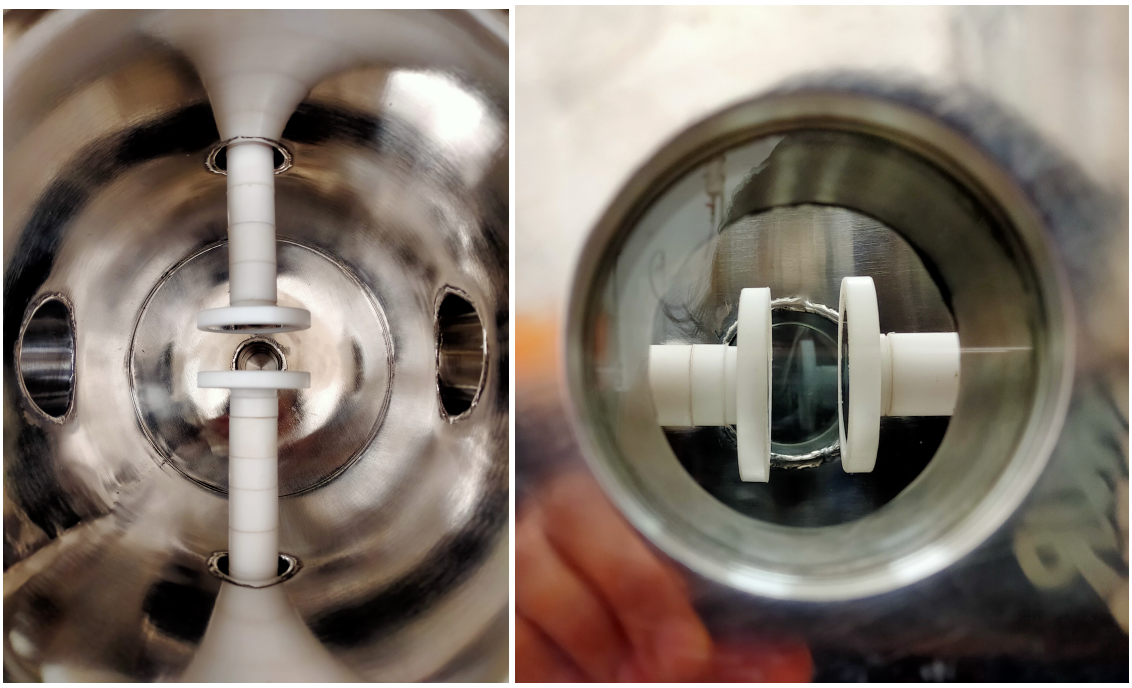

(a) (b)

Figure 3.13: Insulation of the stainless steel electrodes and the copper rods of the feedthrough using cylindrical Teflon jackets.

(a) (b)

Figure 3.14: Plasma generation using (a.) air and (b.) argon as the working gases. The Teflon jackets insulating the rear side of the electrodes are also visible.

After implementing this insulation, plasma was successfully generated using air and argon as working gases inside the chamber (Figure 3.14). This confirmed that the vacuum system, gas flow control, and electrode configuration were functioning correctly.

The generated plasma is characterized through diagnostics employing Optical Emission Spectroscopy (OES) and a custom-fabricated Langmuir probe. Detailed methodologies, analysis procedures, and interpretation of diagnostic results are systematically presented in Chapter 4 (OES) and Chapter 5 (Langmuir probe).

Table 3.1: List of components used in the plasma chamber system.

S.No.	Component	Description	Quantity
1	Cylindrical Section of the Plasma Chamber	Cylindrical section with an outer diameter of 270 mm and a height of 310 mm, featuring two radial ports (OD 270 mm), two surface ports for viewports, and two axial ports for electrode integration.	-
2	Viewport Flange	63 ISO-F viewport flange mounted on the surface ports for optical access.	2
3	Adapter Flange	200 CF to 40 KF adapter flanges designed to interface with the radial ports (OD 270 mm) at the top and bottom of the chamber.	2
4	Tee Flange	Three-way Tee flange (40 KF to 25 KF), installed on the top and bottom adapter flanges, enabling multi-port connectivity.	2
5	40 KF Flange	Flange designed to seal 40 KF ports.	1
6	High-Voltage Vacuum Feedthrough	Provides secure and electrically insulated transmission of high-voltage power into the chamber.	2
7	Electrodes	Parallel plate electrodes made of stainless steel (SS) with a nut for secure attachment to the high-voltage power rod.	2
8	40 KF Clamps	Clamps for securing 40 KF flanges.	10
9	25 KF Clamps	Two Clamps for 25 KF ports on Tee flanges, one for needle valve, one for Pirani gauge and two for securing the vacuum hose on the vacuum pump.	6
10	16 KF Clamps	One clamp used for securing the needle valve and another one for Pirani gauge.	2
11	Gas Cylinder	46.7-liter argon gas cylinder filled with 99.999% pure argon gas (OD 232 mm × Length 1365 mm).	1
12	Gas Regulator	Precision gas regulator fitted to the argon gas cylinder.	1
13	PVC Pipe	6 mm PVC pipe used to connect the gas regulator to the plasma chamber via a needle valve.	1
14	Needle Valve	Needle valve for precise regulation of argon gas flow into the chamber.	1
15	Ball Valve	Ball valve for controlling the outflow of gas through the vacuum pump.	1
16	Vacuum Pump	Rotary vacuum pump with a 25 KF port for chamber evacuation.	1
17	Vacuum Hose	Connects the vacuum pump to the plasma chamber via the 25 KF port of the Tee flange on the bottom adapter flange.	1
18	High-Voltage DC Power Supply	Power supply unit capable of delivering high-voltage DC for plasma generation.	1
19	Digital Pirani Gauge & Gauge Head System	Pirani gauge for measuring chamber pressure, with a range from 999 mbar to 0.001 mbar.	-
20	40 KF to 25 KF Reducer	40 KF to 25 KF clamp reducer used for connecting the Pirani gauge to the 40 KF port of the plasma chamber.	1
21	25 KF to 16 KF Reducer	The KF 25 to KF 16 reducer is used to connect the needle valve to the plasma chamber, while an additional KF 25 to KF 16 reducer is employed for the Pirani gauge installation.	2
22	Langmuir Probe	Probe inserted through the 40 KF port of the Tee flange on the top adapter flange for plasma diagnostics.	1
23	Circuitry System	Electrical circuit for the Langmuir probe, including BNC connectors, BNC cables, resistors, and other essential components.	-

Chapter 4

Plasma Diagnostics: Optical Emission Spectroscopy (OES)

4.1 Overview of Optical Emission Spectroscopy and Spectrometer Components

Optical Emission Spectroscopy (OES) is a non-invasive diagnostic technique extensively used to determine key plasma parameters such as electron temperature (T_e) and electron density (n_e). It analyzes the light emitted by excited atoms and ions within a plasma, utilizing a spectrometer to resolve this light into its constituent wavelengths.

4.1.1 Components and Working Principle of Optical Spectrometer

An optical spectrometer is the core instrument in OES. It captures and disperses light emitted from the plasma, allowing spectral lines to be recorded and analyzed. The key components include:

- **Light Source:** In OES, the plasma itself acts as the emission source, though calibration lamps may be used.
- **Optical Mirrors:** Collimating mirrors (spherical or toroidal) direct the emitted light into the dispersion element. Toroidal mirrors are preferred for minimizing aberrations.
- **Dispersion Element:** A diffraction grating or prism separates the light based on wavelength. Gratings are commonly used due to their high resolution and spectral efficiency.

- **Detector:** After dispersion, light is captured using a CCD, photodiode array, or PMT. CCDs are commonly used for multi-wavelength, high-resolution detection.

4.1.2 Data Acquisition Process

The standard procedure in OES involves:

1. **Emission Collection:** Light emitted from the plasma is directed into the spectrometer using an optical fiber.
2. **Spectral Dispersion:** The collimated light is diffracted into its spectral components.
3. **Detection:** A detector records the intensity of each wavelength, producing an emission spectrum.
4. **Analysis:** Software tools process the spectral data to identify emission lines and compute plasma parameters.

Unlike transmission spectroscopy, OES directly analyzes light emitted by the plasma, making it suitable for real-time monitoring of low-temperature discharges. Modern CCD-based spectrometers offer fast, broad-range detection ideal for dynamic plasma systems.

4.2 Hardware Specifications of the Spectrometer

The performance of an optical spectrometer is determined by several key hardware parameters that collectively influence its sensitivity, resolution, dynamic range, and spectral accuracy. This section outlines the critical specifications of the **Plasma Vacuum Solutions UVH-1 spectrometer** used in this thesis work (Figure 4.1).

4.2.1 Detector

The detector is responsible for converting the dispersed optical signal into electrical data for analysis. Several types of detectors are commonly used in spectroscopy, including Charge-Coupled Devices (CCDs), Photomultiplier Tubes (PMTs), and Avalanche Photodiodes (APDs).

For this thesis, Plasma Vacuum Solutions UVH-1 spectrometer features a CCD-based detector.

Figure 4.1: OES spectrometer featuring a camera sensor module designed for probing across the Ultraviolet (UV), Optical, and Infrared (IR) bands with a minimum resolution of 0.197nm.

4.2.2 Optical Components

The spectrometer's internal optics—including collimating lenses, mirrors, slits, and the diffraction grating—are responsible for focusing and dispersing the incoming light. The design and alignment of these components significantly influence the spectral resolution and light transmission efficiency.

4.2.3 Wavelength Range

The UVH-1 spectrometer covers a broad wavelength span from **294.955 nm to 992.867 nm**, allowing effective measurement from the ultraviolet (UV) to the near-infrared (NIR) region. This wide coverage supports a variety of emission line diagnostics in air and argon plasmas.

4.2.4 Spectral Resolution

Spectral resolution defines the smallest distinguishable wavelength interval, enabling the identification of closely spaced spectral features. The UVH-1 achieves a minimum resolution of **0.197 nm**, sufficient for resolving most emission lines in low-temperature plasma diagnostics.

4.2.5 Dynamic Range

The dynamic range denotes the span of signal intensities measurable without saturation or signal distortion. The UVH-1 model offers a dynamic range of 6000 arbitrary units (Au), allowing reliable detection of both strong and weak emission lines in the same spectrum.

4.2.6 Data Acquisition Rate

The UVH-1 spectrometer supports a high-speed data acquisition rate of up to **365,300 data points per second**. This enables real-time monitoring and analysis of dynamic plasma events, improving the temporal resolution of diagnostics.

4.2.7 Size and Portability

Portability is critical for flexible use in laboratory environments. The UVH-1 spectrometer is compact, lightweight, and powered via a standard USB connection, making it ideal for both stationary and mobile experimental setups.

4.2.8 Connectivity and Interface

The device interfaces seamlessly with computers via USB and is compatible with the dedicated OES software suite for spectral acquisition and analysis. This plug-and-play configuration ensures ease of use, data storage, and real-time visualization during plasma experiments.

4.3 OES Software for Spectroscopic Analysis

The Optical Emission Spectroscopy (OES) software is a critical component of the diagnostic system, enabling comprehensive control, data acquisition, visualization, and analysis of plasma emission spectra. This software bridges the hardware (spectrometer) with the computational interface (computer) to facilitate the interpretation of spectral data, helping extract key plasma parameters such as electron temperature (T_e) and electron density (n_e).

4.3.1 Data Acquisition

The OES software interfaces directly with the spectrometer and associated detector module—typically a CCD-based UV-optical-IR sensor connected via USB. It allows users to define essential acquisition parameters such as integration time, spectral resolution, and wavelength range. Through this interface, emission spectra are captured in real-time as light from the plasma source is directed into the spectrometer.

4.3.2 Spectral Processing

After acquisition, the software offers a suite of processing tools to enhance spectral quality and signal fidelity. These tools include background subtraction, wavelength calibration, normalization, and peak identification.

4.3.3 Visualization Tools

The software provides robust visualization capabilities, allowing emission spectra to be viewed in multiple formats such as line graphs, histograms, or intensity maps. Features like zoom, pan, and cursor tracking facilitate detailed examination of spectral peaks, line widths, and intensities—crucial for quantitative plasma diagnostics (Figure 4.2).

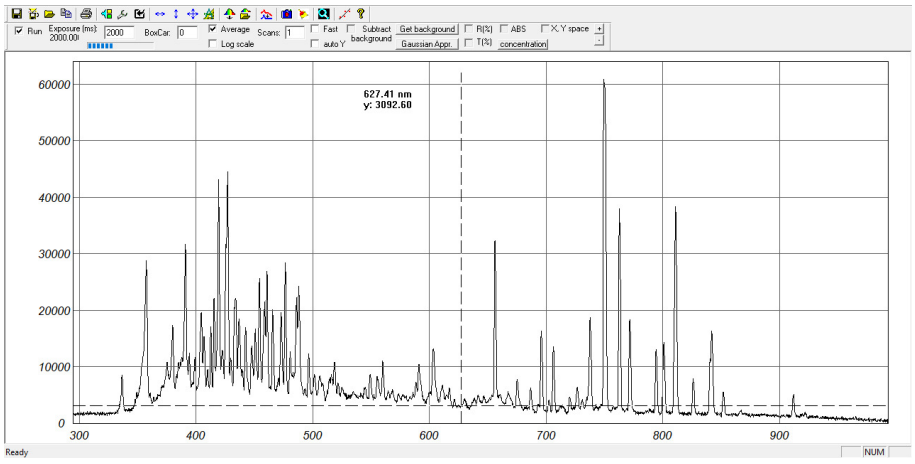

Figure 4.2: Emission Spectrum of Plasma: Intensity (Arbitrary Units) vs. Wavelength (nm).

4.3.4 Quantitative Analysis and Interpretation

Integrated analytical modules in Optical Emission Spectroscopy (OES) software streamline plasma diagnostics by automating elemental identification, concentration estimation, and plasma param-

eter determination. Techniques like Boltzmann plots and Stark broadening analyses are employed to derive electron temperature and density from emission line intensities. Advanced features, including statistical fitting and spectral deconvolution, enhance the accuracy and depth of plasma characterization.

4.3.5 Data Management and Export

Efficient data handling is enabled through features allowing structured storage of spectral files, calibration data, and metadata. The software supports exporting datasets in multiple file formats (e.g., CSV, TXT, or proprietary formats) for further processing or collaborative research.

4.3.6 User Interface and Accessibility

Designed for ease of use, the OES software features a graphical user interface (GUI) that caters to both novice users and experienced researchers. Customizable settings, interactive menus, and integrated help documentation streamline the workflow. Additional support features such as tutorials and remote technical assistance further enhance usability.

In summary, the OES software provides a comprehensive platform for the acquisition, analysis, and interpretation of plasma emission spectra. Its integration with modern spectrometers facilitates real-time, non-invasive diagnostics of low-temperature plasmas and contributes significantly to both fundamental plasma studies and applied research.

4.4 Procedural Framework for Plasma Analysis Using OES

4.4.1 Data Acquisition Procedure

The Optical Emission Spectroscopy (OES) process began with meticulous preparation of the spectrometer. This involved aligning the optical components and verifying the functionality of the detector. The measurement parameters, including the spectral range, integration time, and acquisition mode, were configured using the spectrometer control software. The spectrometer was then precisely focused on the plasma source. The raw spectral data captured by the spectrometer's camera (Figure 4.2) were saved in a suitable file format (e.g., TXT, CSV) for subsequent analysis.

The data were collected across various pressure and applied voltage ranges, from which the electron temperature and electron density were determined for each case. The corresponding Boltz-

mann plot was generated for each condition. Detailed plots of these results can be found in Chapter 6 (Results and Discussion).

In this chapter, to demonstrate the data processing and parameter estimation process, we use the ”argon0.33mbar505.5v.txt” file obtained from the OES spectrometer for the analysis of argon plasma at 0.33 mbar pressure and an applied voltage of 505.5 V.

4.4.2 Data Processing and Visualization

The acquired raw spectral data were imported into OriginLab software [48] for processing and analysis. The software’s visualization tools enabled the graphical representation of the emission spectrum, typically displaying intensity (in arbitrary units) versus wavelength (in nanometers). Additionally, the data were imported into a Python script, which produced the raw spectroscopic data spectrum with a strip of spectral emission lines shown on top. This is illustrated in Figure 4.3, where the initial noisy spectral data is shown.

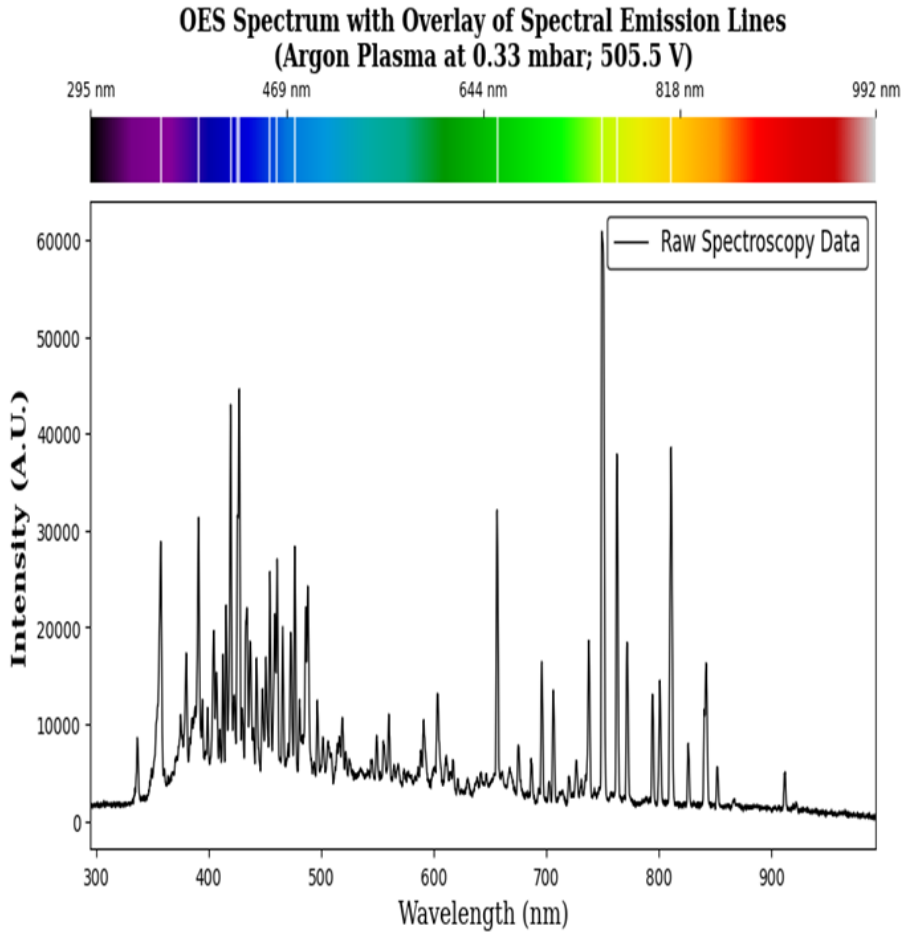

Figure 4.3: Analysis of argon plasma: Intensity (a.u.) vs. Wavelength (nm) for raw spectroscopic data.

4.4.3 Denoising and Spectral Analysis

To enhance the quality of the emission spectrum, denoising techniques were applied. In OriginLab, baseline correction was performed to remove baseline noise. The baseline-noise data were extracted, and the modulus of this data was subtracted from the raw data to obtain a baseline-corrected spectrum. This correction was based on asymmetric least square smoothing.

Following baseline correction, the data were smoothed using the signal processing options in OriginLab, specifically applying the Savitzky-Golay algorithm. These techniques effectively reduced noise and clarified the signal features. Figure 4.4 presents the refined, denoised spectrum.

The same baseline-corrected and smoothed data were also processed in Python to generate the smoothed spectrum, as shown in Figure 4.4.

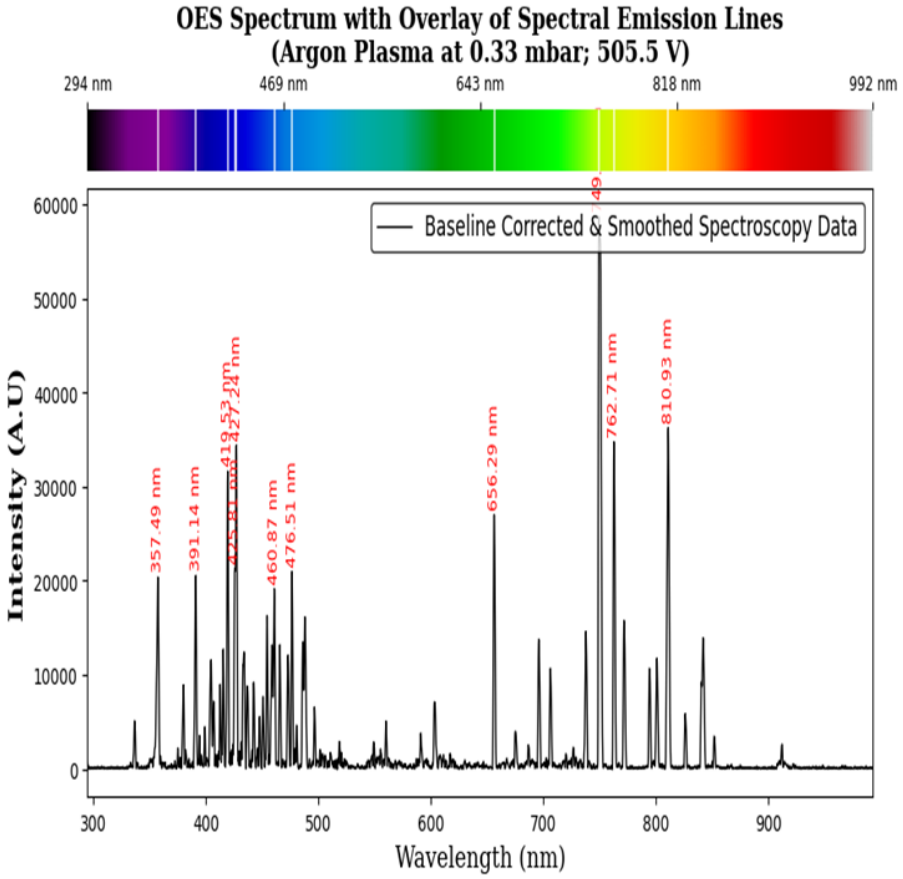

Figure 4.4: Analysis of argon plasma: Intensity (a.u.) vs. Wavelength (nm) after baseline correction and smoothing.

4.4.4 Further Analysis for Boltzmann Plot

The peaks in the spectrum were identified using OriginLab's peak identification feature, which was also employed for baseline correction. These identified peaks were recorded and listed in a Table 4.1. The table contains the peak intensities and their corresponding wavelengths.

Table 4.1: Filtered Spectroscopic Data for Boltzmann Plot [21]

Peak λ [nm]	**Peak Intensity**	**Relative Intensity**	**Ion**	A_{ki} **[s^{-1}]**	E_k **[eV]**	g_k	**log_term**	**Relative Uncertainty** A_{ki}/A_{ki}	**Error log_term**
357.486	20377.79462	6944.167669	Ar II	275000000	23.01454553	8	-5.709934995	0.1	0.100718961
427.239	34400.22901	11722.61094	Ar II	30400000	19.22290215	6	-2.488895347	0.1	0.100426618
454.426	16281.95964	5548.424638	Ar II	47100000	19.86715704	4	-3.237055637	0.1	0.100898063
460.867	19154.04964	6527.150494	Ar II	78900000	21.14307545	8	-4.269559791	0.1	0.100764026
476.509	20976.55123	7148.206741	Ar II	64000000	19.86715704	4	-3.243088244	0.1	0.100697896
488.103	16142.11388	5500.769214	Ar II	39400000	19.76226108	4	-2.978784352	0.1	0.100905650
749.320	58690.38765	20000	Ar I	45000000	13.47988682	1	-0.021553002	0.1	0.100250032
762.712	34759.29368	11844.96987	Ar I	5200000	13.15314387	3	0.542892265	0.2	0.200211111
810.927	36277.72821	12362.40879	Ar I	4900000	13.1717777	5	0.170156565	0.2	0.200202275

In the subsequent analysis, the elemental species were identified by matching the observed spectral peaks with reference databases, such as the NIST database [21]. The wavelengths were selected based on the relative intensities obtained from our data and those reported in the NIST database.

To calculate the electron temperature, the Boltzmann plot method was employed, which involves plotting the logarithmic term against the upper energy levels, as described by Equation 1.4. The uncertainty in the logarithmic term was propagated from the Poisson error in the measured intensity, since intensity corresponds to the number of photon counts as well as from the uncertainty in the transition probability A_{ki}, as given by Equation (1.5).

The Boltzmann plot, presented in Figure 4.5, depicts the determination of electron temperature. The slope of the plot corresponds to the electron temperature in electron volts (eV), with the associated error estimated using the covariance of the slope.

The electron temperature obtained from the Boltzmann method is 1.75 ± 0.04 eV. This estimation of electron temperature (T_e) is based on the relative intensities of emission lines from different ionization stages, as determined from the Boltzmann plot.

4.4.5 Electron Density Calculation via Stark Broadening

For the calculation of electron density, the Full Width at Half Maximum (FWHM) method was applied. The FWHM values were determined by fitting the spectral peaks to a Gaussian distribution using OriginLab software. The Stark broadening parameter ω is essential for accurate electron

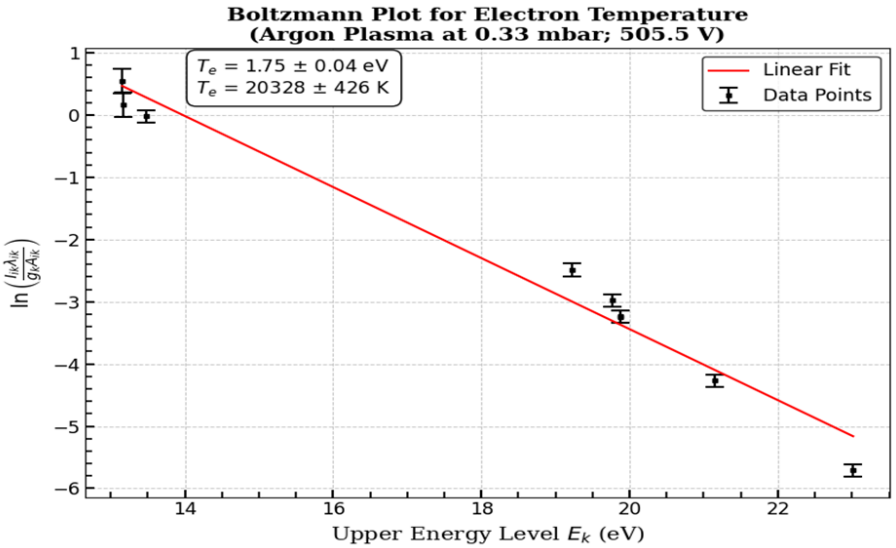

Figure 4.5: Boltzmann plot depicting the electron temperature with corresponding error.

density determination from spectral line broadening. However, this parameter is challenging to obtain with high accuracy and often needs to be sourced from literatures and databases.

For this analysis, we referred a review paper by Konjević et al. (2002) [22], which provides a critically reviewed dataset of Stark widths and shifts for various atomic and ionic species. Using this dataset, the Stark broadening parameter ω for Argon species was estimated, and the electron density was subsequently calculated using Equation 1.6, with its associated uncertainty determined by Equation (1.6.2). The electron density was estimated to be $(1.37712 \pm 0.431864) \times 10^{17}$ cm^{-3}.

The preceding analysis was conducted on an argon plasma at a pressure of 0.33 mbar, with an applied voltage of 505.5 V. Additional plots corresponding to varying pressures and applied voltages were derived using the same analytical methodology. These are presented in Chapter 6, Sections 6.1 (Air Plasma) and 6.2 (Argon Plasma), where they can be examined in detail.

Further plasma parameters—including plasma frequency (ω_p), Debye length (λ_D), and the number of particles within a Debye sphere (N_D)—were calculated using Equation (1.7), Equation (1.8), and Equation (1.9), respectively. The computed values are tabulated in Chapter 6, Section 6.1 and 6.2. Additionally, graphical representations illustrating the variation of these parameters, along with electron temperature and electron density, as functions of pressure and applied voltage, are also provided in the same section.

Chapter 5

Plasma Diagnostics: Langmuir Probe

5.1 LTspice Simulation

The inspiration for the Langmuir probe design is taken from a paper [42], which is discussed in literature review (section 2.3). The circuit as shown in Figure 5.1 depicts the equivalent circuit of the plasma probe system. The circuit is simulated using LTspice software (analog circuit simulator) [49]. The design specifications as shown on the circuit diagram in Figure 5.2a, are derived by solving Poisson's equation for the sheath and electrode. The design specifications are also provided in a Table 5.1 for reference.

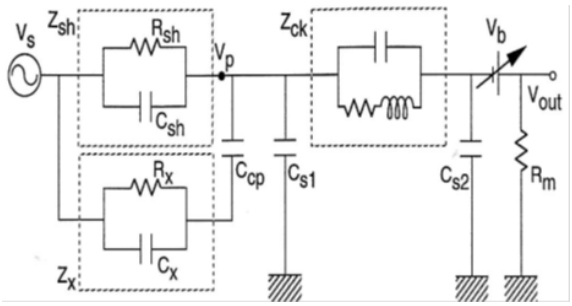

Figure 5.1: Equivalent circuit of the probe plasma system [42].

However, the resulting plot of current through resistance R_m versus potential V_b shows a linear trend without any ion and electron current saturations at extremely high and low voltages, unlike the idealized curve in Figure 1.18. Since the equivalent circuit of a mechanical design can deviate from expected behavior, this suggests that the circuit diagram in Figure 5.1 requires modifications to address the issue of saturation of ion and electron currents.

A diode (1N914) was subsequently placed at various positions in the circuit to simulate and

test for the desired I-V characteristics. A plot resembling the idealized curve was achieved when the diode was connected in series with the bias supply V_b (Figure 5.2a). This plot is valid within the voltage range of -20V to 10V. For higher voltages, the plot is invalid as it fails to saturate due to the physical limitations of components like diodes, resistors, and capacitors, which can influence their behavior at higher voltage levels.

Electronic Component Symbol	**Parameter Description**	**Value and Unit**
V_s	Space or Plasma potential*	— Volts (V)
V_p	Potential at the probe tip (to be measured at node V_p)	To be measured Volts (V)
V_b	Probe DC bias supply voltage	-30 V to $+30$ V Volts (V)
V_0	Output voltage across the resistor R_m (to be measured at node V_{out})	To be measured Volts (V)
R_m	Current and Voltage measuring resistor	1 kΩ Ohm (Ω)
R_{sh}	Sheath impedance Z_{sh}, consists of a resistor in parallel with a capacitor	1.2 kΩ Ohm (Ω)
C_{sh}	Sheath impedance capacitance	3.25 pF Farad (F)
R_x	Auxiliary floating electrode impedance Z_x, consisting of a resistor in parallel with a capacitor	20.014 Ω Ohm (Ω)
C_x	Electrode impedance capacitance	11 pF Farad (F)
C_{cp}	Coupling capacitor for the auxiliary floating electrode	1 nF Farad (F)
R_{ck}	Resistor in choke impedance Z_{ck} circuit	10 kΩ Ohm (Ω)
C_{ck}	Capacitor in choke impedance Z_{ck} circuit	0.04 pF Farad (F)
L_{ck}	Inductor in choke impedance Z_{ck} circuit	1.41 mH Henry (H)
C_{s1}	Stray impedance between chokes and the probe tip	1 pF Farad (F)
C_{s2}	Stray impedance related to the power supply and all connecting cables	0.1 μF Farad (F)
$1N914(diode)$	Small signal fast switching diode (DC blocking voltage)	75 V Volts (V)

Table 5.1: Parameters and Values of the Circuit Components

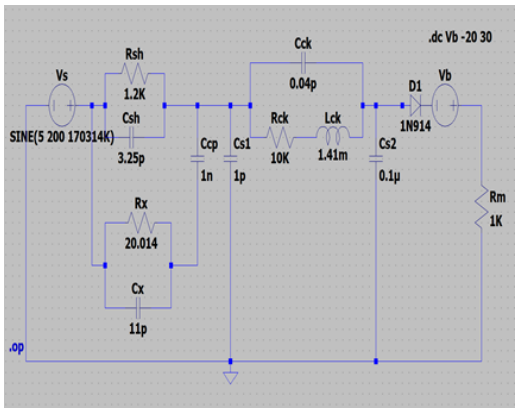

(a) Equivalent circuit diagram for simulation using LTspice.

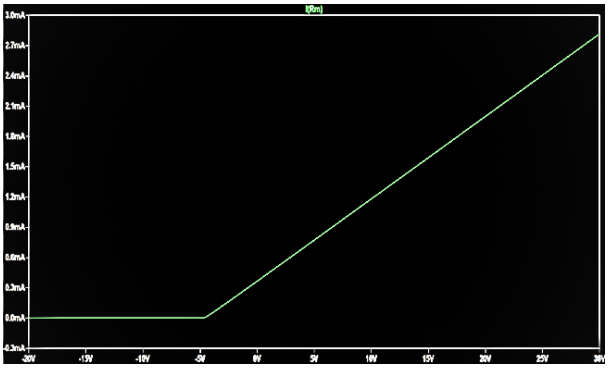

(b) Plot of I-V curve after simulation.

Figure 5.2: LTspice simulation circuit and plot of I-V curve.

5.2 Experimental Setup Of Equivalent Circuit

An experiment was conducted to obtain the I-V curve using an equivalent circuit for probe system and the circuit used for experimental setup is shown in Figure 5.3a. The experimental setup, built on a breadboard (Figure 5.3b), utilized an NPN transistor instead of a diode. The NPN transistor is highly sensitive to high positive voltages. The voltage source (V_s) used in the experiment was ac signal of $2+sin(2*pi*27.12*10^6*t)$ Volts. The values of the components used in the experimental setup are given in the Table 5.1. The results from this experimental setup are discussed in Chapter 5.

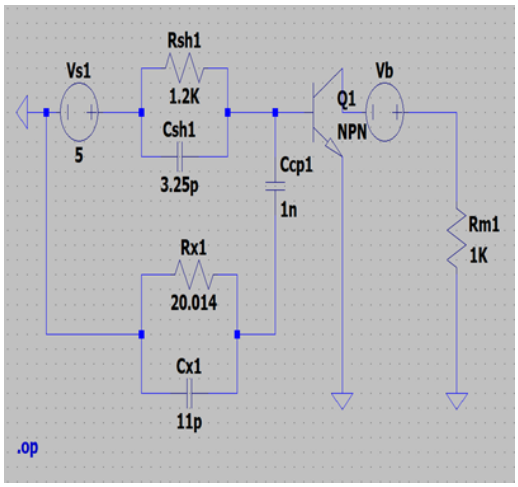

(a) Circuit used for experimental setup.

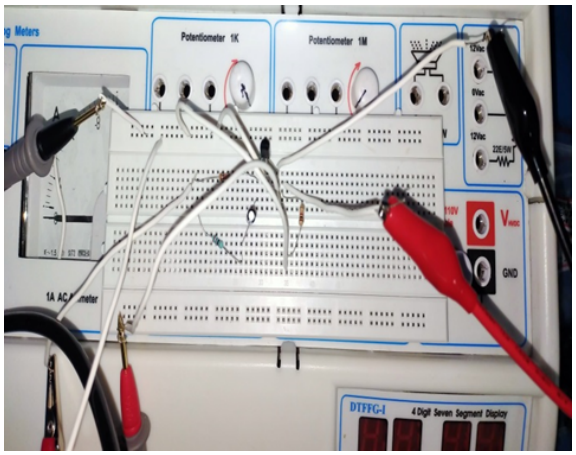

(b) Experimental setup of equivalent circuit on bread board.

Figure 5.3: Circuit used for designing equivalent circuit on breadboard.

5.3 Design and Development Of Langmuir Probe

The probe have to be immersed in a challenging environment, utilizing specialized techniques to shield it from plasma and maintain electrical conductivity, thereby ensuring accurate I-V values. We have to choose a probe tip made from high-temperature material such as graphite needle or tungsten rod with Outer Diameter (OD) of 0.3 mm. The graphite needle or the tungsten rod is then threaded into a very small and thin ceramic tube, providing insulation from the plasma, leaving only a short length of the tip exposed, approximately 2-3 mm in length as shown in Figure 5.4.

The probe tip is centered inside the ceramic tube and without touching the walls of the tube, it is inside the hypodermic needle using an electrically conductive paste which is also used as an electrically conductive adhesive. The end part of the hypodermic needle which is made of some plastic material is then cut off using a cutter so that it can be encased inside the glass tube. The end part of the graphite needle is soldered with a wire (jumper wire) so that it can be connected with the required electrical circuits, to measure the I-V characteristics of the probe. The complete assembly is then encased in a glass tube having an approximate outer diameter of 8 mm. The Figure 5.4 illustrates the 2D design of the Langmuir probe that has been developed, with its image presented in Figure 5.5. The Figure 5.5 illustrates the materials utilized in the fabrication of the Langmuir probe and its appearance post-manufacturing. Additionally, Table 5.2 outlines the design specifications and corresponding values for each component used in the construction of Langmuir probe.

Furthermore, for reference in Appendix A, the images are included to illustrate the brainstorming and refinement process for the design and development of the Langmuir probe.

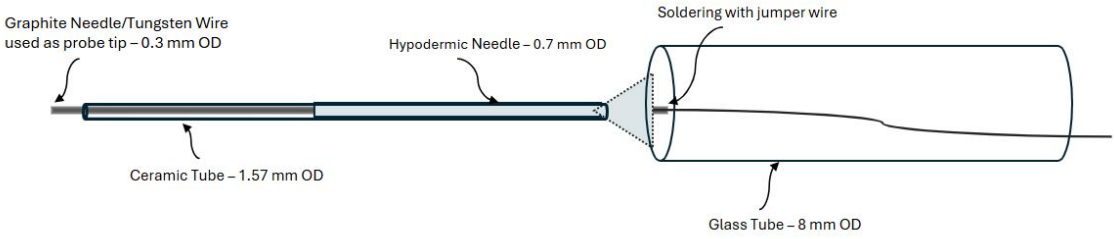

Figure 5.4: Two-dimensional design of Langmuir probe with values of outer diameter (OD).

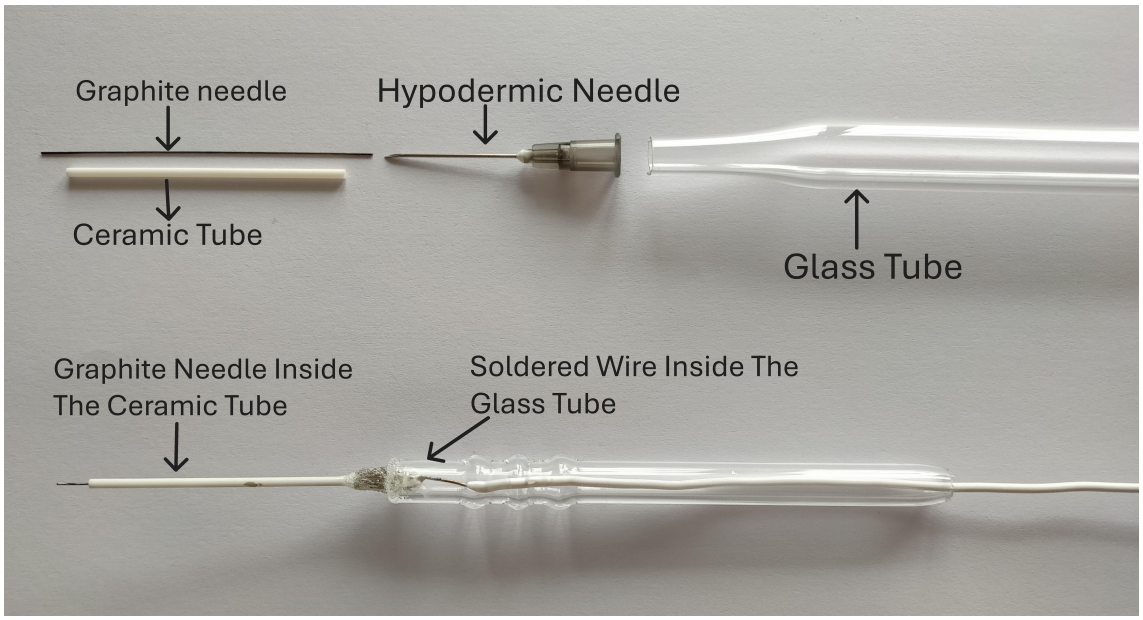

Figure 5.5: Langmuir probe with components used for its manufacturing.

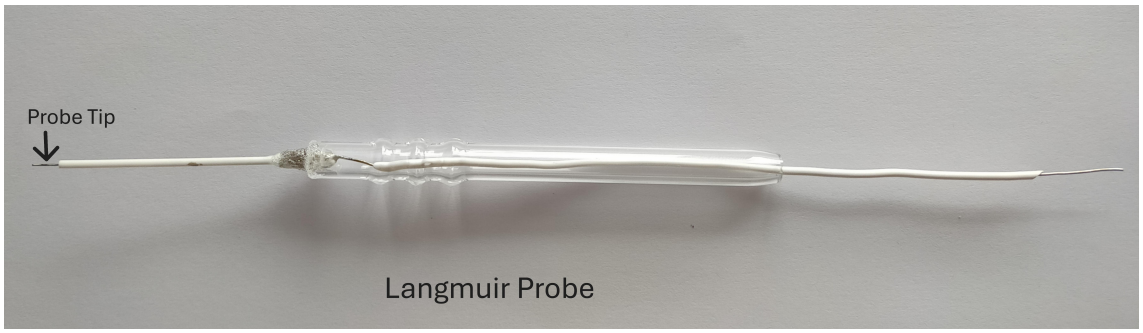

Figure 5.6: Langmuir probe after complete development.

5.4 Design And Fabrication Of Langmuir Probe Compatible With Plasma Chamber

5.4.1 Limitations of the Initial Langmuir Probe Design and the Need for Redesign

The Langmuir probe previously designed and fabricated, as discussed in Section 5.3, was developed primarily for exploratory purposes—to gain familiarity with Langmuir probe concepts and construction techniques. At that stage, the design specifications of the plasma chamber were not yet available. Subsequently, after the plasma chamber was procured and installed in the laboratory, it became evident that the initially fabricated probe was not mechanically and functionally compatible with the new setup.

Table 5.2: Langmuir probe design parameters.

Sl. No.	Probe Parameter	Dimension	Material
1	Probe tip length	3 mm	Graphite
2	Probe tip diameter	0.3 mm	Graphite
3	First tube diameter	1.57 mm	Ceramic
4	First tube length	5.0 cm	Ceramic
5	Hypodermic Needle diameter	0.7 mm	
6	Second tube diameter	8 mm	Glass
7	Second tube length	10 cm	Glass

The primary issue lies in the structural mismatch: the original probe was encased in a glass tube, and although the length constraint could be addressed by employing a longer glass tube (e.g., 35 cm), the glass tube itself could not support or interface with the stainless steel KF40 flange required for secure mounting onto the top tee flange of the chamber for vacuum sealing. Even if a hole matching the outer diameter of the glass tube were drilled into the flange, the sealing would be unreliable and structurally weak.

Additionally, the use of adhesive in the previous design—applied to bond the ceramic tube and hypodermic needle (containing the graphite tip) to the glass enclosure—raises significant concerns. Adhesives are generally unsuitable in plasma environments, as they are prone to vaporization under elevated temperatures. This can lead to contamination of the plasma chamber walls with volatile residues, which are difficult to remove and may render the chamber unsuitable for subsequent plasma experiments.

To address these limitations, a new Langmuir probe was designed and fabricated specifically for compatibility with the current plasma chamber. The revised design eliminates adhesive joints, instead employing mechanical fastening techniques such as micro-drilling and precision fitting with nuts and clamps. Also appropriate, Teflon tape is used to ensure a vacuum-tight seal without introducing contaminants from adhesives. This new approach aligns with best practices for plasma diagnostics and ensures the probe's durability, vacuum integrity, and suitability for long-term experimental use.

The design and fabrication of this new Langmuir probe was carried out at IPS Academy under the supervision of Dr. Nishant Sirse, Associate Professor and Director R&D, IPS Academy, Indore, India.

5.4.2 Fabrication Of Probe

A **Langmuir probe** of length $\approx$ 350 mm, ensuring that it is positioned between the electrodes and visible through the viewports has been designed and fabricated for integration into the plasma chamber for plasma diagnostics. The probe is mounted through a **40 KF port** on the Tee flange of the top adapter flange, ensuring proper vacuum sealing.

The fabrication of the Langmuir probe began with the use of a **300 mm long coaxial cable** as the structural base. The outer plastic insulation was carefully removed. Approximately 10 mm of the aluminum was stripped at one end to expose the underlying aluminum conductor, which serves as the part to be threaded with the tungsten probe. The opposite end was stripped by around 5 mm to facilitate soldering with the BNC connector (Figure 5.7.

Figure 5.7: (a) 300 mm long coaxial cable used as the structural base for the Langmuir probe assembly; (b) Coaxial cable with outer insulation removed and both ends stripped to expose the internal aluminum conductor for electrical connections.

To attach the **tungsten wire** (20 mm in length, 0.1 mm diameter), a thin copper wire was used to wrap and secure it tightly with the exposed 10 mm aluminum conductor (Figure 5.8). Care was taken to thread the tungsten through the copper in a manner that ensured mechanical stability and a firm grip so that the tungsten does not detach, even if the copper wire breaks. Due to the brittleness of tungsten, this stage of the assembly required meticulous handling to avoid breakage.

Subsequently, a **40 KF stainless steel flange** was prepared by drilling a 9.25 mm hole to accommodate the BNC connector. However, drilling through stainless steel proved difficult, and initial attempts were unsuccessful. However, with assistance from the mechanical workshop at the IPS Academy (Indore), the drilling was completed successfully.

Upon initial testing, a standard BNC connector was found to leak at the male–female interface

Figure 5.8: Threading of the tungsten probe tip with the 10 mm exposed aluminium conductor using thin copper wire.

during vacuum trials. To resolve this, a **hermetically sealed BNC connector** was employed, which passed all vacuum integrity tests and was deemed suitable for final integration (Figure 5.9).

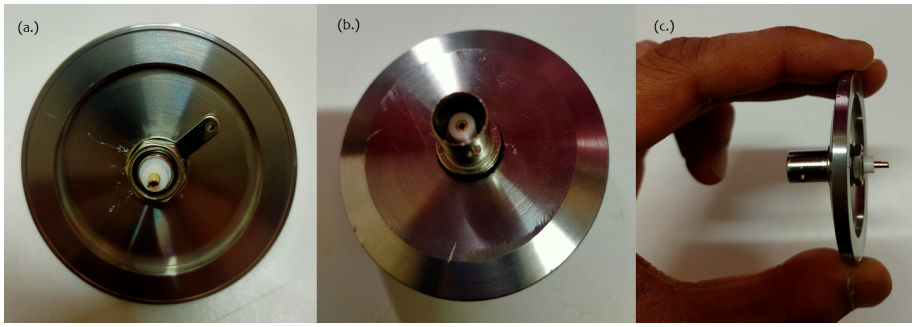

Figure 5.9: BNC connector integrated with the KF40 flange: (a) Inner side of the flange facing the plasma chamber, (b) Outer side of the flange providing probe connectivity, and (c) Lateral view showing the complete flange assembly.

The female end of the BNC connector was then soldered to the exposed 5 mm aluminum conductor of the coaxial cable, ensuring a stable and low-resistance electrical path (Figure 5.10).

For mechanical rigidity and electrical insulation, the probe was encased in a **ceramic tube** approximately 290–300 mm in length. Additionally, a **smaller ceramic tube** ($\approx 30mm - 40mm$ in length) was placed over the exposed tungsten probe wire, leaving less than 10 mm of tungsten as probe tip to be exposed to plasma. The smaller ceramic tube was carefully inserted into the larger one using **Teflon tape** to ensure a snug fit.

Figure 5.11: Fully assembled probe with BNC connector, prior to insertion into the ceramic insulation tube.

Figure 5.10: Soldering of the 5 mm exposed aluminum conductor to the female end of the BNC connector, followed by Teflon taping for mechanical stability and insulation.

Teflon tape was used to ensure a secure fit between the ceramic tube and the BNC connector, preventing unwanted movement and ensuring structural integrity (Figure 5.10).

Finally, additional Teflon tape was used to secure the entire assembly, ensuring the ceramic tube remained stable during vertical insertion into the chamber. Special care was taken to prevent any axial or lateral movement that could compromise the probe's position or performance (Figure 5.12).

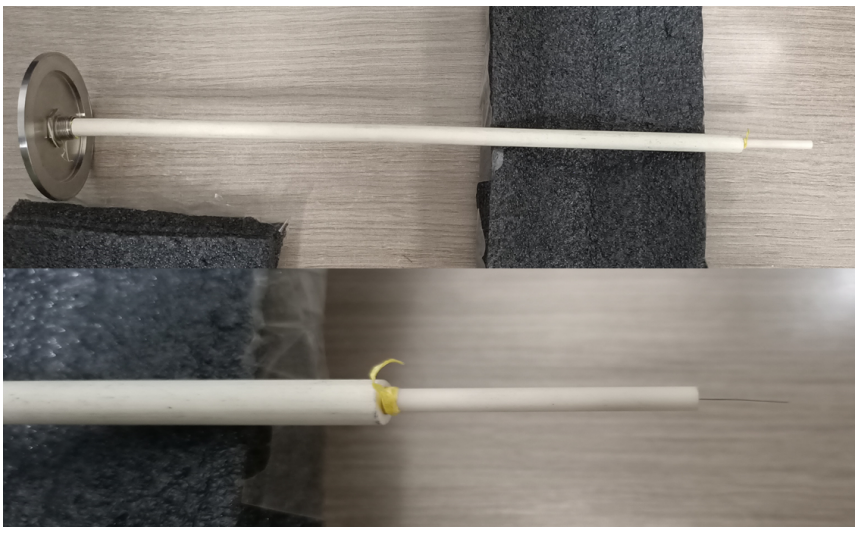

Figure 5.12: Final Langmuir probe assembly ready for installation into the plasma chamber.

With all these steps to develop a probe, a **Langmuir probe**, despite being delicate and sensitive in nature, is now fully assembled and ready for plasma diagnostics.

The Table 5.3 presents the design specifications of the components and materials used in the fabrication of the Langmuir probe, ensuring compatibility with the plasma chamber.

Table 5.3: Design specifications of the newly fabricated Langmuir probe.

Sl. No.	Probe Component	Dimension	Material
1	BNC mounting flange (diameter)	54.86 mm	KF 40 Stainless Steel
2	BNC Connector (diameter)	9.25 mm	-
3	Overall probe length	350 mm	-
4	50 Ω coaxial cable length	300 mm	Aluminium
5	Threading Wire	50 mm	Copper
6	Probe wire	20 mm	Tungsten
7	Probe tip length	8 mm	Tungsten
8	Probe tip diameter	0.1 mm	Tungsten
9	Main Insulating tube length	300 mm	Ceramic
10	Smaller Insulating tube length	40 mm	Ceramic
11	Electrical continuity check	Verified with multimeter	

5.4.3 Electronic Circuit Box

The electronic circuit box plays a crucial role in biasing the Langmuir probe and facilitating the measurement of current and voltage, thereby enabling the generation of I–V characteristic curve used to extract essential plasma parameters.

The circuit box consists of:

- **Three BNC connectors and a resistor** that form the core circuit for I–V measurements.
- **Three cables** used to interface the circuit box with the BNC connector of the Langmuir probe, a low-voltage DC power supply (used to bias the probe), & a digital multimeter (for measuring voltage across the resistor).

Design and Fabrication

The initial design concept for the circuit enclosure involved drilling numerous small-diameter M4 (4 mm) holes in an aluminum sheet to create a fully enclosed box. However, this approach was abandoned due to repeated drill bit breakage, time inefficiency, and difficulties in main- taining alignment.

A more compact and industrial design was also envisioned, inspired by pre-folded enclosures manufactured by electronics companies. These enclosures typically use a single aluminum sheet laser-cut and machine-folded into a box with four or more walls. However, implementing this approach manually proved unfeasible because the available aluminum sheet was difficult to fold cleanly beyond one or two bends without the help of precision equipment. Also, the manual folding

using hammers or vices resulted in imperfect angles, especially when more than two folds were attempted.

To address these challenges, a more practical design was conceived. Two aluminum sheets were selected and bent into shape (Figure 5.13):

- One with dimensions approximately **2.7 cm × 10.1 cm**,
- Another with dimensions approximately **4.7 cm × 8.1 cm**.

Figure 5.13: Raw materials for constructing the electronic circuit box: two aluminum sheets (pre-cut to required dimensions) and two panel-mount BNC connectors.

These sheets were bent into ”U” shapes manually and nested together to form a rectangular box with final external dimensions of approximately **2.5 cm × 4.5 cm × 2.5 cm**. A $0.2cm$ tolerance was incorporated to account for material thickness and bending clearances.

To fasten the sheets together, a single M3 hole was drilled and grooved to accommodate an M4 screw, allowing secure external fastening without internal access or the use of nuts.

Three **10 mm diameter holes** were drilled on one of the box walls to accommodate BNC connectors. Internally, the center pins of the BNCs were soldered using thin wires and connected with a **560 Ω resistor**, which acts as the current-sensing element (Figure 5.14).

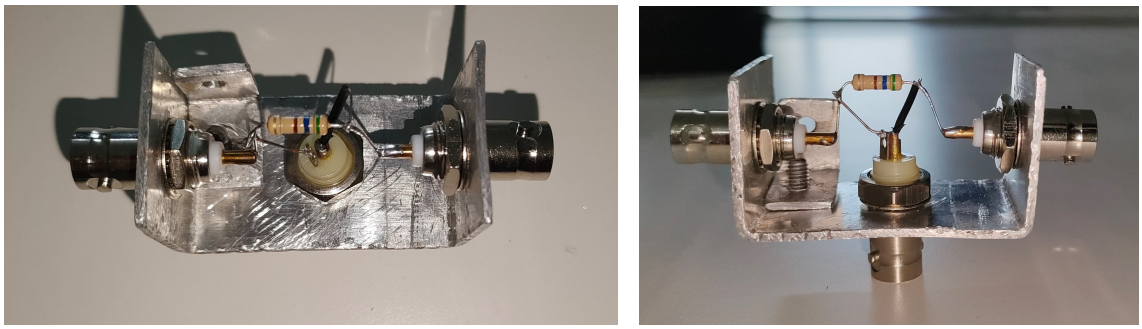

(a) **(b)**

Figure 5.14: (a) Top view and (b) side view showing the internal layout of the electronic circuit box, including BNC connector terminals and soldered resistor connections.

Once connected and verified, the two U-shaped halves were tightly fitted to form a durable electronic circuit box, ready for Langmuir probe measurements (Figure 5.15).

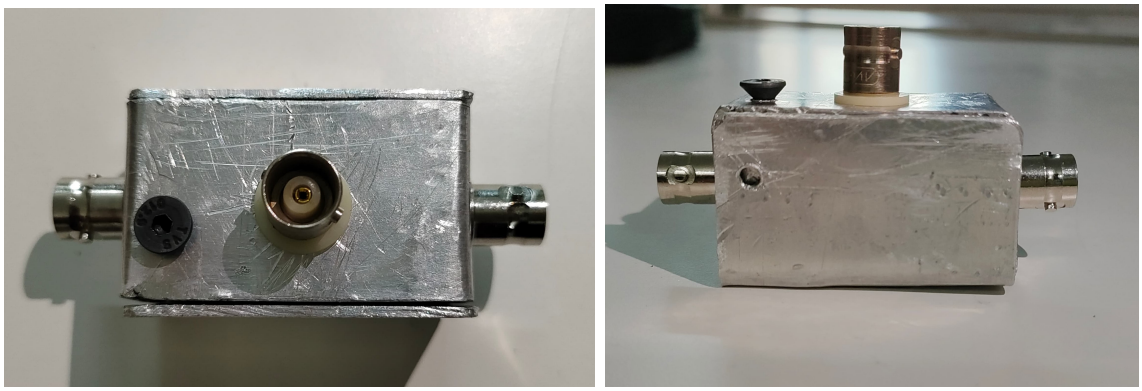

(a) **(b)**

Figure 5.15: (a) Top view and (b) side view of the completed electronic circuit box with tightly interlocked aluminum sheets and mounted BNC connectors.

Chapter 6

Results And Discussion

6.1 Data Analysis of OES Spectroscopic Data

The spectroscopic data obtained from the OES system were processed in OriginLab for initial visualization and baseline correction. These results were then fed into a Python script to produce raw spectra, baseline-corrected and smoothed spectra, and Boltzmann plots for electron temperature estimation. The data were collected under various pressure and voltage conditions using air and argon as the working gases. The complete methodology is detailed in Section 4.4.

6.1.1 For Air Plasma

The Figure 6.1 illustrates the Optical Emission Spectroscopy (OES) results, showing the raw emission spectra, the baseline-corrected and smoothed spectra, and the Boltzmann plot generated from selected peak wavelengths and intensities corresponding to various pressure and voltage conditions.

The plasma parameters extracted from Optical Emission Spectroscopy (OES) and Stark broadening analysis are summarized in Table 6.1. The table presents the calculated electron temperature (T_e), electron density (n_e), and key plasma parameters including plasma frequency (ω_p), Debye length (λ_D), and the number of particles within the Debye sphere (N_D), along with their associated uncertainties, for different pressures and applied voltages.

Figure 6.2 illustrates the variation of electron temperature (T_e) and electron density (n_e) with respect to pressure and applied voltage. The observed trends indicate that with increasing pressure, both the electron temperature and the electron density decrease. Conversely, an increase in the

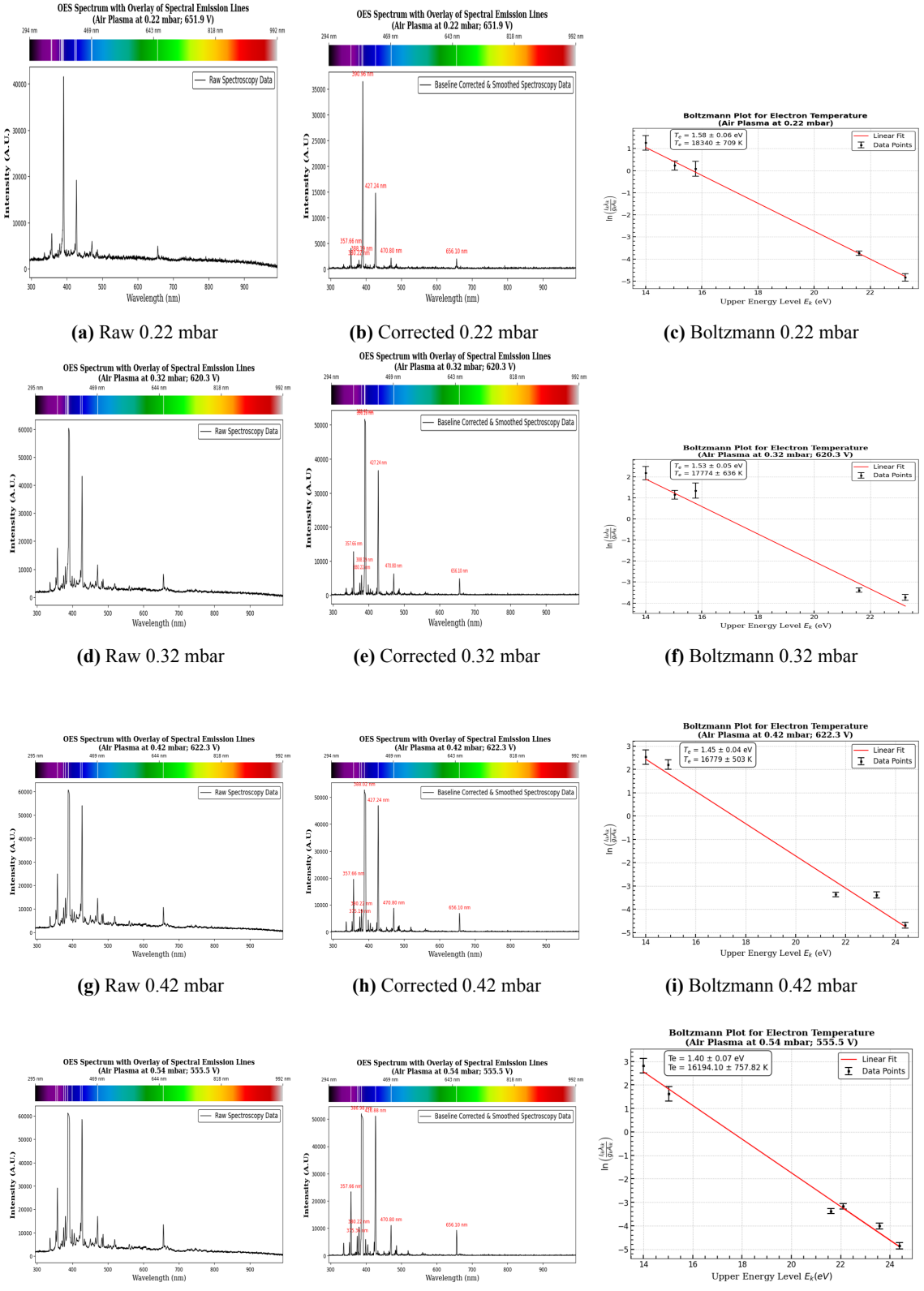

(a) Raw 0.22 mbar **(b)** Corrected 0.22 mbar **(c)** Boltzmann 0.22 mbar

(d) Raw 0.32 mbar **(e)** Corrected 0.32 mbar **(f)** Boltzmann 0.32 mbar

(g) Raw 0.42 mbar **(h)** Corrected 0.42 mbar **(i)** Boltzmann 0.42 mbar

(j) Raw 0.54 mbar **(k)** Corrected 0.54 mbar **(l)** Boltzmann 0.54 mbar

Figure 6.1: Collection of 12 plots for air plasma showing raw OES data, baseline-corrected and smoothed spectra, and corresponding Boltzmann plots at various pressures.

Table 6.1: Final plasma parameters extracted from OES and Stark broadening analysis for air plasma.

Pressure (mbar)	**Voltage** (V)	T_e (eV)	ΔT_e (eV)	**FWHM** (nm)	ω (nm)	$\Delta\omega/\omega$	$\mathbf{n}_e$ (cm^{-3})	$\Delta\mathbf{n}_e$ (cm^{-3})	ω_p (rad/s)	$\Delta\omega_p$ (rad/s)	λ_D (cm)	$\Delta\lambda_D$ (cm)	N_D	ΔN_D
0.22	651.90	1.58	0.03	1.86	0.02	0.30	6.00×10^{17}	9.55×10^{16}	4.37×10^{13}	3.48×10^{12}	1.21×10^{-6}	1.07×10^{-7}	4.41	1.88
0.42	622.30	1.45	0.02	4.12	0.04	0.23	5.82×10^{17}	6.84×10^{16}	4.31×10^{13}	2.53×10^{12}	1.17×10^{-6}	7.70×10^{-8}	3.94	1.24
0.54	555.30	1.40	0.04	1.42	0.04	0.23	2.00×10^{17}	2.69×10^{16}	2.53×10^{13}	1.70×10^{12}	1.96×10^{-6}	1.57×10^{-7}	6.37	2.38

applied voltage leads to an increase in both the electron temperature and the electron density.

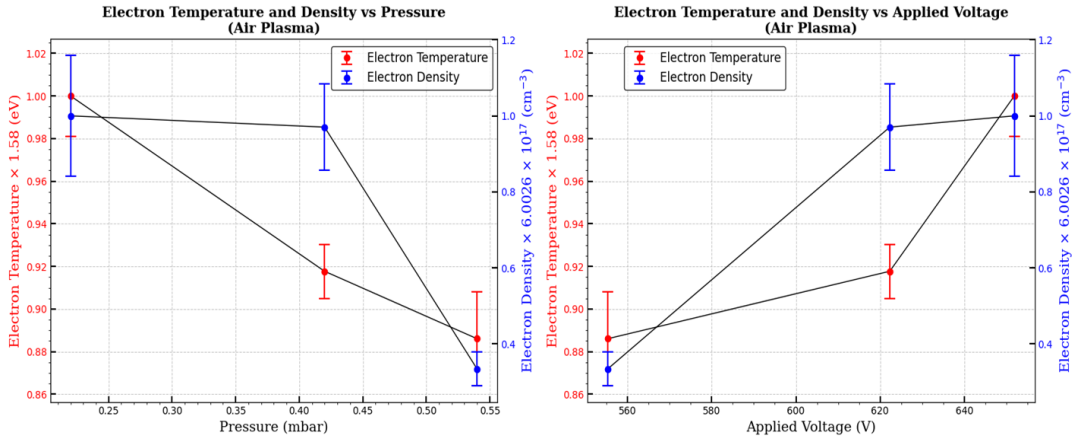

Figure 6.2: Variation of T_e and n_e as a function of (a) pressure (mbar) and (b) applied voltage (V).

Figure 6.3 shows the behavior of key plasma parameters, namely plasma frequency (ω_p), Debye length (λ_D), and the number of particles within the Debye sphere (N_D), with changing pressure and applied voltage. These trends provide further insight into how plasma characteristics evolve under different discharge conditions.

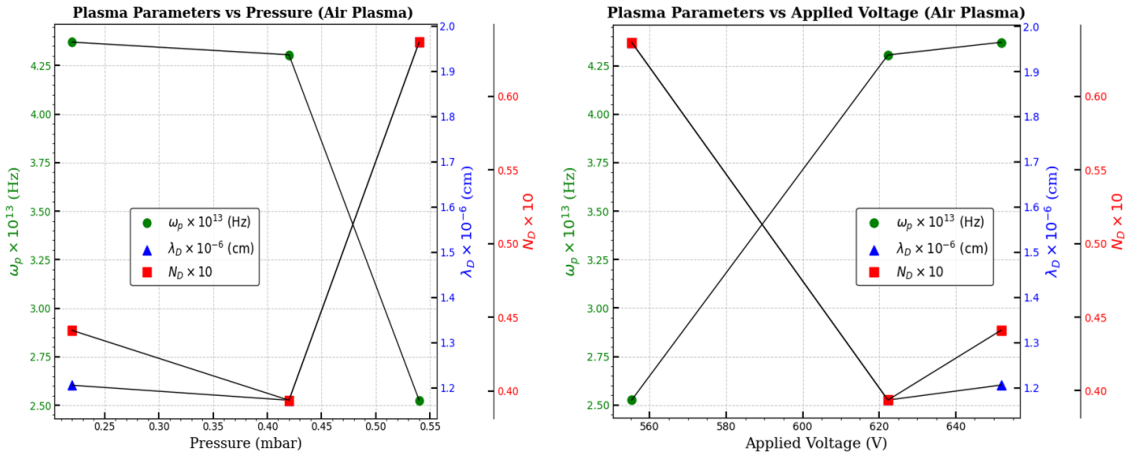

(a) **(b)**

Figure 6.3: Variation of plasma parameters: ω_p,λ_D, and N_D as a function of (a) pressure (mbar) and (b) applied voltage (V).

6.1.2 For Argon Plasma

The Optical Emission Spectroscopy (OES) analysis for argon plasma is presented in Figure 6.4, showing the raw emission spectra, baseline-corrected and smoothed spectra, and the corresponding Boltzmann plots at different pressures and applied voltages.

The plasma parameters extracted from OES and Stark broadening analysis, including electron temperature (T_e), electron density (n_e), plasma frequency (ω_p), Debye length (λ_D), and the number of particles inside the Debye sphere (N_D) with their uncertainties, are summarized in Table 6.2.

Table 6.2: Final plasma parameters extracted from OES and Stark broadening analysis for Argon plasma.

Pressure (mbar)	**Voltage** (V)	T_e (eV)	ΔT_e (eV)	**FWHM** (nm)	ω (nm)	$\Delta\omega/\omega$	$\mathbf{n}_e$ (cm^{-3})	$\Delta\mathbf{n}_e$ (cm^{-3})	ω_p (rad/s)	$\Delta\omega_p$ (rad/s)	λ_D (cm)	$\Delta\lambda_D$ (cm)	N_D	ΔN_D
0.23	574.70	1.82	0.02	2.40	0.03	0.15	3.49×10^{17}	2.99×10^{16}	3.33×10^{13}	1.43×10^{12}	1.70×10^{-6}	8.19×10^{-8}	7.15	1.65
0.33	505.50	1.75	0.02	2.16	0.08	0.30	1.38×10^{17}	2.16×10^{16}	2.09×10^{13}	1.64×10^{12}	2.65×10^{-6}	2.23×10^{-7}	10.74	4.39
0.42	440.90	1.65	0.02	2.13	0.08	0.30	1.33×10^{17}	2.08×10^{16}	2.06×10^{13}	1.61×10^{12}	2.62×10^{-6}	2.18×10^{-7}	10.01	4.06
0.52	328.30	1.58	0.02	2.21	0.11	0.30	1.05×10^{17}	1.64×10^{16}	1.83×10^{13}	1.43×10^{12}	2.89×10^{-6}	2.40×10^{-7}	10.56	4.28

The variation of T_e and n_e with pressure and applied voltage, as well as the behavior of ω_p, λ_D, and N_D, is shown in Figure 6.5 and Figure 6.6, respectively, highlighting the dependence of plasma characteristics on discharge conditions.

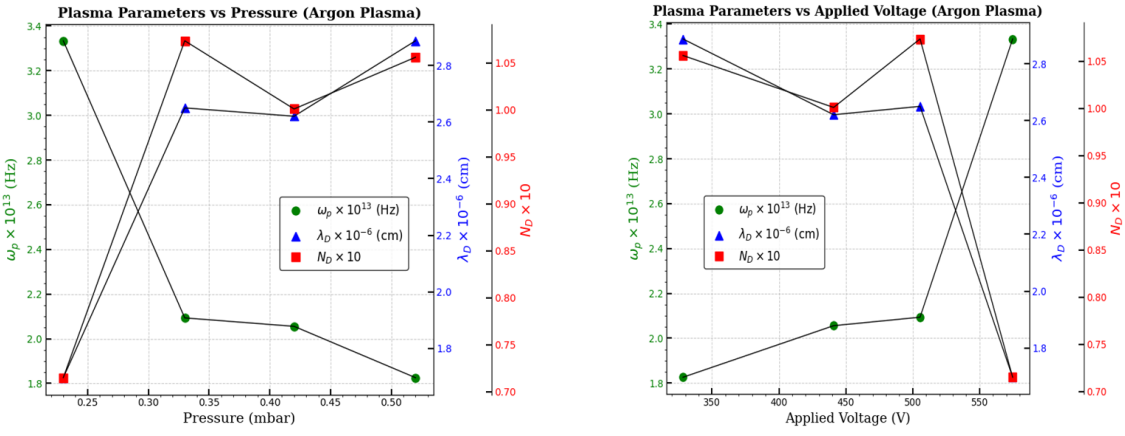

(a) **(b)**

Figure 6.6: Variation of plasma parameters: ω_p,λ_D, and N_D as a function of (a) pressure (mbar) and (b) applied voltage (V) for Argon plasma.

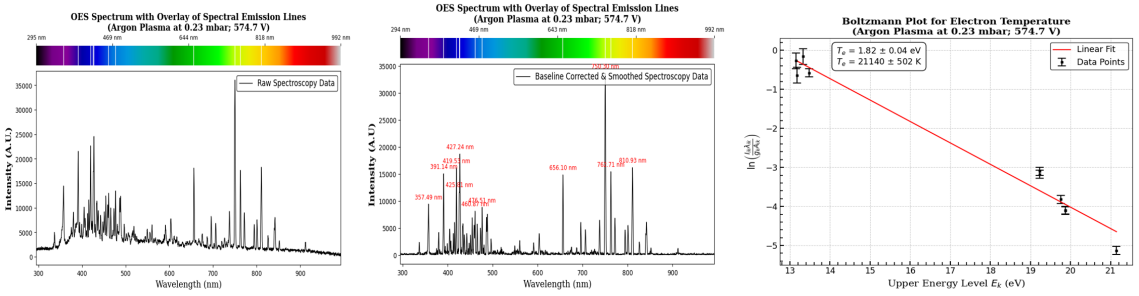

(a) Raw 0.23 mbar **(b)** Corrected 0.23 mbar **(c)** Boltzmann 0.23 mbar

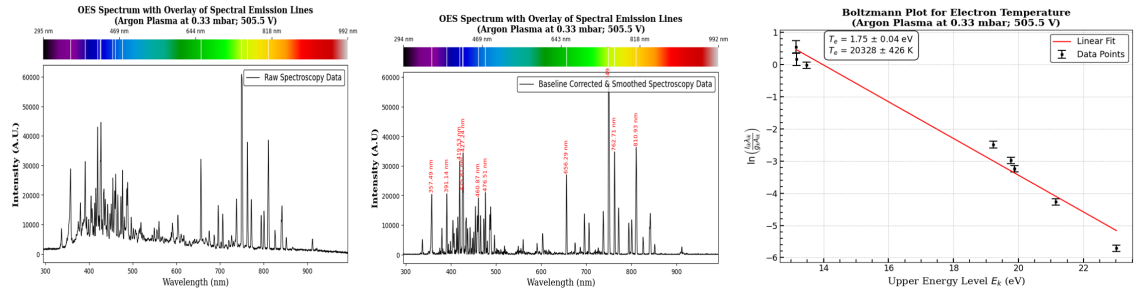

(d) Raw 0.33 mbar **(e)** Corrected 0.33 mbar **(f)** Boltzmann 0.33 mbar

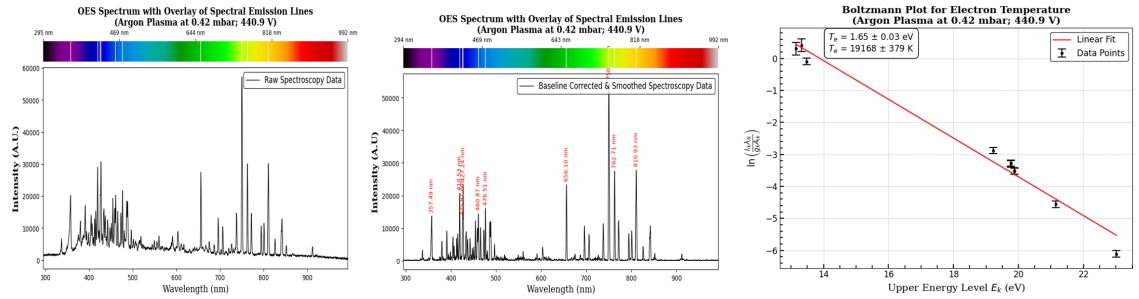

(g) Raw 0.42 mbar **(h)** Corrected 0.42 mbar **(i)** Boltzmann 0.42 mbar

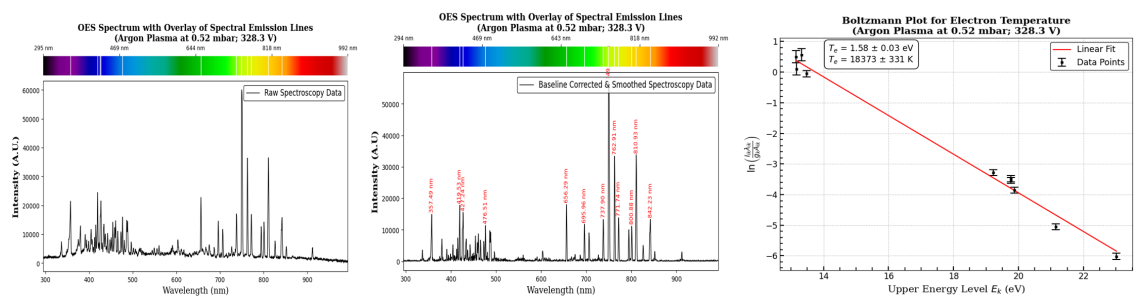

(j) Raw 0.52 mbar **(k)** Corrected 0.52 mbar **(l)** Boltzmann 0.52 mbar

Figure 6.4: Collection of 12 plots for argon plasma showing raw OES data, baseline-corrected and smoothed spectra, and corresponding Boltzmann plots at various pressures.

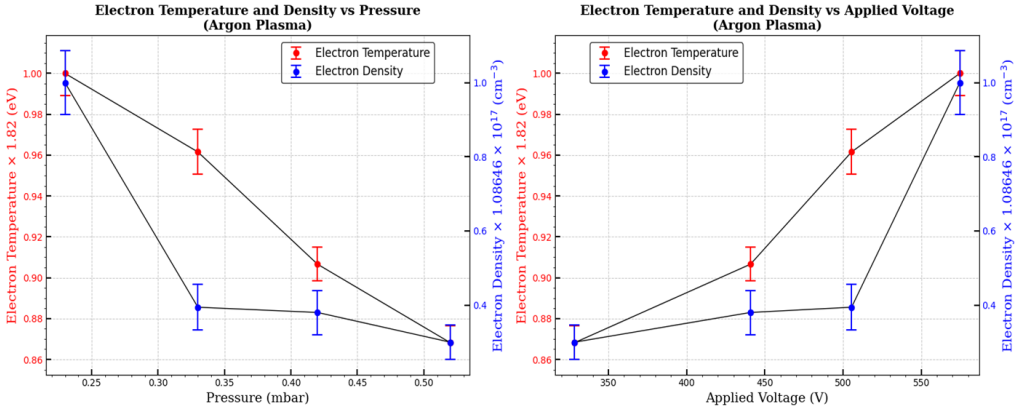

Figure 6.5: Variation of T_e and n_e as a function of (a) pressure (mbar) and (b) applied voltage (V) for Argon plasma .

6.2 Langmuir Probe: Experimental Setup Of Equivalent Circuit

The experimental setup produces reliable results for low voltages, typically in the range of -10V to +3V. Beyond this range, the NPN transistor's sensitivity to high voltage leads to breakdown, potentially damaging the circuit components.

Figure 6.7a illustrates the I-V characteristic curve for a plasma system that generally exhibits poor electron saturation. However, ion saturation is observed at low voltages. Figure 6.7b presents the plot of $\frac{dI}{dV}$ versus voltage (V). The point at which $I_e'(V)$ reaches its maximum, or equivalently where $I_e''(V) = 0$, indicates the space potential V_s, even if the electron current I_e does not exhibit saturation at higher voltages. The semilog plot of the I-V curve, shown in Figure 6.8, indicates that the slope of this plot is precisely $\frac{1}{T_{eV}}$ providing an accurate measure of electron temperature. Here, $T_{eV} = \frac{k_B T_e}{e}$, representing the electron temperature in electron volts (eV). From Figure 6.7b, the minimum value of $\frac{dI}{dV}$ occurs at approximately 1.88 V, indicating that the space potential (V_s) is 1.88 Volts. The provided space or source voltage is 2 V, resulting in:

$$V_s = 1.88\,\text{V} \quad \text{with a 6\% error.}$$

From Figure 6.8, the slope is 1.1088, leading to the following relation:

$$1.11 = \frac{e}{k_B T_e}$$

Solving for T_e, the electron temperature is calculated as:

$$T_e = 10445.23\,\mathrm{K}$$

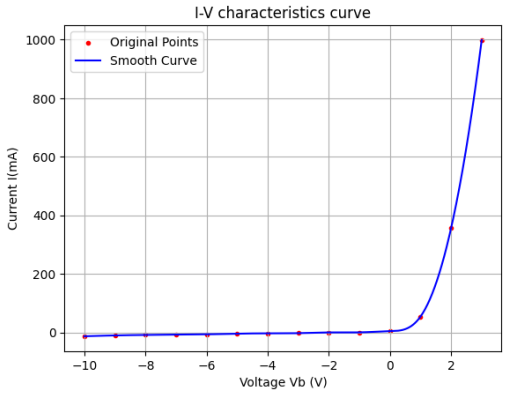

(a) I-V Characteristic Curve using euivalent circuit.

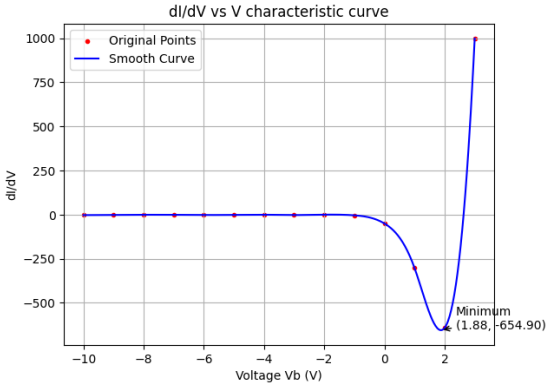

(b) dI/dV vs V characteristic curve.

Figure 6.7

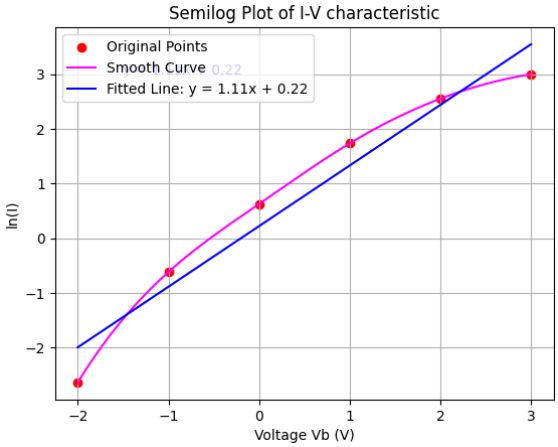

Figure 6.8: Semilog Plot Of I-V curve.

6.3 Manufactured Langmuir Probe

The tungsten tip of the probe may be eroded by sputtering while collecting ion current, thus changing the area of collection of charge particles. This can be minimized using a graphite needle as probe tip, even though it is hard to solder a graphite needle with a jumper wire made of some metal material.

The Langmuir probe manufactured has an electrical continuity from probe tip to the end of the wire which makes it useful for conducting plasma probe experiments with a plasma chamber.

However, due to the dimensional constraints and other limitations discussed in Section 5.4.1,

the existing Langmuir probe was found to be incompatible with the plasma chamber used in our laboratory. Consequently, it was necessary to design and fabricate a new Langmuir probe tailored to our specific plasma chamber and the experimental setup.

6.4 Langmuir Probe Fabricated For Plasma Chamber

The Langmuir probe and its associated electronic circuit box have been successfully fabricated to be fully compatible and suitable for operation within our plasma chamber. A detailed account of their design and fabrication process is provided in Section 5.4.2. The fabricated probe has successfully passed vacuum integrity tests at various stages of development, confirming both its structural robustness and electrical continuity. Furthermore, the probe demonstrated excellent mechanical stability, showing no signs of deformation or failure—even when positioned vertically between the electrodes.

The electronic circuit box also exhibits strong mechanical integrity, securely housing the components and maintaining the structural layout under operational conditions. The circuit itself represents a precise and carefully assembled piece of micro-engineering, combining manual craftsmanship with high standards of electronic design. This integrated setup ensures accurate and reliable measurements during plasma diagnostics.

Chapter 7

Conclusions And Scope For Future Work

The plasma chamber assembly was constructed and understood at a detailed component level, enabling a modular approach to experimental diagnostics. The system was successfully employed for plasma generation experiments using a high-voltage DC power supply capable of delivering up to 660 V. Stable and repeatable plasma discharges were achieved under varying experimental conditions, forming the basis for further diagnostics.

Optical Emission Spectroscopy (OES) was employed to analyze both air and argon plasmas under varying pressure and voltage conditions. From the acquired spectral data, key plasma parameters—such as electron temperature (T_e) and electron density (n_e)—were accurately extracted using techniques including the Boltzmann plot method and Stark broadening analysis.

The variation of T_e, n_e, and other fundamental plasma parameters with respect to discharge conditions (pressure and applied voltage) was systematically studied. It was observed that an increase in pressure leads to a decrease in both electron temperature (T_e) and electron density (n_e), while an increase in applied voltage results in an increase of these parameters.

This behavior can be attributed to the underlying plasma physics, i.e., at lower pressures, electrons undergo fewer collisions, enabling them to gain more energy from the electric field, thus resulting in a higher electron temperature. Conversely, at higher pressures, frequent electron-neutral collisions increase energy loss, leading to a reduction in electron temperature. Similarly, higher applied voltages provide greater energy input to the electrons, raising the electron temperature and density, particularly in low-pressure discharges. However, at very high voltages, effects such as secondary electron emission, ionization, and plasma instabilities may introduce non-linearities into these trends.

The trends observed for plasma frequency (ω_p), Debye length (λ_D), and the number of particles

inside the Debye sphere (N_D) also follow similar dependencies on pressure and voltage. Overall, the experimental results exhibit strong agreement with trends reported in the existing literature, thereby validating the accuracy, consistency, and reliability of the experimental methodology employed in this study.

In parallel, LTspice simulations and practical experiments on an equivalent circuit model of the probe assembly provided useful approximations of plasma behavior, offering further validation of diagnostic approaches. The insights gained from these simulations have been instrumental in bridging theoretical models with experimental results.

The initially available Langmuir probe in our laboratory was found to have dimensional and compatibility limitations when interfaced with the custom-designed plasma chamber. This necessitated the development and fabrication of a new Langmuir probe tailored for our experimental setup. The newly fabricated probe passed mechanical stability, vacuum integrity, and electrical continuity tests, confirming its readiness for future plasma diagnostics. Due to the unavailability of a low-voltage DC power supply required for biasing the probe tip and a high-voltage power supply essential for plasma generation, the newly fabricated Langmuir probe could not be employed to determine plasma parameters through the analysis of the I–V characteristics curve.

Future Scope of Work

The experimental setup developed in this study provides a solid foundation for further investigations into plasma diagnostics and characterization.

- The **Langmuir probe** was successfully fabricated, but the determination of plasma parameters via the analysis of its I–V characteristics could not be conducted due to the unavailability of a low-voltage DC power supply for probe biasing and a high-voltage power source for sustained plasma generation. Future work will focus on completing this diagnostic setup to enable direct measurement of electron temperature, electron density, and plasma potential using the Langmuir probe technique.

- Additionally, the current experimental system can be extended to study discharges in reactive gases or complex gas mixtures relevant to applications in industrial and space plasmas.

Chapter A

APPENDIX-A

Brainstorming And Refinement For Manufactured Langmuir Probe

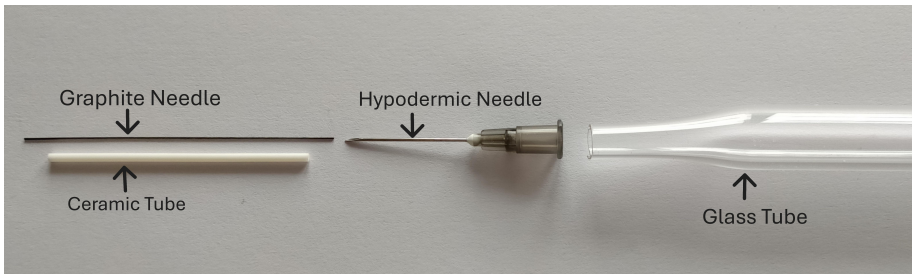

Figure A.1: The materials and components used for the construction of a Langmuir probe.

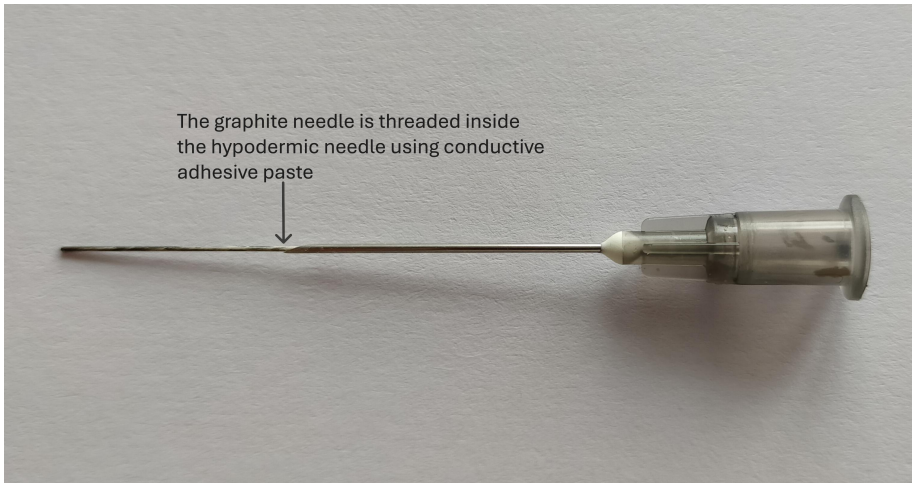

Figure A.2: The graphite needle is inserted into the hypodermic needle, ensuring that a portion of it extends beyond both the top and the bottom ends of the probe.

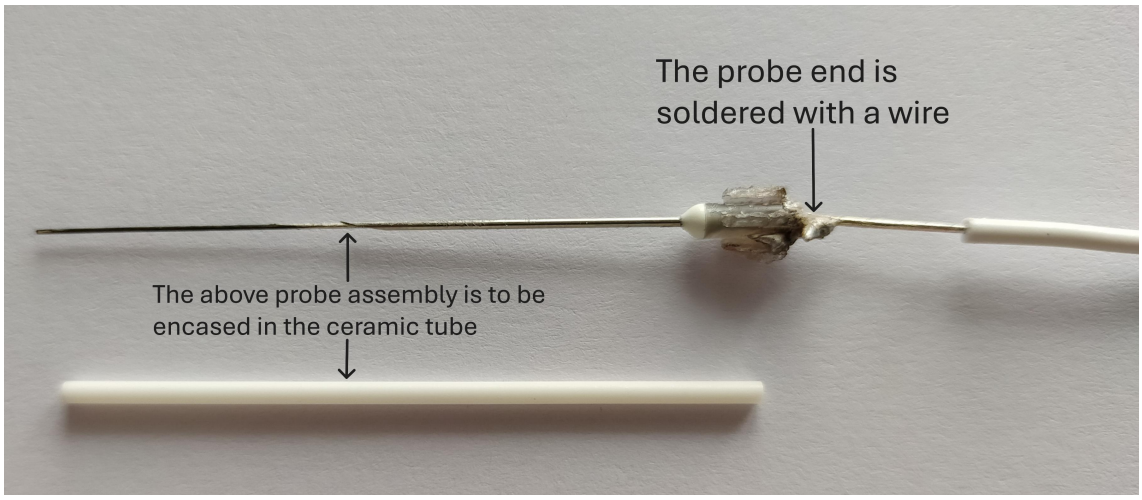

Figure A.3: The plastic end of the hypodermic needle is removed, facilitating soldering the wire to the probe end and allowing the assembly to be conveniently encased within a glass tube.

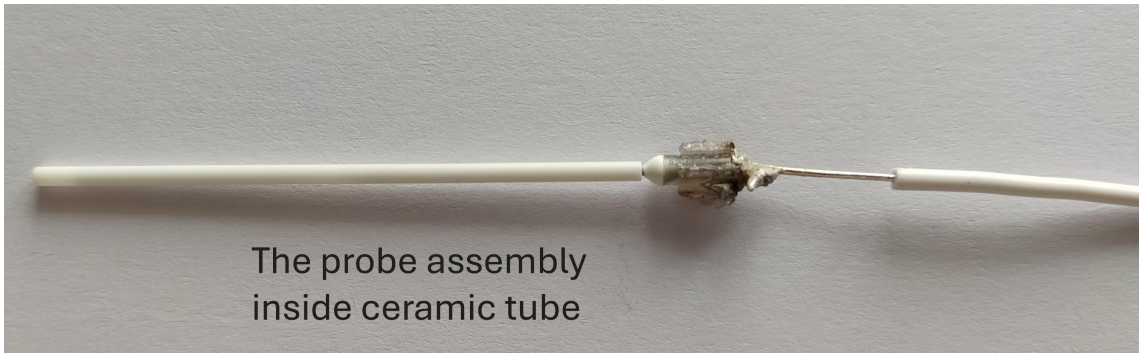

Figure A.4: The probe assembly inside the ceramic tube before encasing it inside a glass tube.

Chapter B

APPENDIX-B

B.1 Paschen's Equation

When a gas is subjected to a sufficiently strong electric field (E) between two electrodes, it can lead to an electric discharge—a self-sustaining current resulting from ionization processes. The discharge becomes self-sustaining, or reaches electrical breakdown, when each charge carrier can generate at least one additional carrier before being neutralized.

The current is driven by electrons and ions generated via ionization of neutral gas atoms, primarily driven by high-energy electrons accelerated by the field. Electrons, due to their lower mass, gain higher kinetic energy and are the primary contributors to further ionization. The electrons are directed toward the anode, and the heavier positive ions toward the cathode.

Two key mechanisms govern breakdown:

- **Ionization**: High-energy electrons ionize neutral gas molecules, producing additional charge carriers.
- **Secondary Electron Emission**: Positive ions recombining at the cathode can release electrons via the Auger effect if the released energy exceeds the cathode's work function.

A transition into the plasma state occurs when these processes become self-sustaining.

Paschen's Law defines the relationship between the breakdown voltage (V_b) which is associated with the breakdown electric field (E_b), and the product of the gas pressure (p) & the electrode separation (d). The law is expressed as:

$$V_b = f(p \cdot d)$$

where $f(p \cdot d)$ is a function dependent on the nature of the gas. This relationship is fundamental in understanding electrical breakdown in gases and is critical in designing electrical insulation systems.

The exact relation for breakdown voltage is given by:

$$V_b = \frac{B(pd)}{C + \ln(pd)}$$

$$\frac{E_b}{p} = \frac{B}{C + \ln(pd)}$$

where

$$C = \ln\left(\frac{A}{\ln\left(\frac{1}{\gamma} + 1\right)}\right)$$

The potential V_b & $\frac{E_b}{p}$ depend on the product of pd. The calculation of V_b, with experimentally determined constants A and B (Table: B.1), gives satisfactory agreement with the experiment.

Gas	**A** $(\text{mbar} \cdot \text{cm})^{-1}$	**B** $(\text{V}/(\text{mbar} \cdot \text{cm}))$
Air	20	487
CO_2	27	621
H_2	7	173
N_2	13	413
He	4	45
Ar	16	240

Table B.1: The values of constants A and B for different types of gases.

Key points:

i. At very low pressures, the breakdown voltage increases due to insufficient ionization.

ii. At very high pressures, frequent collisions suppress free electron mobility, increasing the breakdown voltage.

iii. Paschen's curve demonstrates a minimum breakdown voltage for a specific $p \cdot d$ value.

B.2 Experimental Study of Paschen's Curve in Gas Discharges

The Paschen curves shown here were obtained by fitting experimental data using the Paschen equation as the model. These measurements were performed at a fixed electrode gap of 2.5 cm

while varying the gas pressure. At each pressure, the voltage corresponding to the visible onset of plasma glow was recorded. It is important to note that this glow discharge voltage is slightly higher than the actual breakdown voltage, introducing a systematic offset in the extracted Paschen constants A and B. This deviation has been accounted for in the curve-fitting routine to reduce the associated error.

Table B.2 and Table B.3 present the experimental data for air and argon plasmas, respectively. These datasets reflect the minimum voltages at which a visible glow is observed, serving as practical indicators of breakdown onset in the absence of precise diagnostics.

Table B.2: Experimental Data for Paschen's Curve Analysis of Air Plasma

Pressure (mbar)	Glow Discharge Voltage (V)
0.20	525.3
0.25	429.5
0.30	405.4
0.40	396.3
0.50	397.9
0.60	410.8
0.70	426.0
0.80	439.0
0.90	444.3

Table B.3: Experimental Data for Paschen's Curve Analysis of Argon Plasma

Pressure (mbar)	Glow Discharge Voltage (V)
0.089	468.0
0.095	458.7
0.13	378.3
0.17	317.8
0.22	293.4
0.27	288.9
0.31	274.9
0.36	286.5
0.41	302.0
0.44	309.3
0.53	321.5
0.60	362.8

Figure B.1 and Figure B.2 illustrate the Paschen curves derived from these measurements. These results provide insight into the breakdown characteristics of air and argon under low-pressure conditions. For improved accuracy—particularly near the curve's extrema—a high-voltage DC power supply would enable more precise control and detection of the true breakdown threshold.

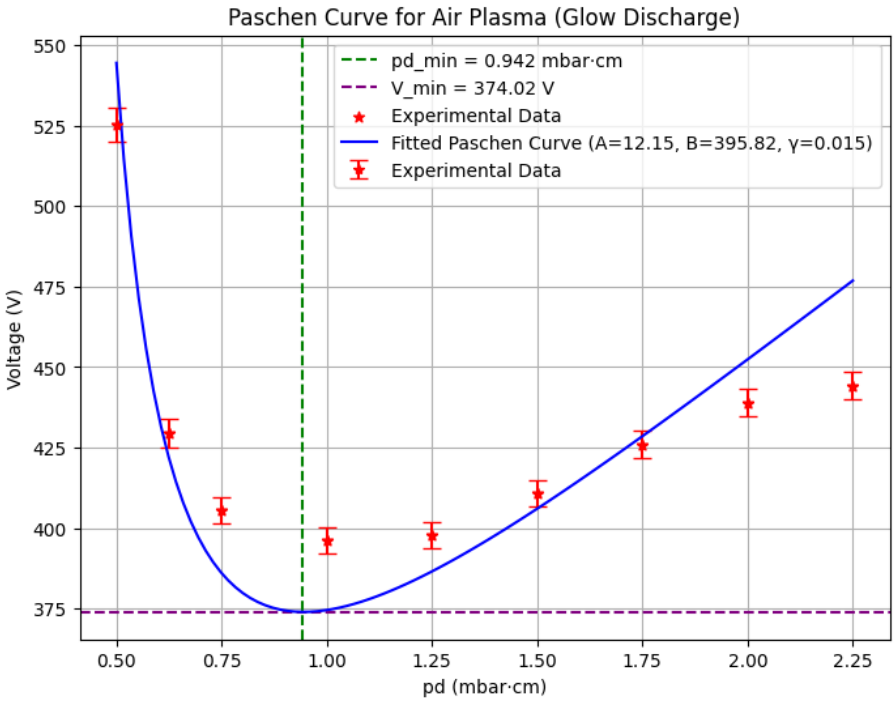

Figure B.1: Paschen Curve for Air Plasma.

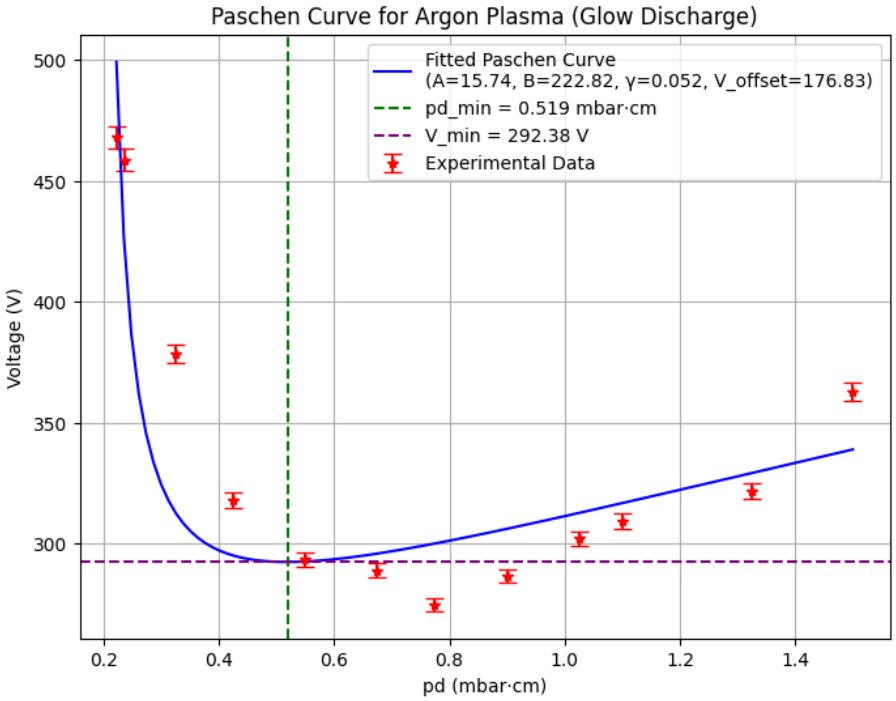

Figure B.2: Paschen Curve for Argon Plasma.

Bibliography

[1] Francis F. Chen, *Introduction to Plasma Physics and Controlled Fusion*, 3rd ed., Springer Cham,ISBN: 978-3-319-22309-4, 2015.

[2] J. A. Bittencourt, *Fundamentals of Plasma Physics*, Springer eBooks, 2004, https://doi.org/10.1007/978-1-4757-4030-1.

[3] Michael A. Lieberman and Allan J. Lichtenberg, *Principles of Plasma Discharges and Materials Processing*, 2nd ed., Wiley-Interscience, Hoboken, NJ, 2005.

[4] Alexander Fridman, *Plasma Chemistry*, Cambridge University Press, 2008. https://doi.org/10.1017/CBO9780511546075

[5] Science Photo Library. *Franklin's Lightning Experiment, 1752*. Retrieved April 12, 2025, from https://www.sciencephoto.com/media/654233/view/franklin-s-lightning-experiment-1752

[6] P. McQuillen, Q. Si, and O. K. Wiess, *High Resolution Sculpting and Imaging of Ultracold Neutral Plasmas*, Master's thesis, Rice University, 2012.

[7] PMF IAS, *The Sun's Internal Structure and Atmosphere, Solar Wind*, Published December 26, 2024. https://www.pmfias.com/sun-internal-structure-atmosphere/

[8] Wikipedia contributors, *Solar wind*, Wikipedia, The Free Encyclopedia, https://en.wikipedia.org/wiki/Solar_wind.

[9] Institute of Space and Astronautical Science (ISAS), JAXA, *As a storm develops in space, plasma originating from the Earth becomes the main component of the inner magnetosphere*, October 31, 2023. https://www.isas.jaxa.jp/en/topics/003566.html

[10] Stefanie Waldek and Daisy Dobrijevic, *Northern lights (aurora borealis)*, Space.com, November 21, 2024. https://www.space.com/15139-northern-lights-auroras-earth-facts-sdcmp.html

[11] Encyclopædia Britannica, *Electric Discharge Lamp*, Published March 2025. https://www.britannica.com/technology/electric-discharge-lamp

[12] RFHIC, *The Role of Plasma Technology and Deposition Techniques in Semiconductor Manufacturing*, Published October 2023. https://rfhic.com/industries-rf-energy/industrial/the-role-of-plasma-technology-and-deposition-techniques-in-semiconductor-manufactu

[13] G. Sonnino, et.al, *Turbulent Transport in Tokamak-plasmas: A Thermodynamic Approach*, arXiv preprint arXiv:2206.08310, June 2022. https://arxiv.org/abs/2206.08310

[14] J. T. Gudmundsson and A. Hecimovic, *Foundations of DC Plasma Sources*, Plasma Sources Science and Technology, vol. 26, no. 12, p. 123001, Nov. 2017. https://doi.org/10.1088/1361-6595/aa940d

[15] Impedans Ltd., *Capacitively Coupled Plasma*, Published August 2022. https://www.impedans.com/docs/capacitively-coupled-plasma/

[16] M. M. Plakhotnyuk *et al.*, *Low surface damage dry etched black silicon*, *Journal of Applied Physics*, vol. 122, no. 14, p. 143101, Oct. 2017. https://doi.org/10.1063/1.4993425

[17] Metal Power Instruments, "Understanding OES: What is Optical Emission Spectroscopy", https://www.metalpower.net/oes/understanding-oes/, Accessed: 2024-04-11.

[18] R. S. Mohammed, K. A. Aadim, and K. A. Ahmed, "Laser Intensity and Matrix Effect on Plasma Parameters for CuZn, Cu, and Zn Produced by Nd:YAG Laser," Acta Physica Polonica A, vol. 140, no. 3, pp. 306–309, 2021.

[19] H. H. Kadhim, R. S. Mohammed, and M. Al Marjine, "Optical Emission Spectroscopy Technique to Estimation of Electron Temperature and Density of Plasma Jet Induced by Applied AC High Voltage," 2022.

[20] D. R. S. Pambudi et al., "Optical Emission Spectroscopy Study of the Electron Temperature and Electron Density Dependence on the Pressure Chamber for the Carbon Deposition Produced by Argon Plasma Sputtering," IOP Conf. Ser.: Mater. Sci. Eng. 833 012083, 2020.

[21] NIST Atomic Spectra Database, https://physics.nist.gov/PhysRefData/ASD/

[22] N. Konjević *et al.*, Experimental Stark Widths and Shifts for Spectral Lines of Neutral and Ionized Atoms: A Critical Review of Selected Data for the Period 1989 Through 2000, *Journal of Physical and Chemical Reference Data*, **31**(3), 819–927 (2002). doi:10.1063/1.1486456

[23] Albert W. Hull and Irving Langmuir, "Control of an Arc Discharge by Means of a Grid," *Proc. Natl. Acad. Sci. USA*, vol. 15, no. 3, pp. 218-225, Mar. 1929.

[24] European Space Agency, "Rosetta - ESA's comet chaser", Retrieved from https://www.esa.int/Science_Exploration/Space_Science/Rosetta.

[25] F. F. Chen and J. P. Chang, "Langmuir Probes," in *Lecture Notes on Principles of Plasma Processing*, Springer US, Boston, MA, 2003, pp. 79–93.

[26] F.F. Chen and J.D. Evans, unpublished data.

[27] I. D. Sudit and R. C. Woods, "A workstation based Langmuir probe system for low-pressure dc plasmas," *Review of Scientific Instruments*, vol. 64, no. 9, pp. 2440–2448, Sep. 1993.

[28] F.F. Chen, J.D. Evans, and D. Arnush, Phys. Plasmas 9, 1449 (2002).

[29] W. J. Carey *et al.*, "Characterization of Paschen curve anomalies at high pd values," *IEEE Transactions on Dielectrics and Electrical Insulation*, vol. 17, no. 4, pp. 1182–1188, 2010.

[30] J. Loureiro *et al.*, "A Paschen curve experiment for e-lab," *Proceedings of the Remote Engineering and Virtual Instrumentation (REV)*, Lisbon, Portugal, 2010.

[31] S. A. Wissel *et al.*, "The use of dc glow discharges as undergraduate educational tools," *American Journal of Physics*, vol. 81, no. 9, pp. 663–669, 2013. doi:10.1119/1.4811435

[32] P. Mathew *et al.*, "Experimental verification of modified Paschen's law in DC glow discharge argon plasma," *AIP Advances*, vol. 9, no. 2, 025215, 2019. doi: 10.1063/1.5086246

[33] G. Galli *et al.*, "Paschen's law in extreme pressure and temperature conditions," *IEEE Transactions on Dielectrics and Electrical Insulation*, vol. 20, no. 3, pp. 865–873, 2013.

[34] C. Chen *et al.*, "Langmuir Probe Diagnostics with Optical Emission Spectrometry (OES) for Coaxial Line Microwave Plasma," *Applied Sciences*, vol. 10, no. 22, p. 8165, 2020. doi:10.3390/app10228165

[35] J. C. Palomares *et al.*, "Experimental study of the modified Paschen's law: glow discharge of Ethanol (CH_3CH_2OH), Methanol (CH_3OH) and its mixture," *Revista Mexicana de Física*, 68(3), 030101, 2022.

[36] B. Zh. Chektybayev *et al.*, "Measurement of plasma parameters in the PBI using the Langmuir probe," *Nuclear Instruments and Methods in Physics Research Section A*, vol. 1028, pp. 166297, 2022. doi:10.1016/j.nima.2021.166297

[37] N. Savard *et al.*, "Comparison of Langmuir probe and optical emission spectroscopy on a volume-cusp filament ion source using helium," *Review of Scientific Instruments*, vol. 93, no. 10, 103303, 2022. doi:10.1063/5.0092156

[38] J. Cooper, Plasma spectroscopy, *Reports on Progress in Physics*, **29**(1), 35–106 (1966). `http://iopscience.iop.org/0034-4885/29/1/302`

[39] J. Blue *et al.*, Creating, implementing, and sustaining an advanced optical spectroscopy laboratory course, *American Journal of Physics*, **78**(5), 549–556 (2010). doi: 10.1119/1.3327859

[40] R. S. Mohammed *et al.*, "Laser Intensity and Matrix Effect on Plasma Parameters for CuZn, Cu, and Zn Produced by Nd:YAG Laser," *Acta Physica Polonica A*, vol. 140, pp. 306–310, 2021. doi:10.12693/APhysPolA.140.306

[41] Mazen, A.*et al.*, (2023). Analysis of the argon plasma spectrum and calculation of the plasma temperature according to the local thermodynamic equilibrium (LTE). *Journal of Physics*, University of Mosul.

[42] I. D. Sudit and F. F. Chen, "RF compensated probes for high-density discharges," *Plasma Sources Science and Technology*, vol. 3, no. 2, pp. 162, 1994.

[43] L. Conde, "An introduction to Langmuir probe diagnostics of plasmas," 2011. Available at: `https://api.semanticscholar.org/CorpusID:53622081`.

[44] Z. Bigelow and L. F. Velásquez-García, "Fully 3D-Printed Miniature Langmuire Multi-Probe Sensor for Cubesat Ionospheric Plasma Diagnostics," *2023 IEEE 36th International Vacuum Nanoelectronics Conference (IVNC)*, Cambridge, MA, USA, 2023, pp. 103-105

[45] T. A. Bekkeng, E. S. Helgeby, A. Pedersen, E. Trondsen, T. Lindem, and J. I. Moen, "Multi-Needle Langmuir Probe System for Electron Density Measurements and Active Spacecraft Potential Control on CubeSats," *IEEE Transactions on Aerospace and Electronic Systems*, vol. 55, no. 6, pp. 2951-2964, Dec. 2019.

[46] ESA, "Multi-Needle Langmuir Probe Tested and Ready for Launch," European Space Agency, [Online]. Available: `https://www.esa.int/Enabling_Support/Space_Engineering_Technology/Shaping_the_Future/Multi-Needle_Langmuir_Probe_Tested_and_Ready_for_Launch`. [Accessed: 16-Nov-2024].

[47] V. K. Yadav and D. Bora, ”Electric probes for characterization of microwave-produced plasma,” *Physica Scripta*, vol. 2008, no. T131, p. 014023, 2008.

[48] OriginLab Corporation, *OriginLab Software*, Available at: `https://www.originlab.com`, Accessed: 2024-04-23.

[49] Analog Devices Inc. *LTspice Simulator Resources*. `https://www.analog.com/en/resources/design-tools-and-calculators/ltspice-simulator/ltspice-recommended-reading-list.html`